A&A 478, 615–658 (2008)
DOI: 10.1051/0004-6361:20077930

Astronomy & Astrophysics

A catalog of galaxy clusters observed by XMM-Newton⋆

S. L. Snowden[1], R. F. Mushotzky[2], K. D. Kuntz[3], and D. S. Davis[4,5]

[1] Code 662, NASA/Goddard Space Flight Center, Greenbelt, MD 20771, USA
e-mail: steven.l.snowden@nasa.gov
[2] Code 662, NASA/Goddard Space Flight Center, Greenbelt, MD 20771, USA
e-mail: richard.f.mushotzky@nasa.gov
[3] Henry A. Rowland Department of Physics and Astronomy, The Johns Hopkins University, 3400 N. Charles Street, Baltimore, MD 21218, USA
e-mail: kuntz@pha.jhu.edu
[4] Department of Physics, University of Maryland, Baltimore County, 1000 Hilltop Circle, Baltimore, MD 21250, USA
[5] CRESST and the Astroparticle Physics Laboratory, NASA/GSFC, Greenbelt, MD 20771, USA
e-mail: david.s.davis@nasa.gov

Received 22 May 2007 / Accepted 3 October 2007

ABSTRACT

Aims. We present a uniform catalog of the images and radial profiles of the temperature, abundance, and brightness for 70 clusters of galaxies observed by *XMM-Newton*.
Methods. We use a new "first principles" approach to the modeling and removal of the background components; the quiescent particle background, the cosmic diffuse emission, the soft proton contamination, and the solar wind charge exchange emission. Each of the background components demonstrate significant spectral variability, several have spatial distributions that are not described by the photon vignetting function, and all except for the cosmic diffuse emission are temporally variable. Because these backgrounds strongly affect the analysis of low surface brightness objects, we provide a detailed description our methods of identification, characterization, and removal.
Results. We have applied these methods to a large collection of XMM-Newton observations of clusters of galaxies and present the resulting catalog. We find significant systematic differences between the *Chandra* and *XMM-Newton* temperatures.

Key words. X-rays: galaxies: clusters – methods: data analysis

1. Introduction

Clusters of galaxies are the largest and most massive collapsed objects in the universe, and as such they are sensitive probes of the history of structure formation. While first discovered in the optical band in the 1930s (for a review see Bahcall 1997), in some ways the name is a misrepresentation since most of the baryons and metals are in the diffuse hot X-ray emitting intercluster medium and not in the galaxies. Clusters are fundamentally "X-ray objects" as it is this energy range where this preponderance of the baryons is visible. Studies of cluster evolution can place strong constraints on all theories of large scale structure and determine precise values for many of the cosmological parameters. As opposed to galaxies, clusters probably retain all the enriched material created in them, and being essentially closed boxes they provide a record of nucleosynthesis in the universe. Thus measurement of the elemental abundances and their evolution with redshift provides fundamental data for the origin of the elements. The distribution of the elements in clusters reveals how the metals moved from stellar systems into the IGM. Clusters should be fair samples of the universe and studies of their mass and their baryon fraction should reveal the gross properties of the universe as a whole. Since most of the baryons are in the gaseous phase and clusters are dark-matter dominated, the detailed physics of cooling and star formation are much less important than in galaxies. For this reason, clusters are much more amenable to detailed simulation than galaxies or other systems in which star formation has been a dominant process.

Clusters are luminous, extended X-ray sources and are visible out to high redshifts with current technology. The virial temperature of most groups and clusters corresponds to $T \sim 2{-}100 \times 10^6$ K ($kT \sim 0.2{-}10$ keV, velocity dispersions of 180−1200 km s^{-1}), and while lower mass systems certainly exist we usually call them galaxies. Most of the baryons in groups and clusters of galaxies lie in the hot X-ray emitting gas that is in rough virial equilibrium with the dark matter potential well (the ratio of gas to stellar mass is ∼2−10:1, Allen et al. 2001). This gas is enriched in heavy elements (Mushotzky et al. 1978) and it thus preserves a record of the entire history of stellar evolution in these systems. The presence of heavy elements is revealed by line emission from H and He-like transitions as well as L-shell transitions of the abundant elements. Most clusters are too hot to have significant (>2 eV equivalent width) line emission from C or N, although cooler groups may have detectable emission from these elements. However, all abundant elements with $z > 8$ (oxygen) have strong lines from H and He-like states in the X-ray band and their abundances can be well determined.

Clusters of galaxies were discovered as X-ray sources in the late 1960's (for a historical review see Mushotzky 2002) and large samples were first obtained with the *Uhuru* satellite in the

⋆ Based on observations obtained with *XMM-Newton*, an ESA science mission with instruments and contributions directly funded by ESA Member States and NASA.

early 1970's (Jones & Forman 1978). Large samples of X-ray spectra and images were first obtained in the late 1970's with the *HEAO* satellites (for an early review see Jones & Forman 1984). The early 1990's brought large samples of high quality images with the *ROSAT* satellite and good quality spectra with *ASCA* and *Beppo-SAX*. In the last few years there has been an enormous increase in the capabilities of X-ray instrumentation due to the launch and operation of *Chandra* and *XMM-Newton*. Both *Chandra* and *XMM-Newton* can find and identify clusters out to $z > 1.2$ and their morphologies can be clearly discerned to $z > 0.8$. Their temperatures can be measured to $z \sim 1.2$ and *XMM-Newton* can determine their overall chemical abundances to $z \sim 1$ with a sufficiently long exposure. For example, a cluster at $z = 1.15$ has recently had its temperature and abundance well constrained by a 1 Ms *XMM-Newton* exposure (Hashimoto et al. 2004).

The temperature and abundance profiles of clusters out to redshifts of $z \sim 0.8$ can be measured and large samples of X-ray selected clusters can be derived. *Chandra* can observe correlated radio/X-ray structure out to $z > 0.1$ and has discovered internal structure in clusters. The *XMM-Newton* grating spectra can determine accurate abundances for the central regions of clusters in a model independent fashion for oxygen, neon, magnesium, iron, and silicon. Despite the stunning successes of the *Chandra/XMM-Newton* era, clusters have not yet fulfilled their promise as a cosmological Rosetta stone; the most important tests of cluster theory require measurements of cluster properties to large radii ($R \sim R_{\rm virial}$) which is observationally difficult. The lack of consensus among the recent X-ray missions about, for example, temperature profiles, is a large stumbling block in the use of clusters for cosmological purposes.

1.1. Temperature structure of clusters

As discussed in detail by Evrard (2003), we now have a detailed understanding of the formation of the dark matter structure for clusters of galaxies. If gravity has been the only important physical effect since the formation, then the gas should be in rough hydrostatic equilibrium and its density and temperature structure should provide a detailed measurement of the dark matter distribution in the cluster. Recent theoretical work has also taken into account other processes, such as cooling, which can be important. The fundamental form of the Navarro et al. (1997) dark matter potential and the assumption that the fraction of the total mass that is in gas is constant with radius results in a prediction that the cluster gas should have a declining temperature profile at a sufficiently large distance from the center (in $R/R_{\rm viral}$ units), both from analytic (Komatsu & Seljak 2001) and numerical modeling (Loken et al. 2002). The size of the temperature drop in the outer regions is predicted to be roughly a factor of 2 by $R/R_{\rm viral} \sim 0.5$.

Although some observational results appear consistent with the theoretical predictions (in particular, the *ASCA* results of Markevitch et al. 1998), many others do not, and considerable controversy exists. Much of the uncertainty of the pre-*Chandra*/pre-*XMM-Newton* data arises from insufficient spectral and spatial resolution and the resultant difficulties in removing backgrounds, modeling the spectra, and interpreting the results. For example, the *ASCA* results of Markevitch et al. (1998) were consistent with a decline in temperature with radius, while the analysis of a similar sample of clusters by Kikuchi et al. (1999), White & Buote (2000), and White (2000) revealed a large number of isothermal clusters. Similar results were obtained from *Beppo-SAX*, with de Grandi et al. (1999) finding temperature gradients and Irwin & Bregman (2000) finding isothermality. Simultaneous analysis of the higher angular resolution *ROSAT* data with the *ASCA* data did not resolve the issue; Finoguenov et al. (2001) finding gradients and Irwin et al. (1999) isothermal profiles. The bulk of the problem with interpreting *ASCA* results is the analysis of impact of the PSF on the profile (Irwin et al. 1999).

XMM-Newton and *Chandra* have significantly better spectral and angular resolution than the previous generation of missions and might be expected to resolve the previous controversies. The recent *Chandra* results of Vikhlinin et al. (2006) show a temperature profile in good agreement with the gradients seen by Markevitch et al. (1998) results and predicted by the standard theory. Analysis of samples of cooling flow clusters with *XMM-Newton* (Piffaretti et al. 2005; Arnaud et al. 2005; Pratt et al. 2007) are also mostly consistent with the Markevitch et al. (1998) results. However flatter, more isothermal profiles have also been found in both *Chandra* and *XMM-Newton* observations (Allen et al. 2001; Kaastra et al. 2004; Arnaud et al. 2005). Despite some early difficulties (e.g., Donahue et al. 2006), the *Chandra* and *XMM-Newton* calibrations have stabilized but agreement between the two great observatories is not assured (e.g, Vikhlinin et al. 2006). The difference in the PSF between the two instruments as well as different methods of background subtraction often make direct comparison difficult. Further, an agreement between *Chandra* and *XMM-Newton* would not entirely resolve the problem; the smaller FOV of current instruments have led to observation of a somewhat higher redshift sample than observed by the previous generation of instruments, suggesting that part of the difference between the *XMM-Newton*/*Chandra* results and the *ASCA*/*ROSAT*/*Beppo-SAX* results may be due to a real difference between clusters at lower and higher redshifts.

The measurement of the cluster mass function can provide a sensitive cosmological test but is sensitive, in turn, to the parameters that are directly measurable, and especially to the observed quantities at large radius. Recent simulations show that cluster temperature profiles decline with radius but less rapidly than is shown by previous X-ray analysis (e.g., Kay et al. 2004). Since the total mass of the cluster is quite sensitive to the measured temperature profile (Rasia et al. 2006), particularly at large radii, these systematic differences lead to significant uncertainties in the cosmological constraints. Thus, there is an urgent need to understand the temperature profiles of clusters at large radii and to understand the source of the systematic differences observed in the literature.

In this paper we consider a large sample of clusters observed with the *XMM-Newton* observatory and derive temperature, density and abundance profiles for many of these systems out to near the virial radius. We present a new technique that should provide more accurate background subtraction at large radii, and are careful to correct for the effect of the finite *XMM-Newton* PSF. A comparison of our measurements with *Chandra* measurements of the same clusters shows a simple systematic difference between the two observatories. Although we have not yet determined the source of that difference, resolution of this relatively well defined issue should significantly reduce the uncertainties in cluster cosmology.

1.2. Analysis of extended sources

The analysis of extended sources in X-ray astronomy is typically problematic and quite often very complex. This is particularly true for objects which subtend the entire field of view (FOV)

of the observing instrument such as nearby galaxies, relatively nearby clusters of galaxies, many regions of galactic emission, and of course the cosmic diffuse background. Even with objects smaller than the FOV, quite often the simple subtraction of a nearby "background" region from the same data set is inappropriate due to spectral and spatial variations in the internal background and angular variations in the cosmic background. The use of deep "blank sky" observations can also be inappropriate due to the same considerations, as well as the probability that many background components are temporally varying. Because of the temporal variation of the background and the angular variation of the cosmic background, the average of the blank-sky data, even after normalization, may not match the conditions of a specific observation of interest, and so may yield an incorrect result.

While the cores of many clusters are relatively bright in X-rays so the treatment of the background is not such a significant consideration, at the edges of clusters it is absolutely critical. Clusters fade gently into the backgrounds at large radii, therefore improving the modeling of the backgrounds extends the reliable radial range for the determination of cluster parameters.

Critical to compensating for the various background components by filtering, subtraction, or modeling is a basic understanding of their origin and effects on the detectors. Unfortunately this usually takes a considerable amount of time to develop, which is why useful methods for a specific observatory become available to the general community only years into the mission. Even then, the methods will continue to evolve with greater understanding of the various background components and their temporal evolution, and the operation of the instruments. In addition, the efforts are quite often undertaken by individuals who are not project personnel, but whose scientific interests require the improved analysis methods.

This is certainly true of the *XMM-Newton* mission and observations using the EPIC instruments. Several groups have presented methods and published scientific results based upon them (Arnaud et al. 2001; Read & Ponman 2003; Nevalainen et al. 2005; de Luca & Molendi 2004). As opposed to these methods which derive background spectra from normalized blank-sky observations, this paper presents the details of a method based as much as possible on the specific understanding of the individual background components. This method was used successfully in the paper identifying the solar wind charge exchange emission in the *XMM-Newton* observation of the Hubble Deep Field North (Snowden et al. 2004).

Section 2 of this paper gives a short description of the *XMM-Newton* observatory, Sect. 3 discusses the various background components and the suggested methods used to compensate for them, Sect. 4 demonstrates the data reduction method using the observation of Abell 1795. Section 5 applies the methods to the determination of the temperature, abundance, and flux radial profiles of a catalog of 70 clusters of galaxies and presents the results, and Sect. 6 discusses the conclusions. Note that the detailed discussion of the science derived from these observations is deferred to Paper II.

Currently the specific method and software package discussed here are only applicable to EPIC MOS data. Although the MOS and pn experience the same backgrounds, the physical difference between the two detectors (readout rates, fraction of unexposed pixels, etc.) make analysis of the pn background somewhat more difficult than that of the MOS. However, the analysis methods described here are being extended to the pn.

2. *XMM-Newton* and the EPIC MOS Detectors

The *XMM-Newton* observatory (Ehle et al. 2005) orbits the Earth in a long period (~48 h), highly elliptical path (the original perigee and apogee were ~6000 km and ~115 000 km but they have since evolved over the mission to ~19 000 km and ~103 000 km as of 2006 June). The scientific package of *XMM-Newton* is comprised of six independent but co-aligned instruments which operate simultaneously. The European Photon Imaging Camera (EPIC) is comprised of three CCD imagers of two distinct technologies (MOS and pn), and are coupled to the three X-ray mirror assemblies. The EPIC instruments provide imaging over a ~30′ FOV with moderate energy resolution. Half of the light from two of the X-ray mirrors (those with the MOS detectors) is diverted by reflection gratings to the Reflection Grating Spectrometer (RGS), two instruments which provide high spectral resolution for point sources and small-scale extended objects (<2′). The final scientific instrument is the Optical Monitor (OM) which is an optical/UV telescope with a FOV (17′ × 17′) somewhat smaller than that of the EPIC.

The EPIC MOS detectors are each comprised of seven individual CCDs where one is roughly centered on the optical axis and the others form a hexagonal pattern surrounding it. The central CCD can be operated independently in several different observation modes (imaging, windowed imaging, and timing) while the outer CCDs always operate in the standard imaging mode. There are three optical blocking filters (thin, medium, and thick) which can be set by the observer. The filter wheel has a circular aperture with a 30′ diameter which leaves portions of the outer CCDs shielded from exposure to the sky. These unexposed corners of the detectors play a vital role in the modeling of the quiescent particle background (QPB) as described below. The filter wheel also has settings which expose the CCDs to an on-board calibration source (cal-closed position) and which block the sky (filter wheel closed position, FWC), data from the latter position are also used in modeling the QPB. 13 of the 14 MOS CCDs are still functioning as of 2007 September, one of the MOS1 outer CCDs (CCD #6) was lost to a micrometeorite hit on 2005 March 9.

3. EPIC MOS background components

There are five major contributors to the background of EPIC MOS (and pn) observations that we consider here. However, the characterization of some components as background is occasionally debatable as they may actually be the main scientific interest of an observation. The first is the quiescent particle background, a continuum component produced by the interaction of high energy penetrating particles with the detectors. Generally included with, but distinct from, the QPB are fluorescent X-rays (FX) which are produced by the particle flux interacting with various components of the satellite and then are detected by the instruments. For the MOS the fluorescent X-rays are dominated by the lines Al Kα ($E \sim 1.49$ keV) and Si Kα ($E \sim 1.75$ keV), but there are also lines from other elements at higher energies (Au, Cr, Mn, Fe, Ni, Zn). The continuum QPB dominates at high (above ~2 keV) and low (below ~1.2 keV) energies while the Al and Si lines dominate the 1.3−1.9 keV band.

The third background component is also produced locally at the detectors and is caused by soft protons (SP, with energies less than a few 100 keV[1]) which travel down the telescope light path

[1] *XMM-Newton* Technical Note XMM-SOC-USR-TN-0014, P. M. Rodriguez-Pascual & R. González-Riestra,

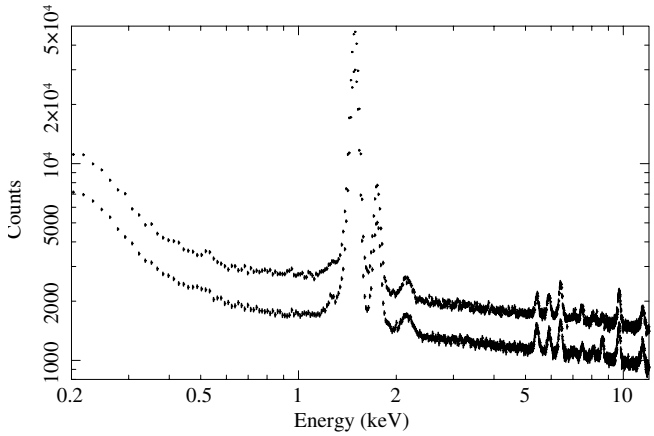

Fig. 1. Filter wheel closed spectra for the MOS1 (*upper*) and MOS2 (*lower*) detectors. The MOS2 data have been scaled by a factor of 1.5 in order to separate the spectra for clarity. The spectra are comprised of a general continuum from the QPB and the FX lines of Al, Si, Au, and other elements. The energy binning for the data is a constant 15 eV.

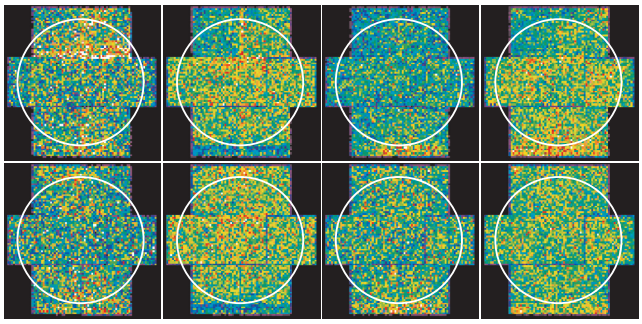

Fig. 2. Images in detector coordinates of the FWC data for the MOS1 (*upper row*) and MOS2 (*lower row*) detectors. The data are from (*left to right*) the 0.35−1.25, 1.25−2.0, 2.0−4.0, and 4.0−8.0 keV bands, and have been binned into 25″ × 25″ pixels. The 1.25−2.0 band is most affected by the FX contamination, and it is likely that there is some difference between the spatial distributions between FWC and open data due to the different source geometry. Note that all of the bands show at least somewhat different structure. The circles indicate the FOV regions of the instruments outside of which the detectors are always shielded from cosmic X-rays.

and deposit their energy directly in the detectors. The SP spectrum, as recorded by the EPIC detectors, can be described by a power-law continuum and varies both in magnitude and slope. The soft proton background is highly variable and enhancements in the soft proton background are often referred to as "flares".

For many observations the fourth component, the cosmic X-ray background (CXB), is a source of contamination although it can also be the scientific goal of the observation. The diffuse CXB dominates below ∼1 keV and has a thermal spectrum dominated by emission lines. It is the superposition of Galactic emission from multiple sources as well as the Galactic halo and perhaps even more distant emission, and is strongly variable over the sky. Included in the CXB is the unresolved emission from the superposition of cosmological objects (e.g., AGN, Hickox & Markevitch 2007) which dominates at higher energies and Galactic stars with a relatively minor contribution at lower energies (e.g., Kuntz & Snowden 2001). The average spectrum of the cosmological emission is for the most part a power law continuum with a possible change in slope at lower energies. There is thought to be a true cosmic variation of magnitude on the sky but there is also the obvious variation caused by the excision of point sources to various levels.

The fifth background component, solar wind charge exchange emission (SWCX, e.g., Wargelin et al. 2004; Snowden et al. 2004), like the CXB, can either be background or a source of scientific interest, although admittedly to a rather limited community. SWCX in the MOS energy band is essentially all line emission at energies less than ∼1.3 keV and is strongly variable in both total magnitude and relative line strengths. For the MOS detectors of *XMM-Newton* the strongest SWCX emission is from C VI, O VII, O VIII, Ne IX, and Mg XI, although this ignores the $\frac{1}{4}$ keV band where *ROSAT* observations were occasionally affected by very strong SWCX emission.

3.1. Quiescent particle background

The QPB and FX for the EPIC MOS detectors has been well studied by Kuntz & Snowden (2008, hereafter KS07) and is the dominant background above ∼2.0 keV. In general it is relatively featureless and resembles a power law which is not folded through the instrumental effective area. Figure 1 shows MOS1 and MOS2 spectra compiled from observations where the filter wheels were in their closed positions (FWC) while Fig. 2 shows FWC images in several bands. In this configuration no particles or X-rays passing through the optical system can penetrate to the detectors, nor are the on-board calibration sources visible to the detectors. The FOV of the detectors for cosmic X-rays and soft protons is constrained by a circular aperture indicated by the circles in the figure. The permanently shielded regions of the CCDs, i.e., the corner regions outside of the circles in Fig. 2, are read out the same as those within the FOV and experience roughly the same QPB flux.

The QPB spectra for the two detectors (Fig. 1) are very similar and show a strong continuum with the Al Kα and Si Kα lines, as well as a few lines from other elements. Figure 2 shows that the distribution of counts over the detectors is clearly not uniform, and that the contributions from the Al Kα and Si Kα fluorescent lines are distributed somewhat differently from the QPB as well.

In addition to the spatial variation of the QPB over the detectors, there is also a temporal variation in the spectra both in magnitude and in hardness. Figure 3 (top panel) shows the QPB count rates from the CCD corners outside of the FOV in the 0.3−10.0 keV band. The temporal variation is due both to changes in the CCDs and their operating conditions as well as variations of the particle flux over the course of the solar cycle. Some of the short-term scatter is due to the varying conditions during the orbit (∼2 days). Observations can take place both inside and outside of the magnetosheath and at various distances from the particle belts. Figure 3 (bottom panel) shows the QPB hardness ratio (the ratio of the 2.5−5.0 keV band to the 0.4−0.8 keV band) over the course of the mission for the individual CCDs. Of note are the occasional deviations of CCD #5 of both instruments as well as MOS1 CCD #4 from relatively nominal levels and the loss of MOS1 CCD #6 near revolution (orbit) 950. The deviations are due to a strong enhancement in the background below $E \sim 1$ keV and are extensively discussed in KS07.

http://xmm.esac.esa.int/ docs/documents/ USR-TN-0014-1-0.pdf.

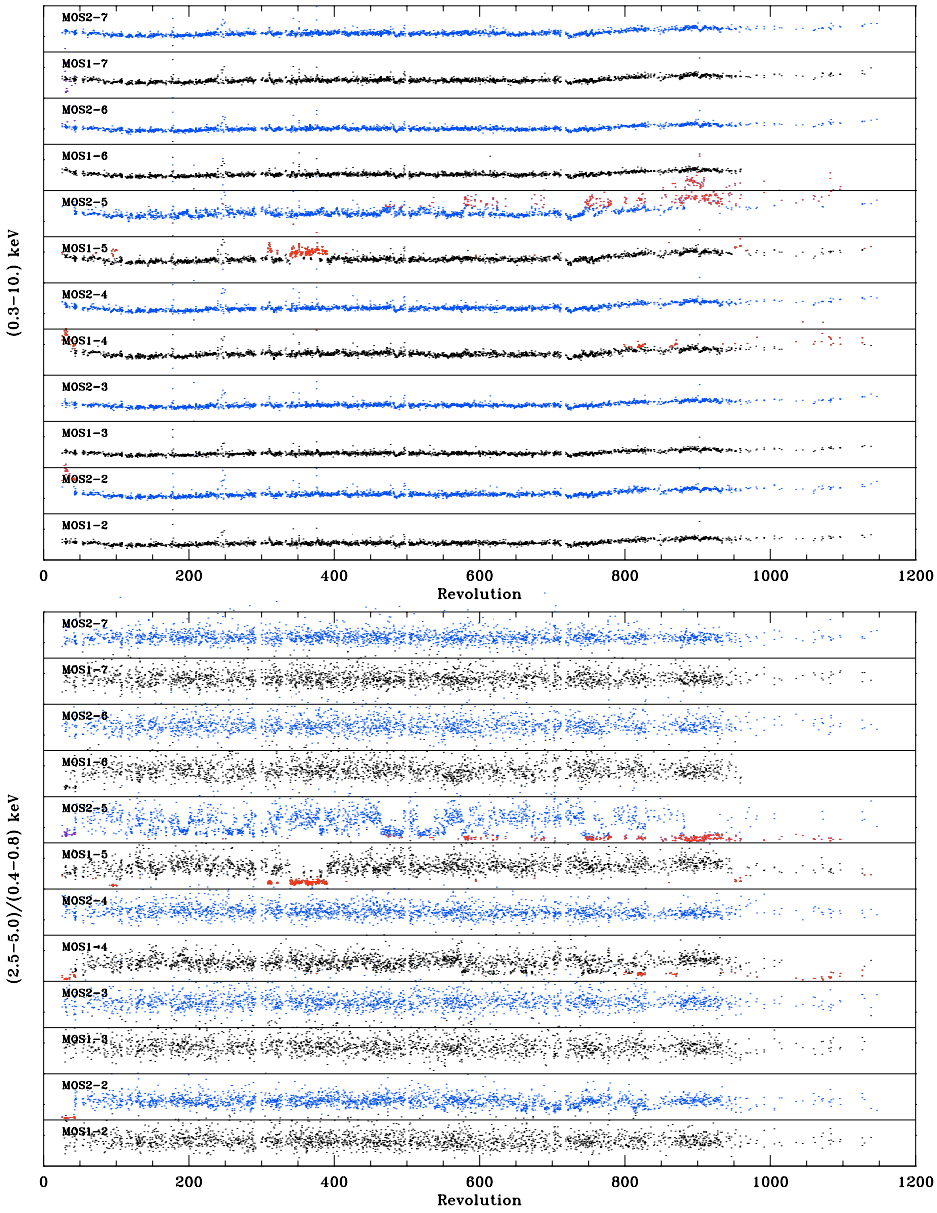

Fig. 3. *Top panel*: QPB count rate in the 0.3−10.0 keV band from the out-of-FOV corners of the detectors from KS07 (their Fig. 6) for the individual CCDs from both MOS instruments. The MOS1 data are shown in black, the MOS2 data are shown in blue, and time periods of anomalous CCD background behavior are shown in red. *Bottom panel*: QPB (2.5−5.0 keV)/(0.4 − 0.8 keV) hardness from the out-of-FOV corners of the detectors from KS07 (their Fig. 7) for the individual CCDs from both MOS instruments. The MOS1 data are shown in black, the MOS2 data are shown in blue, and time periods of anomalous CCD background behavior are shown in red. The plot limits are 0−0.075 counts s^{-1} $chip^{-1}$ for the count-rate plots and 0−7.5 for the ratio plots. The data are linearly scaled in both cases.

3.1.1. Treatment of the QPB

In all of the discussion above only the quiescent part of the particle background is considered, these are the time periods not affected by flares. Frequently times of particle background flaring are so intense that the instruments must be turned off for their health. Periods of less intense flaring are easily filtered out by light-curve screening, which is discussed in Sect. 3.2.1.

The QPB for an individual observation (primary observation, PO) can be modeled and subtracted with, in general, quite high reliability using the FWC data in conjunction with data from the unexposed corners of the CCDs (KS07). The modeling is a multi-step process, and is done for each detector and CCD individually. The process creates a background spectrum tailored for the specific region of interest where the spectrum of an astrophysical object is extracted. To summarize the process outlined in KS07: 1) after the PO has been screened for flares, the spectra from the unexposed corners of the outer CCDs are extracted. 2) The magnitudes (0.3−10.0 keV band) and hardness ratios (2.0−5.0 keV band to the 0.5−1.2 keV band) for the spectra are determined. 3) A data base of all archived observations is searched for observations (secondary observations, SO) whose unexposed corner spectra have similar magnitudes and hardness. 4) The PO corner spectra are then augmented by the SO corner spectra increasing the statistical significance of individual spectral bins to a useful level. This step makes the assumption that data collected from time periods of similar spectral magnitude and hardness have in aggregate the same spectrum. This appears to generally be the case, although CCDs #4 and #5 in their anomalous states can be problematic. 5) Spectra from the

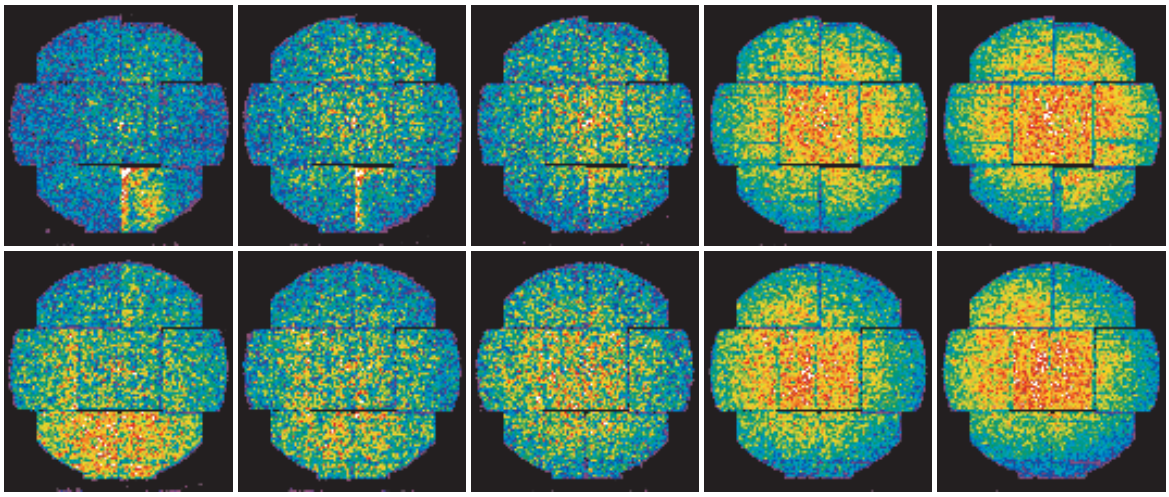

Fig. 4. Image in detector coordinates of the SP data for the MOS1 (*upper row*) and MOS2 (*lower row*) detectors. From left to right the data are from the 0.35−0.8 keV, 0.8−1.25 keV, 1.25−2.0 keV, 2.0−4.0 keV, and 4.0−8.0 keV bands. In the plots blue and green indicate lower intensities while red and white indicate higher intensities. The data are linearly scaled. For better statistics, data are from the observations using all filters have been combined as there is little difference between the distributions for the thin, medium, and thick filter observations separately. Note that the distributions are not flat across the detectors nor are they symmetrically vignetted like cosmic X-rays. As well, the distributions are not the same for different energies.

FWC data are extracted from CCD corners as well as from the region of interest. If the region of interest is comprised of more than one CCD, the individual CCD spectra are kept separate. 6) For the outside CCDs the FWC spectra from the region of interest are scaled, spectral bin by spectral bin, by the ratio of the augmented observation spectra from the CCD corners to the FWC spectra from the corners. The central CCD has to be handled in a more complicated way (KS07). 7) For reasons discussed in Sect. 3.1.2 below, the spectral region affected by the Al Kα and Si Kα lines (1.2−2.0 keV) is cut out and replaced by an interpolated power law. The EXPOSURE and BACKSCAL keywords in the background spectrum are set to be consistent with the PO. The spectrum is then included as the background in spectral fitting.

3.1.2. Treatment of the FX background

There are two reasons why the Al-Kα and Si-Kα FX background can not be treated in the same manner as the QPB. First, the environment with the filter wheel open (with the thin, medium, and thick filters) is different from that with the filter wheel closed, and therefore the distribution and magnitude of the FX background are unlikely to be the same. Second, there are quite large numbers of counts in the lines providing high statistics. Because of this, even the slight residual variations in the instrumental gains (within the gain uncertainty) when compared to the FWC data can produce large residuals. The most straightforward method for treating the lines is to fit them as separate Gaussian model components where the line energy is allowed to vary to achieve an acceptable fit.

3.2. Soft Proton background

The SP background is produced by relatively low energy protons (< a few 100 keV) passing down the telescope tube, penetrating the filters, and depositing their energy directly in the CCDs. This is a very problematic component which can vary from undetectable levels (by examination of the count rate) to strong flaring of over one hundred counts per second rendering the observation useless for the study of all but the brightest point sources. The SP spectrum is a continuum with variable hardness. The distribution of SP events across the FOV is different from both cosmic X-rays and the QPB, and varies as well with energy. Figure 4 shows SP background images collected from time intervals of slightly enhanced background (~1 counts s^{-1}) for several energy bands. While there is a significant variation in the distributions from low to high energies, and between the two detectors, they are relatively similar at energies >2.0 keV for the individual detectors where the SP contribution is relatively stronger.

3.2.1. Treatment of the SP Background

The primary treatment of the SP background is to filter the data by creating a light curve and excluding all time intervals with a count rate greater than some selected threshold. There are a number of different filtering methods in the literature but they all give basically the same results. Since most, if not all observations contain residual SP contamination at some level, the setting of the threshold becomes dependent on a trade-off between the level of that contamination and the amount of the exposure left over after the screening process. Our goal is to retrieve as much useful data as possible so rather than setting a strict limit to exclude all possible time periods of SP contamination (e.g., de Luca & Molendi 2004), we follow the working assumption that there will always be residual contamination which will be modeled during the spectral fitting process.

The filtering light curve is usually extracted in a high-energy band (e.g., 2.5−12.0 keV) and may or may not have had point sources excluded. Only infrequently is there a source in the field which is bright, sufficiently hard, and variable enough to significantly affect the filtering process. The light curve can be filtered either by setting a fixed absolute threshold or more creatively by using the light curve of the specific observation to set the threshold. We use this method in our analysis of the clusters presented here (see Sect. 4). In this method a histogram is made of the light curve count rate which typically has a roughly Gaussian peak with a high count-rate tail. A Gaussian is then fit to the peak of

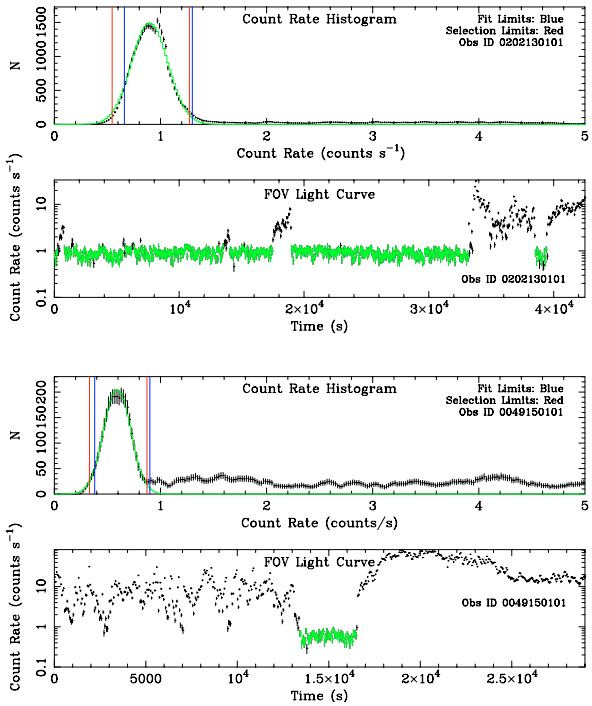

Fig. 5. Sample light curves and light-curve histograms from two observations with different amounts of SP contamination. The top two panels show the light-curve histogram and light curve for the data from ObsID 0202130101 while the bottom two panels show the same for ObsID 0049150101.

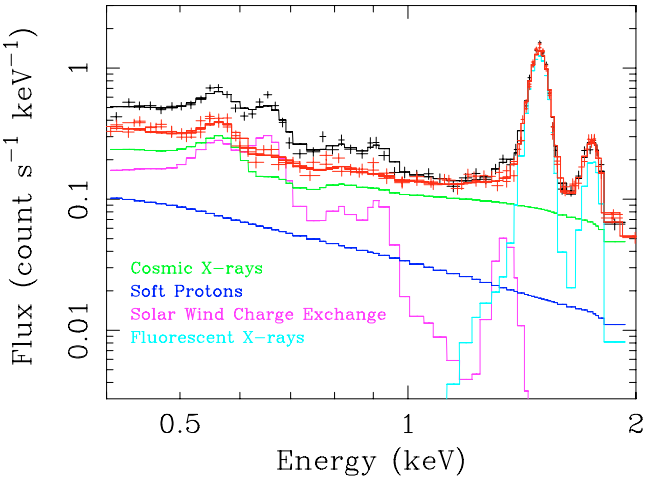

Fig. 6. Spectra from two of the four *XMM-Newton* EPIC MOS observations of the Hubble Deep Field North (ObsID 0202130101 in black and ObsID 0049150101 in red). The black data points and curve show the spectrum from the contaminated observation while the red data points and curve show an uncontaminated spectrum. The uncontaminated spectrum agreed well with the two other observations of this direction. The additional curves show the fitted model contributions to the fits where all components besides the SWCX emission were fit simultaneously for the two spectra.

the distribution and the threshold set at the mean value of the Gaussian plus some number of sigma (typically about 1.5σ). A second threshold is set at the mean value minus the same number of sigma to avoid biasing the data to lower count rates. The fitted width of the Gaussian can give an indication of residual low level contamination, although examination of the light curve can often do the same. The benefit of this more complicated screening method is that it works well for observations of bright, hard extended objects (e.g., clusters of galaxies).

As noted above, even after screening there may well be residual SP contamination in the data. This can be accommodated in the spectral fitting process by the inclusion in the model of a power law component which is not folded through the instrument effective area. Care needs to be taken, however, as power from the source signal can be transferred to the SP component.

Also note, again, that the screening process is inherently a trade-off between the amount of data available for analysis and how clean those data are. Figure 5 shows examples of two observation light curves along with their light-curve histograms. As can be seen, the extent of the contamination in a given observation is extremely variable, as well as the magnitude of that contamination. Also be aware that even though a light curve may look relatively flat, there is no guarantee that there is no contamination. Although the longer that the observation count rate looks constant, the more likely it is that the level of contamination is minimal. However, the data in Fig. 5 present a clear example of why caution is necessary in considering the possibility of residual SP contamination. The two observations are of the same direction on the sky (a density enhancement in the Magellanic Bridge with no bright point sources or extended emission) and the greater "nominal" count rate in the upper panel (ObsID 0202130101) is due entirely to a strong residual SP flux. In this case a relatively flat light curve is extremely misleading.

3.3. Solar wind charge exchange background

This is an insidious contributer to the backgrounds of extended objects, and particularly of observations of the diffuse background. SWCX emission is produced as the solar wind flows out from the Sun and interacts with material in the solar system. This includes both interstellar neutral material from the Local Cloud (Lallement 2004) flowing through the solar system and exospheric material at Earth's magnetosheath (Robertson & Cravens 2003). The highly ionized atoms in the solar wind collide with the neutral material and pick up electrons in excited states from which they radiatively decay. In the MOS energy band this includes emission from C VI, O VII, O VIII, Ne IX, and Mg XI some of which are commonly used for plasma temperature, density, and ionization equilibrium diagnostics.

Figure 6 shows the example of SWCX emission from Snowden et al. (2004), an analysis of four observations of the Hubble Deep Field North (HDF-N). Displayed are two spectra from the same direction collected at different times (separated by two weeks). Since the cosmic background does not vary with time, the spectra should be the same except for the possibility of SP contamination which would be a continuum enhancement rather than the clear emission lines. The O VII (0.56 keV) and O VIII (0.65 keV) lines are particularly clearly seen as excesses. For about 40 ks of the contaminated observation there was no significant indication in the 0.5−0.75 keV light curve that there was anything unusual happening. If there were no other observations of the HDF-N and if the contaminated observation lasted only for that 40 ks period, there would have been no reason a priori to suspect the data.

Since some fraction of the SWCX emission is due to the interaction of the solar wind with the ISM flowing through the solar system, SWCX emission must, at some level, contaminate all observations. The contamination depends upon the look direction and the strength of the solar wind. Usually, the temporal variation in the SWCX is smaller than the uncertainty in the data, but is occasionally significantly stronger. In a study of

"empty field" lines of sight having multiple observations, KS07 found significant SWCX contamination in 12 of 46 observations. Of the large survey region near $\alpha, \delta \sim 02^{h}25^{min}, -03^{\circ}$, 5 of 26 observations show significant SWCX contamination. This suggests that 10% to 25% of observations may have significant SWCX contamination.

3.3.1. Treatment of the SWCX background

Because the SWCX emission originates externally to the satellite and is unlikely to show any angular structure in the *XMM-Newton* FOV, it is inseparable from the cosmic background. Depending on the length of the observation and the specific SWCX occurrence, the contamination may or may not be detectable in the observation light curve. The emission is at energies less than 1.5 keV, primarily in the 0.5−1.0 keV band, so a light curve of that band may show variation in the diffuse count rate while the light curve in the hard band (2.0−8.0 keV) would not. SWCX contamination may also be detectable in the spectrum. There can be very strong O VIII and Mg XI emission unfittable by any normal equilibrium or normal abundance plasma models. There are also certain observation geometries which may be more susceptible to SWCX contamination than others, specifically any line of sight which passes near the subsolar point of Earth's magnetosheath (Robertson & Cravens 2003).

3.4. Cosmic X-ray background

The CXB is comprised of many components which vary considerably over the sky. At high energies ($E > 1$ keV) and away from the Galactic plane the dominant component is the extragalactic power law. Most of this power law represents the superposition of the unresolved emission from discrete cosmological objects (i.e., AGN). There is considerable discussion concerning the uniformity of this emission over the sky and what the true form of the spectrum is (e.g., whether the slope changes for energies less than 1 keV, Tozzi et al. 2006). The contribution of this component to the observed spectrum is clearly going to be dependent on the extent to which point sources have been excluded from the analysis. The emission is also absorbed by the column of Galactic material along the line of sight.

At lower energies there is a greater variety of components, most of which have thermal emission spectra. In the solar neighborhood the Local Hot Bubble (LHB, Snowden et al. 1998, and references therein) provides the dominant contribution near $\frac{1}{4}$ keV. The LHB is a region of hot plasma ($T \sim 10^6$ K) at least partially filling an irregularly shaped cavity in the neutral material of the Galactic disk surrounding the Sun with a radial extent of ~30 pc to over 100 pc (preferentially extended out of the plane of the Galaxy). In the halo of the Galaxy there is additional plasma with $T \sim 10^6$ K. The distribution of this plasma is quite patchy and probably has a relatively low scale height. There is additional general diffuse emission at $\frac{3}{4}$ keV which may be associated with the Galactic halo or perhaps the local group (McCammon et al. 2002; Kuntz et al. 2001). Except for the emission from the LHB, these components are all absorbed by the column density of the Galactic ISM.

Also contributing to the cosmic X-ray background are a wide variety of distinct Galactic objects, some of which subtend large angles on the sky. Loop I is a nearby superbubble which has a diameter of ~100°, and its emission is combined with the Galactic X-ray bulge which extends to $|b| > 45^{\circ}$. There are supernova remnants, the Galactic ridge, and the unresolved emission from stars all contributing to the CXB with varying spectra affected by varying amounts of absorption. The CXB at $\frac{1}{4}$ keV, $\frac{3}{4}$ keV, and 1.5 keV can vary by an order of magnitude over the sky, and it can vary independently between those bands (although to a lesser extent for the $\frac{3}{4}$ keV and 1.5 keV bands). Figure 7 displays the *ROSAT* All-Sky Survey (RASS) sky maps in the $\frac{1}{4}$ keV, $\frac{3}{4}$ keV, and 1.5 keV band from Snowden et al. (1997). Comparison of the $\frac{1}{4}$ keV and $\frac{3}{4}$ keV maps demonstrates the likely unsuitability of average blank sky data to sufficiently characterize the sky in any particular direction.

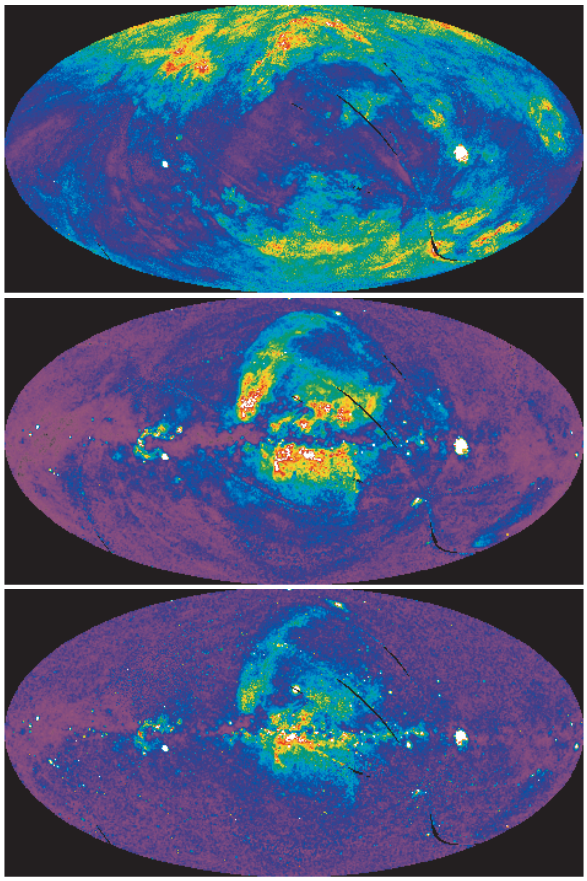

Fig. 7. All-sky maps in the $\frac{1}{4}$ keV (*upper*), $\frac{3}{4}$ keV (*middle*), and 1.5 keV (*lower*) bands from Snowden et al. (1997) in an Aitoff-Hammer projection with the Galactic center at the center with longitude increasing to the left. Red and white indicate higher intensities while purple and blue indicate lower intensities.

3.4.1. Treatment of the Cosmic X-ray background

The CXB is the dominant background component at energies less than 1.35 keV, i.e., below the Al Kα and Si Kα FX lines. It is significant in all directions and it can not be modeled as a single spectrum independent of position on the sky. The variation in both spectral shape and magnitude makes it very problematic to separate from the source of interest when the source covers a large fraction or all of the instrument FOV. This is particularly troublesome for the study of objects like clusters of galaxies where the source emission fades into the background at an uncertain rate and radius. As noted in the introduction, several unanswered scientific questions are dependent on the true temperature radial profile and mapping that profile to the greatest possible radius is critical.

In the absence of an otherwise source-free region within the field of view there is no way to directly subtract the CXB from the source spectrum. And, as noted above, the use of blank-field data as a spectral template may be inappropriate. For this reason, the CXB should be modeled as part of the fitting process. Unfortunately, it is easy to transfer significant power between the various background components of a source with low surface brightness. It is therefore desirable to constrain the fits to the greatest extent possible. One method for doing so for the CXB is to use spectra from the *ROSAT* All-Sky Survey. A publicly-available tool[2] at the High Energy Science Archive Research Center (HEASARC) extracts seven-channel spectra from the data of Snowden et al. (1997) for user-defined regions (circular or annuli). These data can be simultaneously fit, after proper correction for the observed solid angle, with the *XMM-Newton* MOS data by a standard model for the CXB. For example (and this will be demonstrated in Sect. 4 below for Abell 1795) a CXB RASS spectrum can be extracted for an annulus surrounding the cluster, but not including it. With the assumption that the annulus spectrum is a good representation of the CXB in the direction of the cluster, a model including 1) an unabsorbed ~0.1 keV thermal spectrum representing the LHB; 2) an absorbed ~0.1 keV thermal spectrum representing the cooler Galactic halo emission; 3) an absorbed ~0.25 keV thermal spectrum representing the hotter halo emission (and/or emission from the local group); and 4) an $E^{-1.46}$ power law representing the unresolved cosmological emission (e.g., Kuntz & Snowden 2000) can be fit to the RASS and MOS data, with additional components representing the cluster, SP, and FX components fit only to the MOS data.

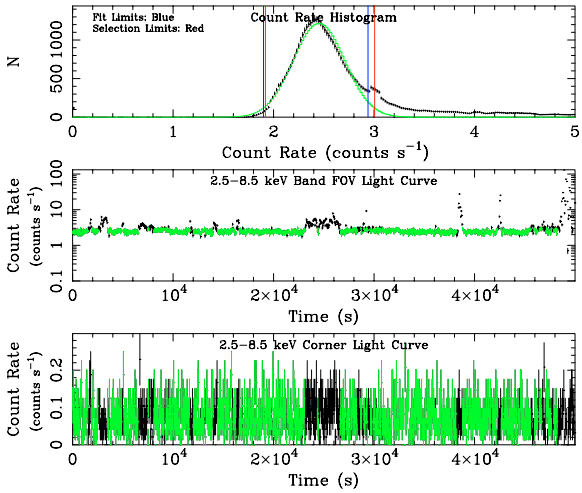

Fig. 8. Temporal filtering results for the MOS1 Abell 1795 cluster observation with ObsID 0097820101. The *upper panel* plots the light curve histogram for the 2.5−12.0 keV band from the FOV, the *middle panel* displays the 2.5−12.0 keV band FOV light curve, and the *lower panel* displays 2.5−12.0 keV band light curve from the unexposed corners of the instrument. The histogram is derived from the smoothed light curve. In the *upper panel*, the blue vertical lines show the range for the Gaussian fit, the green curve shows the Gaussian fit, while the red vertical lines show the upper and lower bounds for filtering the data. In the bottom two panels green points indicate accepted data while black points indicate data excluded by the filtering algorithm. The high count rate excursions are produced by soft protons rather than a particle background flare as the latter case would produce a similar increase in the corner data.

4. Abell 1795 – A case study

Abell 1795 is a well-studied nearby cluster of galaxies. It was chosen for the example presented here as it was used by Nevalainen et al. (2005) for their discussion of the analysis of *XMM-Newton* observations of extended objects. The observation (ObsID 0202130101) was taken on 2000 June 26 with an exposure of ~49.6 ks. The pointing direction was α, δ = 207.2208°, 26.5922°.

The preparation of the data for analysis presented below uses the XMM-ESAS[3] package of perl scripts and FORTRAN programs, which also require The XMM-Newton Standard Analysis Software (SAS[4]) package. XMM-ESAS was prepared by the NASA/Goddard Space Flight Center XMM-Newton Guest Observer Facility (GOF) in conjunction with the ESA Science Operations Center (SOC) and the Background Working Group. The software is publicly available through both the GOF and SOC and is provided with documentation.

4.1. Temporal filtering

The Abell 1795 observation was relatively clean by visual observation of its light curve with just a few excursions to high count rates from SP contamination. Figure 8 shows the results from the temporal filtering algorithm. Filtering the data reduced the exposure to 36.5 ks, roughly 75% of the original observation. However, the slight ripple in the light curve indicates that there is likely to be some residual SP contamination.

In the screening process a light curve with a 1 s binning in the 2.5−8.5 keV band was first created from the photon event file (PEF). This light curve, binned by 50 s, is shown in the middle panel of Fig. 8. The light curve is smoothed with a 50 s running average and a histogram created from the smoothed data (upper panel). The presence of the SP contamination is shown by the high count-rate tail of the of the otherwise relatively Gaussian distribution. That the flaring in the light curve is not caused by an increase in the high-energy particle background is shown by the corner count rate (lower panel) not having similar enhancements. The histogram is searched for the maximum and a Gaussian is fit to the data surrounding the peak. A count-rate cut of the light curve is made by setting thresholds at $\pm 1.5\sigma$ on either side of the fitted peak channel. Note that the setting of these thresholds is somewhat arbitrary, and that there is no absolute answer. With cleaner data wider limits can be set, but there is always a trade-off between the amount of accepted data and how clean those data are.

4.2. Extraction of spectra

After the data were screened spectra were extracted and model background spectra created. For this analysis of Abell 1795 the goal is the determination of the temperature radial profile, thus the extracted spectra were from concentric annuli.

Extraction selection expressions consistent with the requirements for the SAS task *evselect* were required for the annuli. These were most easily created using SAS and the *xmmselect* task and its interface with the *ds9*[5] (Joye & Mandel 2003) image

[2] http://heasarc.gsfc.nasa.gov/cgi-bin/Tools/xraybg/xraybg.pl

[3] http://heasarc.gsfc.nasa.gov/docs/xmm/xmmhp_xmmesas.html

[4] http://xmm.esac.esa.int/external/xmm_sw_cal/sas_frame.shtml

[5] http://hea-www.harvard.edu/RD/ds9/

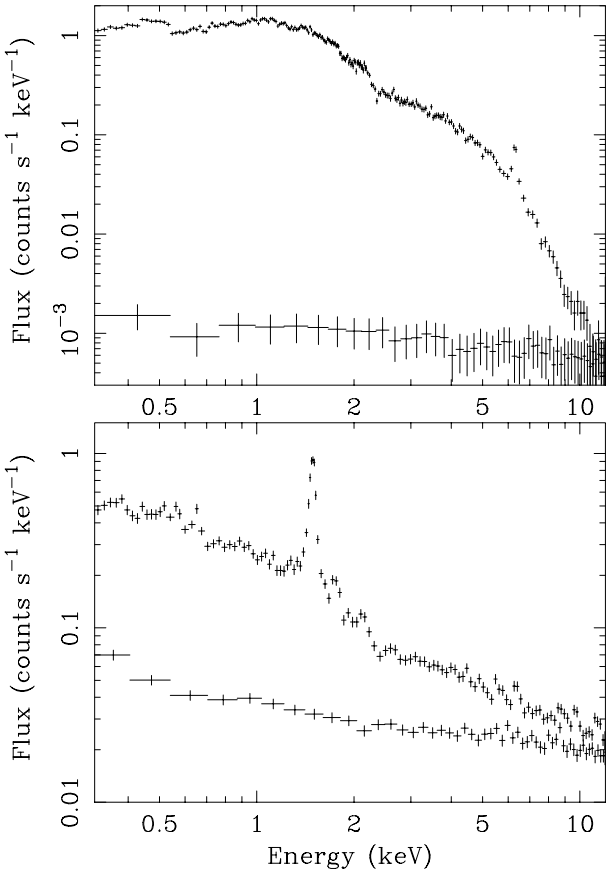

Fig. 9. Spectra from two annuli from the Abell 1795 analysis, 1′−2′ (*upper panel*) and 10′−15′ (*lower panel*). In each panel the upper spectrum is the total spectrum while the lower spectrum is the modeled QPB spectrum. The data have not been normalized for solid angle, otherwise the 1′−2′ spectrum would be relatively brighter by about two orders of magnitude.

display software. From *xmmselect* an image was created in detector coordinates (*DETX* and *DETY*). The detector coordinates of the center of Abell 1795 were determined from the image, and then the desired region descriptions defined. As an example of the region selection descriptors,
((DETX, DETY) IN circle(201, −219, 2400))
&&!((DETX,DETY) IN circle(201, −219, 1200))
selects data from the MOS1 detector from the 1′−2′ annulus. The numbers 201 and −219 are detector coordinates (*DETX* and *DETY*) of the cluster center while the numbers 1200 and 2400 are the inner and outer radii of the annulus, all in units of 0.05 arcsec. The annulus is created by selecting all data within the first circle but not within the second circle (the "&&" symbol is used for the Boolean "and" and the "!" symbol is used for the Boolean "not"). Note that the DETX and DETY positions for a given sky position in the MOS1 and MOS2 detectors will be different.

4.3. Modeling the particle background

The model particle spectra were created using the XMM-ESAS package which follows the process as outlined in Sect. 3.1 above. Figure 9 displays total and model QPB spectra from an inner and an outer annulus of the Abell 1795 analysis. As expected the fainter outer annulus is much more strongly affected by the various background components, in particular the FX contamination

Table 1. Spectral model definitions.

Parameter	Definition
P_1	Power law representing the residual SP contamination.
G_1, G_2	Gaussians representing the Al Kα and Si Kα FX lines.
C_1, C_2	Constants representing the different solid angles of the extraction annuli and calibration offsets between the two detectors.
A_1	CXB LHB thermal component.
A_2	CXB cooler halo thermal component.
A_3	CXB hotter halo thermal component.
P_2	CXB extragalactic power law component.
$N_{\rm Hg}$	Column density of Galactic hydrogen.
AC	Cluster thermal component.
$N_{\rm Hc}$	Column density foreground to the cluster, includes both Galactic hydrogen and material associated with the cluster.

is clearly represented by the Al-Kα line and the residual SP contamination which is responsible for the difference between the spectra above $E \sim 8$ keV.

4.4. Modeling the cosmic background

Modeling and constraining the CXB was a two-part process. First, the RASS spectrum of the CXB in the direction of interest was obtained from the HEASARC "X-ray Background Tool" (see Sect. 3.4.1 above). Since the object of interest in this analysis is a discrete object and not the CXB itself, an annular extraction region was used where the inner annulus radius was large enough to exclude cluster emission. The outer annulus radius was limited so that the spectrum could be as appropriate as possible for the cluster region (and in addition so that the *ROSAT*-spectrum statistics would not dominate the spectral fitting process). For this analysis of Abell 1795, inner and outer radii of 1° and 2°, respectively, were used.

4.5. The Fitted Spectral Model

The model for this example (below and Table 1) is rather extensive as it represents most of the emission components along the line of sight to and including the Abell 1795 cluster as well some local background components. To complicate the process even further, the fitted parameters for some of the components will differ between the different annuli.

$$S = P_1 + G_1 + G_2 + C_1 \times C_2 \times (A_1 + (A_2 + A_3 + P_2) \times e^{-\sigma N_{\rm Hg}} + AC \times e^{-\sigma N_{\rm Hc}})$$

The equation above for the fitted spectrum includes a fairly complete model for the non-cluster component of the observed spectrum in the cluster analysis. P_1 is a power law representing the residual SP contamination. This is not folded through the instrumental effective areas. G_1 and G_2 are Gaussians which represent the Al Kα and Si Kα FX lines. C_1 and C_2 are constant scale factors which represent the different solid angles of the extraction annuli and any relative calibration offsets between the two detectors. For consistency with the RASS data, the C_1 parameter is set to the solid angle in units of square arc minutes (in practice, this is the spectrum BACKSCAL keyword value produced by SAS

Table 2. Spectral fit parameters.

Spectral component	Model component	Parameter	Initial guess	Initial constraint	Final constraint
SP	P_1	γ_1	0.9	Fix	Free
–	–	Normalization	10^{-5}	Free	Free
FX	G_1	Energy	1.49 keV	Fix	Free
–	–	Width	0.0 keV	Fix	Free
–	–	Normalization	10^{-5}	Free	Free
FX	G_2	Energy	1.75 keV	Fix	Free
–	–	Width	0.0 keV	Fix	Free
–	–	Normalization	10^{-5}	Free	Free
Scale	C_1	Solid Angle	Set	Fix	Fix
Scale	C_2	Scale Factor	1.0	Fix	Fix/Free[a]
CXB[b]	A_1	kT	0.1	Fix	Free
–	–	Normalization	5.0×10^{-6}	Free	Free
–	A_2	kT	0.1	Fix	Free
–	–	Normalization	5.0×10^{-6}	Free	Free
–	A_3	kT	0.25	Fix	Free
–	–	Normalization	10^{-6}	Free	Free
–	P	γ	1.46	Fix	Fix
–	–	Normalization	8.88×10^{-7}	Fix	Fix/Free[c]
–	$N_{\rm Hg}$	Galactic Column	1.2×10^{20}	Fix	Free
A1795	A_4	kT	5.0 keV	Free	Free
–	–	Abundance	0.5	Free	Free
–	–	Redshift	0.06	Free	Free
–	–	Normalization	5.0×10^{-4}	Free	Free
–	$N_{\rm Hc}$	Cluster Column	1.2×10^{20}	Fix	Free

[a] The MOS1 and RASS scale factors were fixed at 1.0 and the MOS2 scale factor was allowed to vary.
[b] The abundances and redshifts of the cosmic thermal components are fixed at 1.0 and 0.0, respectively.
[c] Whether the extragalactic power law normalization is fixed or allowed to vary must be carefully examined.

divided by 1 440 000). The cosmic background is represented by the three thermal components A_1 for the LHB, A_2 for the cooler halo component, A_3 for the hotter halo component, and the extragalactic power law, P_2. $N_{\rm Hg}$ is the column density of Galactic neutral hydrogen. To model the cluster emission we use a simple absorbed thermal model where the abundance (a single overall scaling) and absorption are allowed to vary. The spectral fitting is done using the Xspec package with Astrophysical Plasma Emission Code (APEC[6]) thermal models and the Morrison & McCammon (1983) absorption model (Wisconsin Absorption, WABS).

4.6. The data

For this analysis we extracted data from 10 annuli for the cluster. These are the same annuli which are used for the rest of the clusters in this catalog. The size of the annuli were chosen to be reasonable, where reasonableness in this, and most cases, is not unique. The dominant constraint is that the number of events in a specified annulus must be sufficient for a significant spectral fit.

4.7. The fit

The setting up of the spectral fit was a time-consuming process. For the number of spectra (20 MOS1 and MOS2 spectra and 1 RASS spectrum) and the complex model used for the fit, there are 546 parameters. Clearly if all 546 parameters are fit independently convergence of the fit would take place only on geologic time scales. However, many of the parameters can be either linked or frozen to known values, some of which may be later allowed to vary once the fit is relatively accurate. (It is occasionally easy for the fitting engine to get "stuck" in a local minima.) The cosmic background is the same for all spectra and so the parameters can be linked (the redshifts and abundances of the thermal components were frozen to 0.0 and 1.0, respectively). The solid angle scale factors were frozen to their appropriate values and the instrument scale factors were linked. The normalizations for the SP contributions were linked using the model distribution available in the XMM-ESAS package and the power law index was also linked. For the cluster contribution to the spectra, the redshift can be linked. Table 2 lists suggested initial parameters and whether they should be frozen (fix) or allowed to vary (free). In practice, the abundances for many of the outer annuli were effectively unconstrained. In such cases the abundance of the outer most annulus with a free abundance was linked to that of the next inner annulus and the data refit. This process was repeated until a S/N of ~3 was achieved. In addition, abundances which went to unphysical values, e.g., zero, were also linked to that of the next inner annulus.

There are further complications to the fitting process. First, because of the finite PSF of the EPIC instruments, some X-rays which originate in one annulus on the sky are detected in a different annulus. In cases where there are strong spectral gradients, e.g., for clusters with a strong cooling flow, this can significantly affect the results with the inner annulus having a higher fitted temperature and the neighboring annuli having cooler fitted temperatures than their true values. The fitted value for the flux is also likely to be different than the true value. The arfgen task of SAS now has the capability (using the crossregionarf parameter) of calculating the "cross-talk" effective area file (ancillary region file, ARF) for X-rays originating in one region but which are detected in another. The cross-talk contribution to the spectrum of a given annulus from a second annulus is treated in Xspec V12 as an additional model component. The spectrum

[6] http://cxc.harvard.edu/atomdb/sources_apec.html

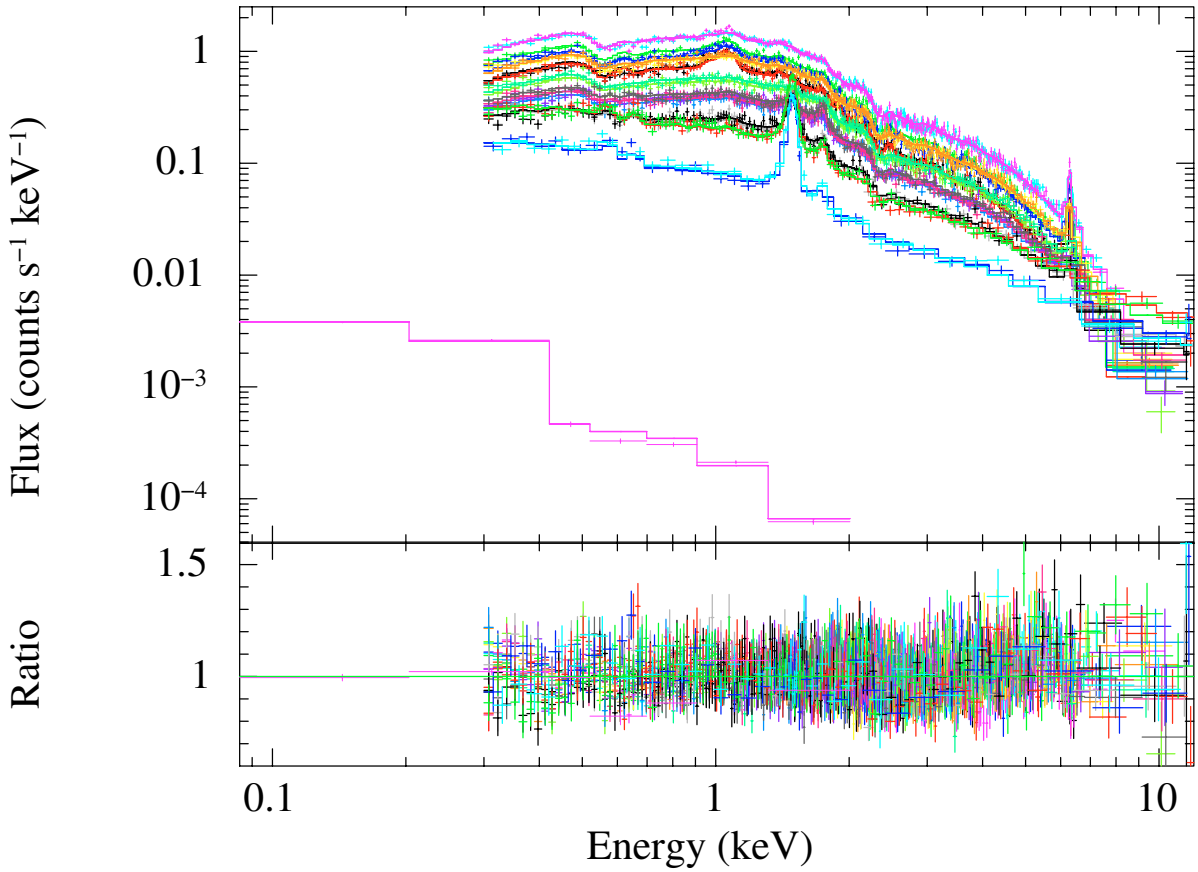

Fig. 10. Spectral fit to the data from Abell 1795. MOS1 and MOS2 spectra are shown for all ten annuli, as well as the *ROSAT* spectral energy distribution. The *lower panel* shows the ratio of the data to the model and demonstrates that the fit is reasonably good over the full dynamic range.

from the second annulus is folded through the cross-talk ARF linking the two annuli and then the redistribution matrix (RMF) of the first annulus. Note that the ARF for the contributions of X-rays originating in one region of the sky to a second region on the detector is typically not the same as the ARF for the contribution of X-rays originating in the second region on the sky to the first region on the detector. Second, the use of Xspec V12 requires that the SP power law be included as a separate model with a separate response matrix. This response matrix is diagonal with unity elements. For the cluster analysis presented here we fitted the *XMM-Newton* spectra over the 0.3−12.0 keV energy range where statistics permitted. Quite often the range was limited to 0.3−10.0 keV.

4.8. Abell 1795 results

The final fit for the Abell 1795 data is relatively good with a χ^2 value of 1.25 for 3958 degrees of freedom. The data, model fits, and residuals are shown in Fig. 10. However, the distribution of the residuals does show some systematic variation with energy, most noticeably at energies above 2 keV. The variation is rather limited in extent and could be due to the simplicity of the model for the cluster emission, residual calibration errors, or errors in the model background (both QPB and SP). The latter is less likely as all annuli show the systematic, including the inner ones which are not significantly affected by backgrounds.

Figure 11 shows the comparison between the *Chandra* (Vikhlinin et al. 2005), *XMM-Newton* (Nevalainen et al. 2005), and current analysis of Abell 1795. As expected, there is reasonable agreement between the *XMM-Newton* results. However,

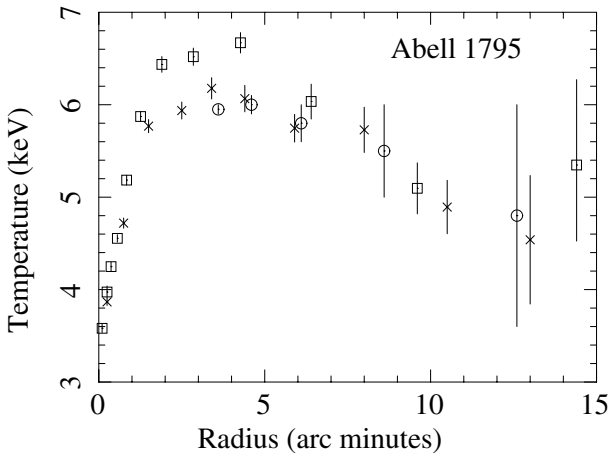

Fig. 11. Comparison of results for the A1795 temperature radial profile from *Chandra* (square, Vikhlinin et al. 2005), and *XMM-Newton* analysis from Nevalainen et al. (2005) (circle) and this analysis (cross). The radii for the *XMM-Newton* points have been slightly offset in the plot for clarity.

the *Chandra* results are very significantly different from those of *XMM-Newton* at intermediate radii. This discrepancy is consistent for the higher temperature clusters which have been compared. The sense of the difference is that the higher the fitted temperature the more likely it is that *Chandra* will find a higher temperature than *XMM-Newton* with the effect typically becoming significant above $kT \sim 5$−6 keV. Figure 12 displays this difference in the fitted temperatures for clusters in their ∼1′−5′

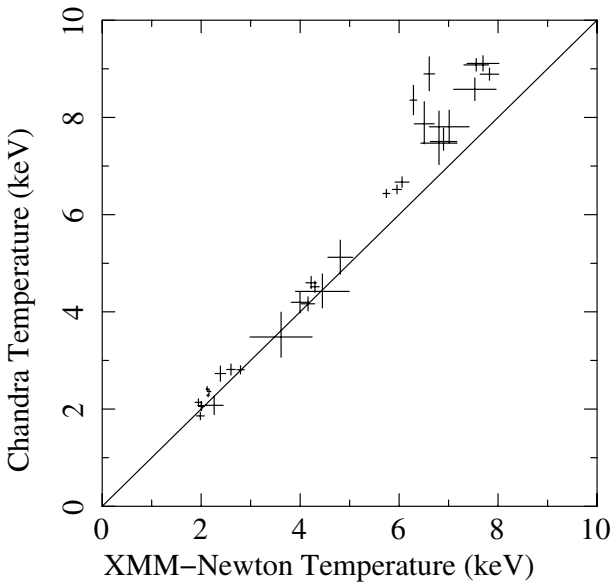

Fig. 12. Comparison of results for the temperature radial profiles for various clusters in their ∼1′−5′ annuli from *Chandra* (Vikhlinin et al. 2005) and *XMM-Newton* (this analysis).

annuli (*Chandra* data from Vikhlinin et al. 2005). These annuli are used for comparison purposes since their signal to noise ratio are high, the effects of background subtraction is minimal, and the PSF issues are minor. This discrepancy between *Chandra* and *XMM-Newton* can lead to significant differences in the fitted temperature profiles causing the *Chandra* observations to have greater fall-offs in temperature at higher radii.

One suggested explanation for the discrepancy was the effect of the finite PSF of *XMM-Newton* and the spreading of the cooler X-rays from the cluster core to the inner annuli. Indeed, this is what led to the development of the arfgen modification to account for the cross-talk. While the correction effect does go in the right direction (Fig. 13, top panel), for Abell 1795 it is barely significant and not nearly sufficient to account for the difference. Also, use of the *Chandra* image with its finer PSF for the calculation of the cross-talk contribution has no significant effect. However, the effect can be significant in cases where the flux and temperature gradients are steeper (on an angular scale) and greater in magnitude. Figure 13 (bottom panel) shows a similar comparison for the cluster Abell 2204. In this case the fitted temperature of the second annulus increases by ∼1.5 keV when the correction for PSF smearing is applied.

In an effort to improve the cross-calibration between the MOS, pn, and RGS detectors, new quantum efficiencies were released in 2007 August[7]. The revisions decrease the effective area of the response at lower energies by increasing the absorption depth at the C, N, and O edges. In order to gauge the significance of the change on the results reported in the cluster catalog, we reprocessed seven clusters with a range of temperatures with SAS V7.1 and the calibration files of 2007 September 14. Figure 14 shows the ratio of the reprocessed versus the cluster catalog temperatures. There is a tendency for the reprocessed temperatures to be slightly lower although only at the $\sim 1\sigma$ level. The average ratio is ∼0.97, or ∼0.2 keV at 6 keV.

[7] `http://xmm.esac.esa.int/docs/documents/CAL-SRN-0235-1-0.ps.gz`

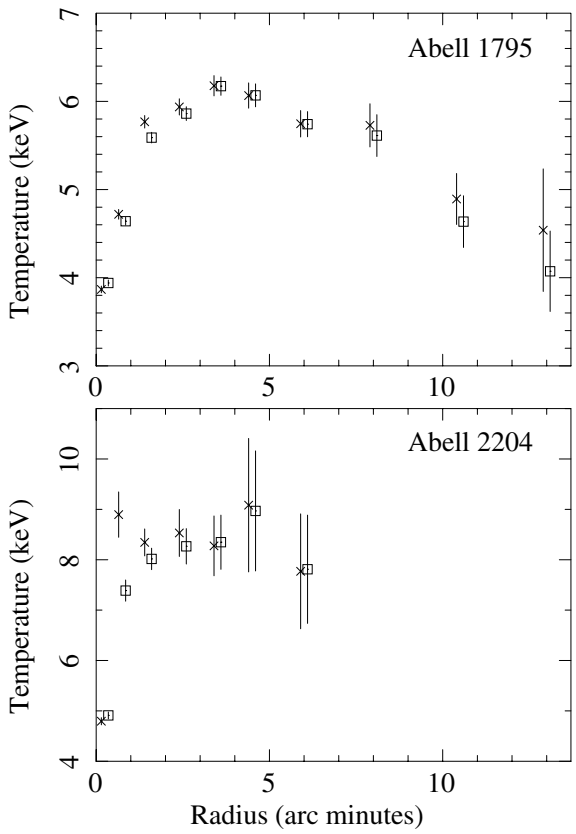

Fig. 13. Comparison of results for the Abell 1795 (*top panel*) and Abell 2204 (*bottom panel*) temperature radial profiles from analysis including (cross) and not including (square) the effect of PSF smearing (crosstalk between adjacent annuli). The radii have been slightly offset in the plot for clarity.

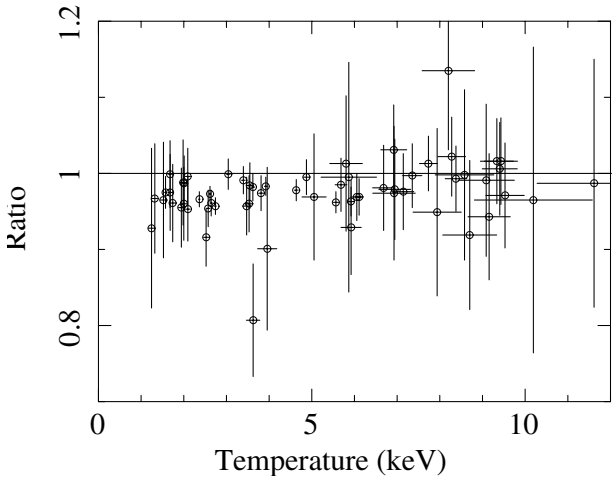

Fig. 14. Ratio of the fitted temperatures for a selection of clusters analyzed using SAS V7.1 and the calibration files of 2007 September versus the calibration used for the cluster catalog. The horizontal line is set at a ratio of 1.0.

5. The cluster catalog

We applied the method described above for the Abell 1795 data to 70 clusters of galaxies from the *XMM-Newton* archive in a consistent manner. The selection of the clusters was empirical; postage-stamp count images from the *ROSAT* All-Sky Survey were examined for each of the *XMM-Newton* cluster observations in the archive. Those which appeared to have (subjectively)

Table 3. Annuli definitions.

Annulus	Inner Radius	Outer Radius
1	0′	0.5′
3	0.5′	1′
3	1′	2′
4	2′	3′
5	3′	4′
6	4′	5′
7	5′	7′
8	7′	9′
9	9′	12′
10	12′	14′

Inner and outer radii in arc minutes of the annuli used in the analysis of the clusters presented here.

reasonable extent and reasonable brightness were chosen for processing. A total of just over 100 clusters were selected.

The initial step of the processing was to filter the data to exclude periods of SP flaring and to create count images. Clusters where the accepted exposure time was less than ∼8 ks as well as clusters with a surface brightness insufficient to produce reasonable statistics for the cluster emission were excluded from further analysis. The selection against overly contaminated observations excluded ∼30 clusters. For those observations with filtered times acceptable for processing, roughly 25% of the original processing time was lost on average to flaring. (This loss does not include the useless exposures of observations with multiple exposures.) A few other clusters were excluded from the processing because of their extreme asymmetry or the presence of strong substructures obviating the circular assumption.

For the accepted observations, the center of the cluster was determined from an image, bright point sources were manually excluded (typically to the level of a few times 10^{-13} erg cm^{-2} s^{-1}, but the level varied due to the brightness and angular extent of the cluster), and the data were processed to produce spectra for the ten annuli listed in Table 3 for both MOS detectors. The count images in the 0.2−1.0 keV band were examined for evidence of the individual CCDs operating in an anomalous state (KS07). If so, the individual CCD was excluded from the spectral extraction. The HEASARC X-ray Background Tool was used to create RASS spectra in, typically, a 1−2 degree annulus around the cluster. For a few cases (e.g., the Coma and Virgo clusters) the annulus had to be increased in size to fully exclude the cluster. The X-ray Background Tool also provided the column density of Galactic H I which was fixed in the spectral fits. The analyzed clusters are listed in Table 4. Included in the table are the fitted X-ray redshifts, *XMM-Newton* observation identification (ObsID), accepted and initial exposures, and the surface brightness limits for the image color bar scalings in Figs. 36 through 42 of the electronic (on-line) version of this paper.

In order to test the reliability of our analysis methods we use second observations of the clusters Abell 1835, Sérsic 159-3 and Perseus for comparisons. (Note that the second observation of Sérsic 159-3 is under the alternate name AS 1101 and the second observation of Perseus is under the alternate name Abell 426). Figure 15 shows the fitted temperatures which are in very good agreement. Along with our Sérsic 159-3 results we have plotted the CIE (which are more equivalent to our spectral fitting) results from de Plaa et al. (2006). These data are also in reasonable agreement except at higher radii where background subtraction is more problematic and at radii at 0.5−2′ where the cross-talk effect is strongest. The fitted temperatures for the Perseus cluster

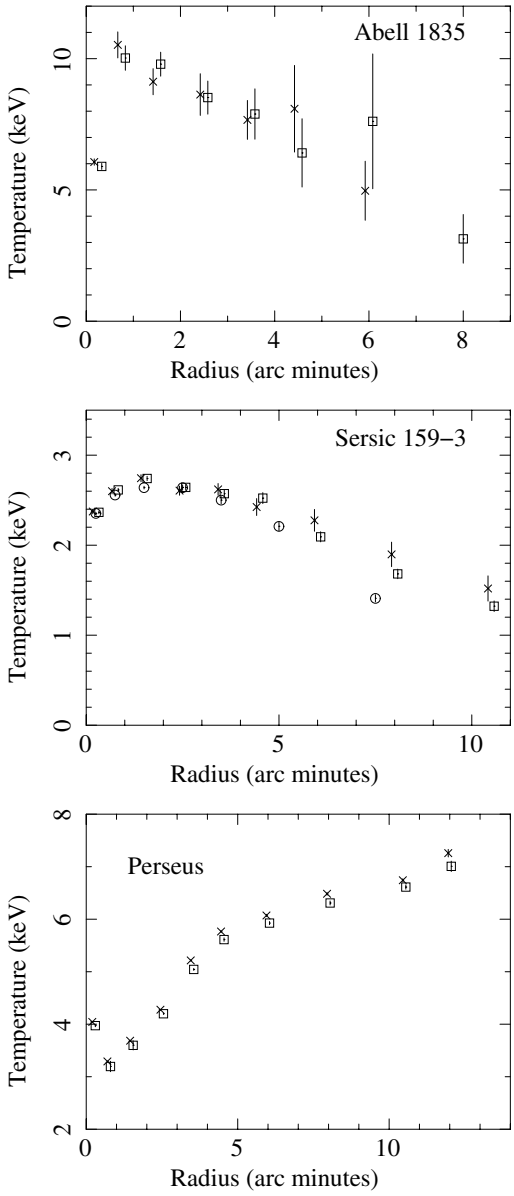

Fig. 15. Comparison of temperature radial profile results for the two observations of Abell 1835 (*upper panel*), Sérsic 159-3 (*middle panel*), and Perseus (*lower panel*). The radii have been slightly offset in the plot for clarity. For the Sérsic 159-3 plot the CIE results of de Plaa et al. (2006). In all panels the box and cross symbols represent the results of this paper while in the *middle panel* the circle symbols represent the de Plaa et al. (2006) results.

do so a slight but significant systematic difference with one observation having consistently higher temperatures by ∼0.15 keV. However, as the Perseus cluster is very bright, it is very unlikely that this systematic difference was caused by errors in the background modeling.

We have tested the robustness of our results to variations in the assumed emission abundance model. As noted above, for the cluster catalog analysis we use Anders & Grevesse (1989) abundances allowing only a single scale factor. We refit the data for four clusters (Abell 665, Abell 1060, Abell 1795, and 2A 0335+096) using Lodders (2003) abundances with the results shown in Fig. 16. The fits were of similar quality and the only significant difference were the values of the fitted abundances, which were consistent with a simple scaling by a factor

Table 4. Clusters.

Cluster	Redshift	ObsID	Filtered exposure (s)	Original exposure (s)	0.35–1.25 keV band scaling (cnts s^{-2} deg^{-2})	2.0–8.0 keV band scaling (cnts s^{-2} deg^{-2})	χ^2_ν	ν
2A 0335+096	0.0329	0147800201	74 890.7	95 962.0	4500	1700	1.48	5002
A13	0.1035	0200270101	33 379.5	33 870.7	200	120	1.03	1063
A68	0.2481	0084230201	23 818.7	29 567.6	350	200	1.25	704
A85	0.0520	0065140101	12 012.2	12 524.4	5000	1800	2.02	1836
A133	0.0575	0144310101	19 042.1	33 670.5	2800	700	1.17	1306
A209	0.2116	0084230301	16 847.6	21 796.1	400	290	0.99	643
A262	0.0140	0109980101	22 256.9	23 897.0	1900	200	1.26	2067
A383	0.1874	0084230501	25 444.9	33 379.3	3000	1000	1.08	942
A399	0.0644	0112260101	10 807.6	14 297.6	200	200	1.03	809
A400	0.0220	0404010101	29 906.9	38 620.9	200	130	1.10	1431
A478	0.0808	0109880101	49 696.1	56 249.2	3500	4000	1.27	4913
A496	0.0293	0135120201	15 845.2	29 448.0	3500	1400	1.19	2625
A520	0.1946	0201510101	27 227.4	46 371.6	200	150	1.15	1140
A576	0.0420	0205070301	87 52.0	21 671.3	300	140	1.04	528
A665	0.1788	0109890501	49 696.9	78 487.2	500	300	1.21	2117
A773	0.2161	0084230601	12 332.1	15 082.8	350	300	1.28	464
A1060	0.0131	0206230101	32 724.8	63 773.6	400	200	1.24	3165
A1068	0.1471	0147630101	19 188.9	29 669.0	1000	400	1.03	852
A1413	0.1349	0112230501	23 397.2	25 922.4	1000	500	1.09	1311
A1589	0.0722	0149900301	15 121.6	17 170.7	150	50	1.19	550
A1650	0.0812	0093200101	34 006.0	42 534.0	1200	800	1.10	2470
A1689	0.1809	0093030101	34 530.0	39 169.6	2700	1900	1.17	2031
A1775	0.0754	0108460101	22 065.8	32 003.9	500	200	1.18	1042
A1795	0.0614	0097820101	35 144.6	50 011.7	5000	2000	1.25	3958
A1835	0.2490	0098010101	24 849.0	40 635.5	4000	2000	1.12	1301
A1835 a[8]	0.2454	147330201	27 895.1	83 817.3	–[9]	–	1.17	1465
A1837	0.0663	0109910101	46 233.9	49 031.5	500	200	1.14	1529
A1914	0.1735	0112230201	19 219.6	25 571.4	1000	700	1.15	1334
A1991	0.0642	0145020101	22 620.9	41 790.5	2000	500	1.33	1184
A2029	0.0728	0111270201	11 088.8	17 846.7	4000	3000	1.18	2195
A2052	0.0333	0109920101	28 743.7	30 397.0	4000	1000	1.37	2759
A2065	0.0728	0202080201	19 205.3	33 870.7	800	500	1.09	1444
A2163	0.2021	0112230601	10 177.1	15 766.7	400	550	1.16	760
A2199	0.0277	0008030201	14 190.8	20 051.5	2500	1000	1.24	2745
A2204	0.1512	0112230301	18 367.1	22 097.7	4000	3000	1.30	1687
A2218	0.1723	0112980101	17 673.1	18 169.1	300	200	1.30	709
A2256	0.0530	0141380201	10 233.8	18 369.3	300	200	1.24	987
A2319	0.0519	0302150101	15 145.8	16 668.9	650	650	2.51	2672
A2589	0.0417	0204180101	22 934.0	46 670.6	400	200	1.10	1574
A2597	0.0804	0147330101	46 726.9	104 451.1	5000	2000	1.13	2388
A2626	0.0549	0148310101	38 306.4	41 119.6	1000	400	1.11	1746
A2667	0.2205	0148990101	17 682.8	30 914.4	3500	1500	1.21	863
A2717	0.0510	0145020201	47 414.8	54 010.5	500	100	1.20	1668
A3112	0.0723	0105660101	22 271.5	23 247.0	6000	2500	1.24	1919
A3158	0.0609	0300210201	19 076.9	22 149.7	400	300	1.37	1755
A3526	0.0054	0046340101	43 699.3	47 182.9	5000	1000	2.32	5031
A3558	0.0459	0107260101	40 643.4	44 026.4	600	400	1.23	3601
A3560	0.0429	0205450201	27 009.7	45 271.8	150	70	1.10	1261
A3581	0.0225	0205990101	33 930.6	43 670.2	2400	500	1.40	2206
A3827	0.0959	0149670101	21 024.9	24 970.8	500	400	1.23	1437
A3888	0.1537	0201903101	23 250.1	30 469.8	500	400	1.08	1564
A3911	0.0958	0149670301	22 883.3	27 269.2	200	150	1.02	1236
A3921	0.0919	0112240101	28 488.8	30 763.6	400	300	1.10	1467
A4059	0.0467	0109950201	22 581.2	24 398.8	1200	400	1.18	1952
AWM 7	0.0155	0135950301	29 418.7	31 621.6	1000	500	1.35	3793
Coma	0.0218	0124711401	16 195.8	23 598.0	500	300	1.15	3692
E1455+2232	0.2583	0108670201	33 785.9	39 993.7	1600	1800	1.25	1100
EXO0422	0.0336	0300210401	38 373.1	41 070.2	3000	1500	1.26	2402
Hydra	0.0521	0109980301	17 944.5	31 546.3	4000	2000	1.29	2180
Klemola 44	0.0286	0204460101	29 668.9	29 669.0	1200	500	1.28	2757
M87	0.0042	0114120101	35 931.1	39 551.8	15 000	3000	3.71	5401
MKW 3S	0.0417	0109930101	33 244.3	51 038.7	1900	800	1.24	2699
MKW 4	0.0214	0093060101	13 585.2	15 368.8	1000	200	1.26	673
Perseus	0.0148	0305780101	10 1982.0	12 4869.2	15 000	15 000	3.63	10 095

Table 4. continued.

Cluster	Redshift	ObsID	Filtered exposure (s)	Original exposure (s)	0.35–1.25 keV band scaling (cnts s^{-2} deg^{-2})	2.0–8.0 keV band scaling (cnts s^{-2} deg^{-2})	χ^2_ν	ν
Perseus a[10]	0.0147	0085110101	47 272.9	53 646.5	–	–	2.48	8982
PKS 0745-19	0.0986	0105870101	18 043.2	26 946.8	3000	5000	1.24	1872
RXCJ0605.8-3518	0.1367	201901001	17 798.1	26 668.6	3000	1500	1.30	904
RXJ0658-55	0.3069	0112980201	21 464.2	42 770.6	600	400	1.22	961
RXJ1347-1145	0.4477	0112960101	30 122.7	38 121.7	4000	3000	1.29	1290
Sérsic 159-3	0.0563	0147800101	81 339.4	122 209.4	3500	1000	1.51	3488
Sérsic 159-3 a[11]	0.0564	0123900101	30 643.1	60 996.9	–	–	1.14	1982
Triangulum	0.0478	0093620101	91 68.9	14 497.8	500	600	1.02	1890
ZW3146	0.2817	0108670101	51 450.6	53 597.1	4000	2000	1.36	1802

[8] Second observation.
[9] Dashes indicate that the cluster was not plotted.
[10] Second observation, under the name Abell 426 in the archive.
[11] Second observation, under the name AS 1101 in the archive.

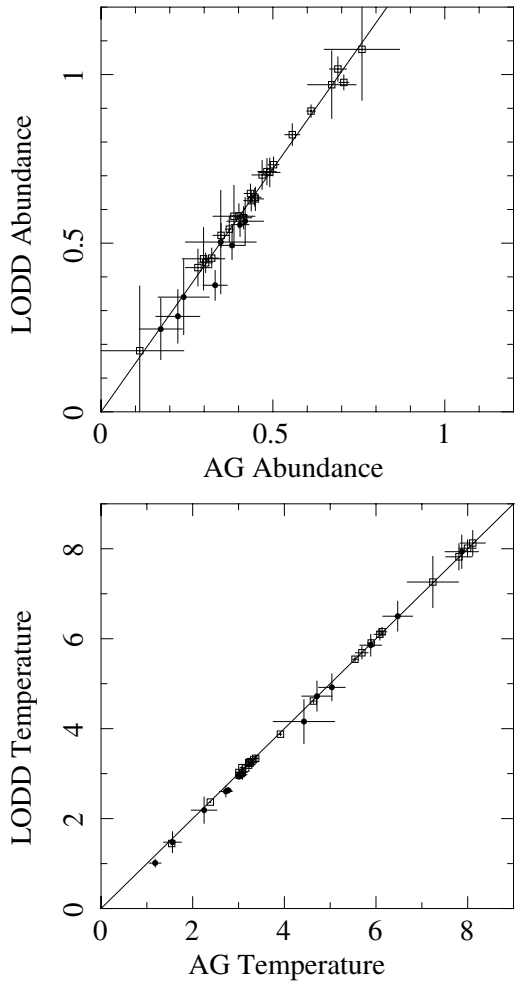

Fig. 16. The two plots display the comparison results from using Anders & Grevesse (1989) and Lodders (2003) abundances for the fitted values of the abundance (*upper panel*) and temperature (*lower panel*). In the upper plot the line is the best-fit scale factor of 1.44 while in the *lower plot* the line shows the one-to-one relationship. In both plots the filled circles indicate data from the outer annuli.

of 1.44 with the Lodders (2003) abundances greater than those of Anders & Grevesse (1989). The fitted temperatures using the two abundance models were all consistent.

We also have used the Abell 1795 data to examine the effect of allowing the abundances to vary independently using the VAPEC model of Xspec (Fig. 17). To examine the variation in the abundances we considered iron, which showed a simple scaling of 1.47, which is consistent with the factor of 1.44 determined for the average scale factor between the two abundance models. The fitted values for the temperatures were in very good agreement. For the Anders & Grevesse (1989) model the fitted Fe abundance when all elements were allowed to vary was ∼10% higher than the fitted average value for the abundance.

The temperature, abundance, and flux radial profiles for the 70 clusters listed in Table 4 are shown in Figs. 21 through 35 in the electronic version of this paper. The radii of the annuli have been scaled to the R_{500} value of the cluster as derived from the equation $R_{500} = 2.6\times((1.0+z)^{\frac{-3}{2}}\times(T/10.0)^{\frac{1}{2}}$ (Evrard et al. 1996) where z is the fitted value for the cluster redshift and T is the average fitted value for the cluster temperature in the $1'-4'$ annulus. Both the temperature and flux have been normalized to the values in the range 5%−30% of R_{500}.

We also include soft (0.35−1.25 keV) and hard (2.0−8.0 keV) band images of the clusters in the electronic version (Figs. 36 through 42). The images combine the MOS1 and MOS2 data and are background subtracted (QPB and SP), exposure corrected, and adaptively smoothed. Table 4 provides the upper scaling limits for the color coding (purple and blue indicate low intensity while red and white indicate high intensity). The images were produced by *ds9* where the minimum value of the dynamic range was set to zero and the image was logarithmically scaled. Units are counts s^{-1} deg^{-2} where the typical level of the cosmic background is ∼1 in these units. The intensities are average values of the MOS1 and MOS2 data rather than the sum. Table 5, also in the electronic version of this paper, lists the radial profile data, temperature, abundance, and flux, for the clusters.

6. Results and conclusions

In this paper we have outlined a robust and reliable method for analyzing extended X-ray sources observed with the *XMM-Newton* EPIC MOS detectors. The method combines screening of the data for periods of background enhancements (most notably the soft proton contamination), detailed modeling of the particle background spectrum, and the determination of other background components in the spectral fitting

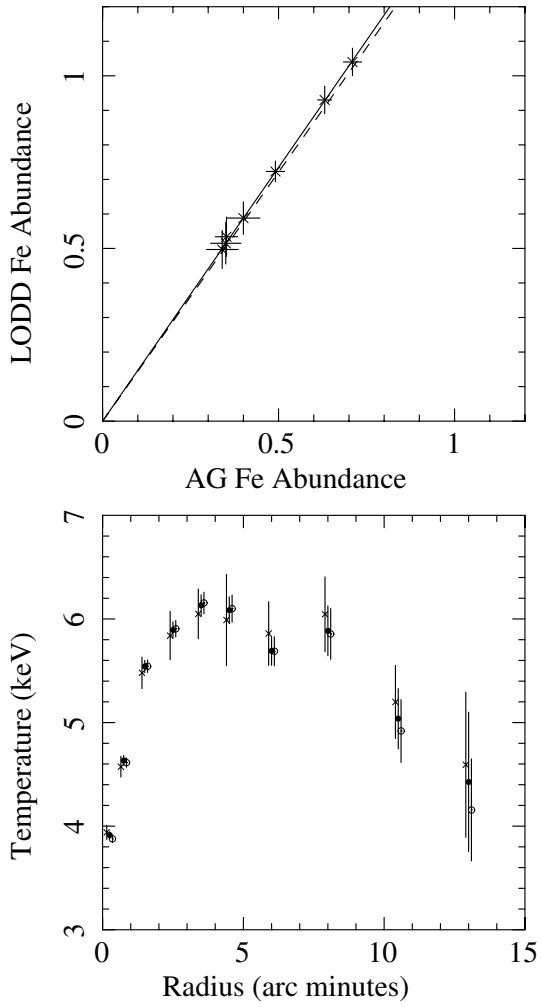

Fig. 17. Comparison of the fitted values for the annuli iron abundances and emission temperatures using Anders & Grevesse (1989) and Lodders (2003) model abundances while allowing all abundances to vary. The *upper panel* shows the correlation between the fitted values for the iron abundance for the two abundance models. The solid line is the best-fit correlation of 1.47 while the dashed line shows the 1.44 correlation of the single abundance normalization. The *lower panel* shows the fitted values for the temperatures where (open circle) abundances starting with Anders & Grevesse (1989) values were allowed to vary independently, (filled circle) Anders & Grevesse (1989) values were allowed to vary only with a single scale factor, and (filled triangle) Lodders (2003) values were allowed to vary only with a single scale factor.

process (residual SP contamination, fluorescent particle background lines, and the cosmic background).

We have demonstrated our method with the bulk processing of the observation of 70 clusters of galaxies. Comparison of the results for two separate observations of Abell 1835, Sérsic 159-3, and Perseus show good agreement between their fitted temperatures. However, comparison of our results with the *Chandra* results of Vikhlinin et al. (2005) for the overlapping subset of clusters shows a significant discrepancy for higher temperature clusters. The sense of this discrepancy is that the higher the fitted temperature, the greater the likelihood that *Chandra* will find a higher temperature than *XMM-Newton*. The differences can be over 1 keV at 7−8 keV. This effect can increase the apparent temperature gradient in the outer annuli of clusters in *Chandra* data.

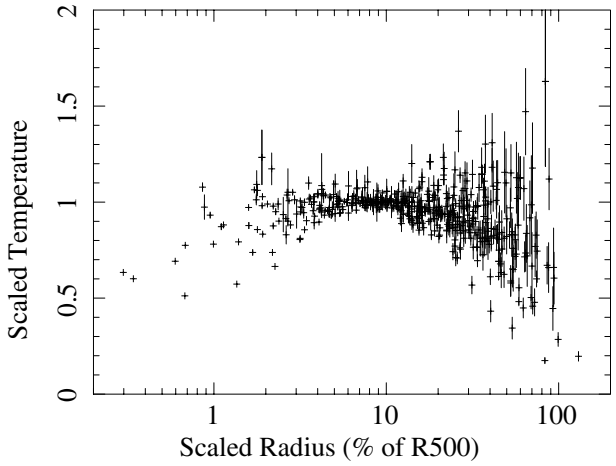

Fig. 18. Scaled temperature radial profiles for all of the analyzed clusters.

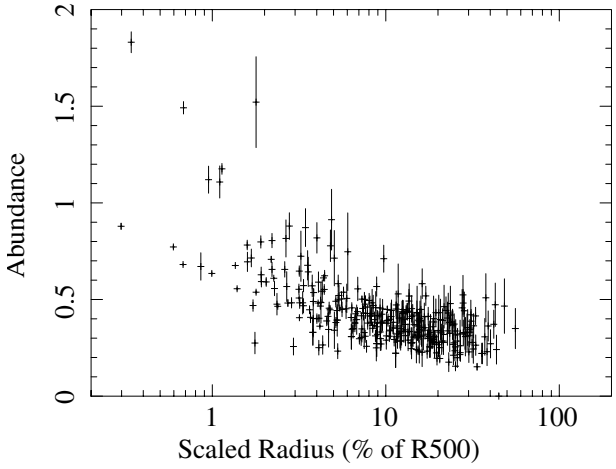

Fig. 19. Abundance radial profiles for all of the analyzed clusters.

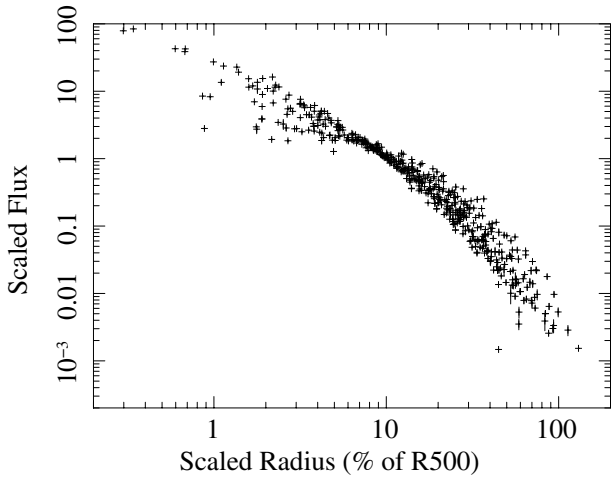

Fig. 20. Scaled flux radial profiles for all of the analyzed clusters.

While the detailed scientific analysis and discussion of these results are deferred to Paper II, a few aspects are clear from plots of the entire data set. For the combined plots, the radii of the annuli have been scaled to the R_{500} value in the same manner as the individual plots (Sect. 5). Figures 18−20 show the cumulative plots for the temperature, abundance, and flux, respectively. Again, both the temperature and flux have also been normalized

to the values in the range 5%−30% of R_{500}. In addition, only points where the fitted values are three times the fitted uncertainty are plotted.

Inspection of Fig. 18 shows, as seen before (e.g. Pratt et al. 2007; Arnaud et al. 2005; Vikhlinin et al. 2006), a wide variety of temperature profiles inside 5% of R(500). Most of these can be characterized by a temperature drop in the center as has long been seen in cooling-flow clusters. However our single phase analysis may produce results slightly different than more detailed analysis. Over the range from $0.05-0.2R_{500}$ the clusters are isothermal to better than 5%. Beyond $\sim 0.2R_{500}$ a significant fraction of the clusters (Paper II) show temperature drops, but they are not all self-similar. However a significant fraction of the clusters are relatively isothermal out to the largest radii measurable.

As noted by Arnaud et al. (2005), many of the clusters show a self-similar surface brightness profile (Fig. 20). Inside of $\sim 0.03R_{500}$ there is significant scatter in the profile. With respect to the overall abundance, as was noted for *ASCA* spectra of clusters by Finoguenov et al. (2001) and later for many *XMM-Newton* and *Chandra* spectra (Maugham et al. 2007) there is, in a significant fraction of the clusters, an abundance increase in the center. However outside of the central $\sim 0.05R_{500}$ there is little evidence for an abundance gradient and all the clusters are very close to the average value of $A = 0.3$ on the Anders & Grevesse (1989) abundance scale (Fig. 19). Detailed analysis of these results will appear in Paper II.

Acknowledgements. We would like to thank Alexey Vihklinin for providing the *Chandra* cluster profiles and Richard Saxton for providing the arfgen modification for calculating the "cross-talk" between annuli. We would also like to thank the *XMM-Newton* Background Working Group for their comments and encouragement. The data for this work were provided through the HEASARC. This work was made possible by NASA *XMM-Newton* Guest Observer grants and the support of the NASA *XMM-Newton* Guest Observer Facility at the Goddard Space Flight Center.

References

Allen, S. W., Schmidt, R. W., & Fabian, A. C. 2001, MNRAS, 328, L37
Anders, E., & Grovers, N. 1989, Geochim. Cosmochim. Acta, 53, 197
Arnaud, M., Neumann, D. M., Aghanim, N., et al. 2001, A&A, 365, L80
Arnaud, M., Majerowisc, S., Lumb, D., et al. 2002, A&A, 390, 27
Arnaud, M., Pointecouteau, E., & Pratt, G. W. 2005, A&A, 441, 893
Bahcall, N. A. 1997, ARA&A, 15, 1505
de Grandi, S., & Molendi, S. 2001, ApJ, 567, 163
de Grandi, S., Böhringer, H., Guzzo, L., et al. 1999, ApJ, 514, 148
De Luca, A., & Molendi, S. 2004, A&A, 419, 837
de Plaa, J., Werner, N., Bykov, A. M., et al. 2006, A&A, 452, 397
Donahue, M., Horner, D. J., Cavagnolo, K. W., & Voit, G. M. 2006, ApJ, 643, 730
Ehle, M., et al. 2005, XMM-Newton Users' Handbook (Madrid: ESA)
Evrard, S. 2003, Carnegie Observatories Astrophysics Series, Vol. 3, Clusters of Galaxies: Probes of Cosmological Structure and Galaxy Evolution, ed. J. S. Mulchaey, A. Dressler, & A. Oemler (Cambridge: Cambridge Univ. Press)
Evrard, A. E., Metzler, C. A., & Navarro, J. F. 1996, ApJ, 469, 494
Fabricant, D., & Gorenstein, P. 1983, ApJ, 267, 535
Fabricant, D., Lecar, M., & Gorenstein, P. 1980, ApJ, 241, 552
Finoguenov, A., Arnaud, M., & David, L. P. 2001, ApJ, 555, 191
Gorenstein, P., Bjorkholm, P., Harris, B., & Harnden, F. R., Jr. 1973, ApJ, 183, 57
Hashimoto, Y., Barcons, X., Böhringer, H., et al. 2004, A&A, 417, 819
Hickox, R. C., & Markevitch, M. 2007, ApJ, 661, L117
Hughes, J. P., Gorenstein, P., & Fabricant, D. 1988, ApJ, 329, 82
Irwin, J. A., Bregman, J. N., & Evrard, A. E. 1999, ApJ, 519, 518
Irwin, J. A., & Bregman, J. N. 2000, ApJ, 538, 543
Jones, C., & Forman, W. 1978, ApJ, 224, 1
Jones, C., & Forman, W. 1984, ApJ, 276, 38
Joye, W. A., & Mandel, E. 2003, in Astronomical Data Analysis Software and Systems XII, ed. H. E. Payne, R. I. Jedrzejewski, & R. N. Hook, ASP Conf. Ser., 295, 489
Kaastra, J. S., Tamura, T., Peterson, J. R., et al. 2004, A&A, 413, 415
Kay, S. T., Thomas, P. A., Jenkins, A., & Pearce, F. R. 2004, MNRAS, 355, 1091
Kikuchi, K., Furusho, T., Ezawa, H., et al. 1999, PASJ, 51, 301
Komatsu, & Seljak 2001, MNRAS, 327, 1353
Kuntz, K., & Snowden, S. L. 2000, ApJ, 543, 195
Kuntz, K. D., & Snowden, S. L. 2001, ApJ, 554, 684
Kuntz, K. D., & Snowden, S. L. 2008, A&A, 478, 575 (KS07)
Kuntz, K. D., Snowden, S. L., & Mushotzky, R. F. 2001, ApJ, 548, 11
Lallement, R. 2004, A&A, 418, 143
Lodders, K. 2003, ApJ, 591, 1220
Loken, C., Norman, M. L., Nelson, E., et al. 2002, ApJ, 579, 571
Majerowicz, S., Neumann, D. M., & Reiprich, T. H. 2002, A&A, 394, 77
Markevitch, M., Forman, W. R., Sarazin, C. L., & Vikhlinin, A. 1998, ApJ, 503, 77
Maughan, B. J., Jones, C., Forman, W., & Van Speybroeck, L. 2007, in press
McCammon, D., Almy, R., Apodaca, E., et al. 2002, ApJ, 576, 188
Morrison, R., & McCammon, D. 1983, ApJ, 270, 119
Mushotzky, R. F., Serlemitsos, P. J., Boldt, E. A., Holt, S. S., & Smith, B. W. 1978, 1978, ApJ, 225, 21
Mushotzky, R. 2002, in The Century of Space Science (Kluwer: The Netherlands), 473
Navarro, J. F., Frenk, C. S., & White, S. D. M. 1997, ApJ, 490, 493
Nevalainen, J., Markevitch, M., & Lumb, D. 2005, ApJ, 629, 172
Piffaretti, R., Jetzer, Ph., Kaastra, J. S., & Tamura, T. 2005, A&A, 433, 101
Pratt, G. W., & Arnaud, M. 2002, A&A, 394, 375
Pratt, G. W., Bhringer, H., Croston, J. H., et al. 2007, A&A,461, 71
Rasia, E., Ettori, S., Moscardini, L., et al. 2006, MNRAS, 369, 2013
Read, A., & Ponman, T. 2003, A&A, 409, 395
Robertson, I. P., & Cravens, T. E. 2003, Geophys. Res. Lett., 30, 1439
Sfeir, D. M., Lallement, R., Crifo, F., & Welsh, B. Y. 1999, A&A, 346, 785
Snowden, S. L., Collier, M. R., & Kuntz, K. D. 2004, ApJ, 610, 1182
Snowden, S. L., Egger, R., Freyberg, M. J., et al. 1997, ApJ, 485, 125
Snowden, S. L., Egger, R., Finkbeiner, D. P., Freyberg, M. J., & Plucinsky, P. P. 1998, ApJ, 493, 715
Tozzi, P., Gilli, R., Mainieri, V., et al. 2006, A&A, 451, 457
Vikhlinin, A., Markevitch, M., Murray, S. S., et al. 2005, ApJ, 628, 655
Vikhlinin, A., Kravtsov, A., Forman, W., et al. 2006 ApJ, 640, 691
Wargelin, B. J., Markevitch, M., Juda, M., et al. 2004, ApJ, 607, 596
White, D. A. 2000, MNRAS, 312, 663
White, D. A., & Buote, D. A. 2000, MNRAS, 312, 649

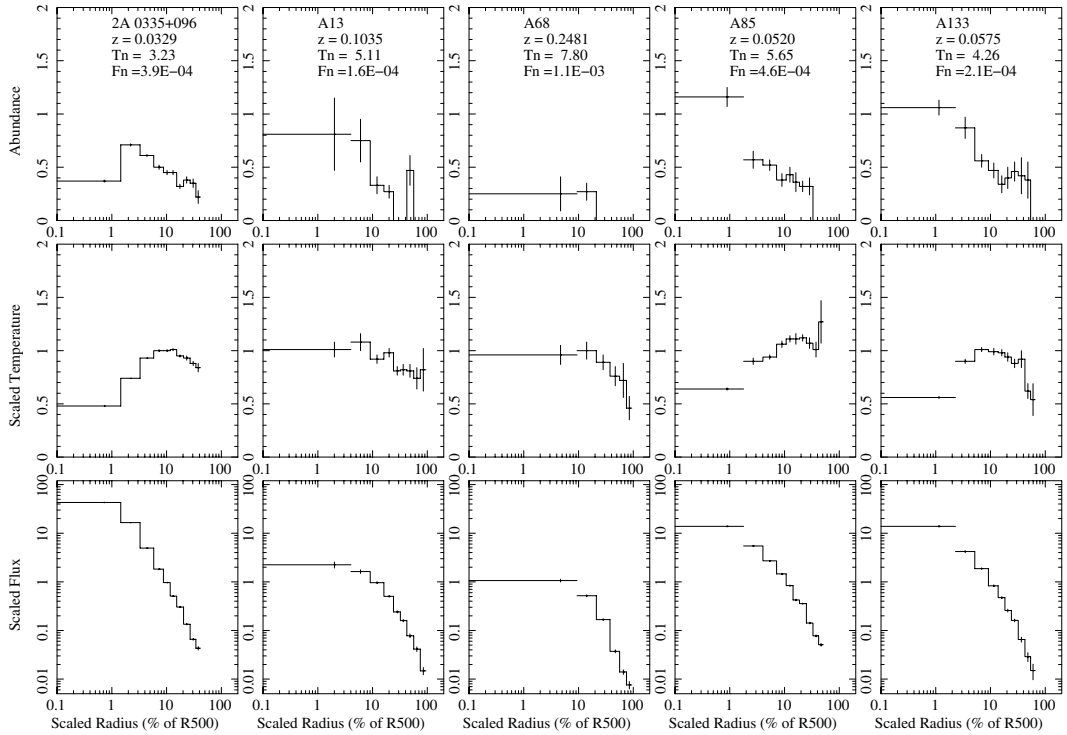

Fig. 21. Cluster temperature, abundance, and flux radial profiles. The name of the cluster, fitted redshift, and values for the temperature (T_N) and flux (T_N) used for the normalization of the data are provided in the abundance panel.

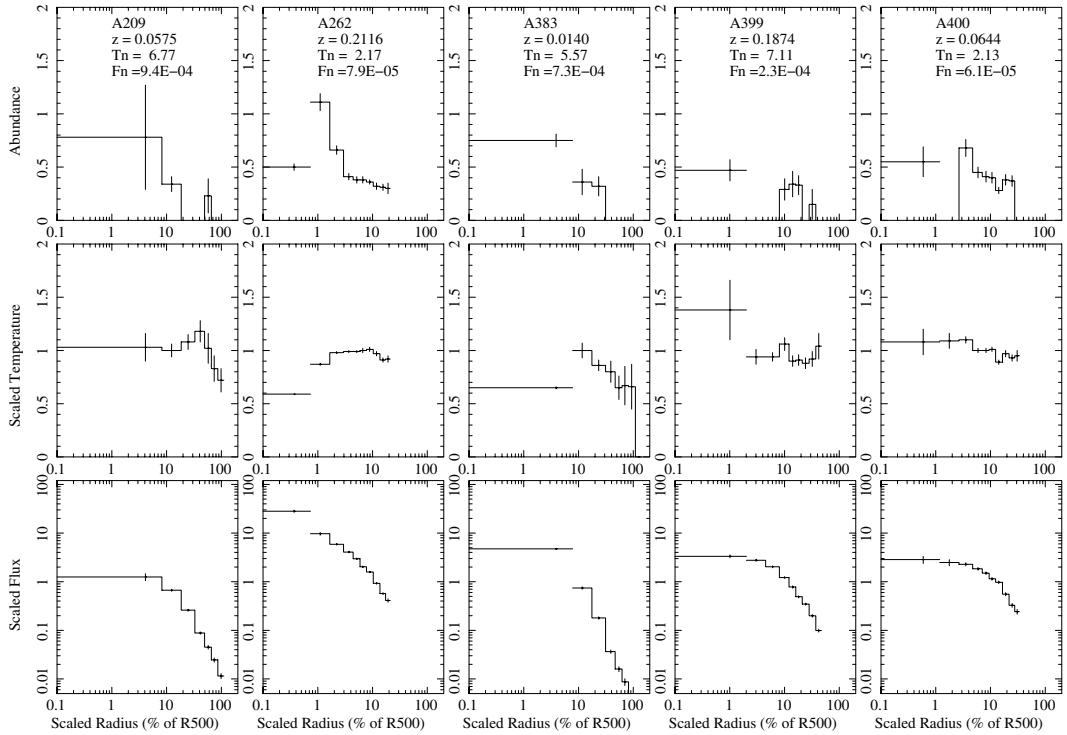

Fig. 22. Cluster temperature, abundance, and flux radial profiles. The name of the cluster, fitted redshift, and values for the temperature (T_N) and flux (T_N) used for the normalization of the data are provided in the abundance panel.

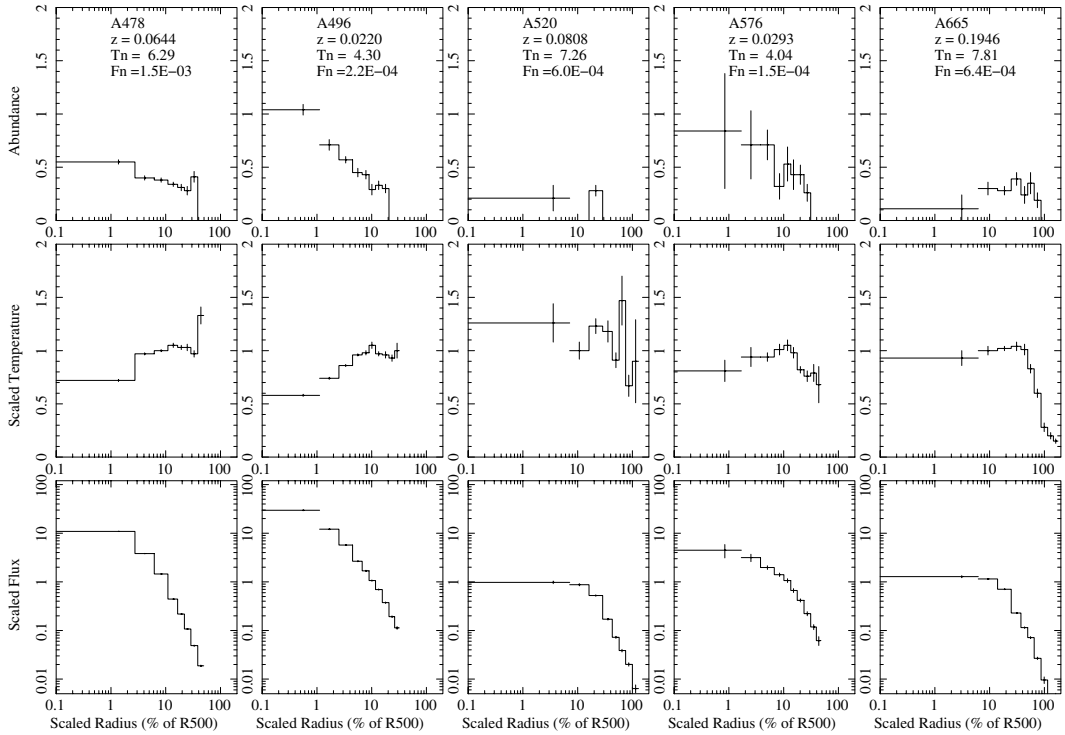

Fig. 23. Cluster temperature, abundance, and flux radial profiles. The name of the cluster, fitted redshift, and values for the temperature (T_N) and flux (T_N) used for the normalization of the data are provided in the abundance panel.

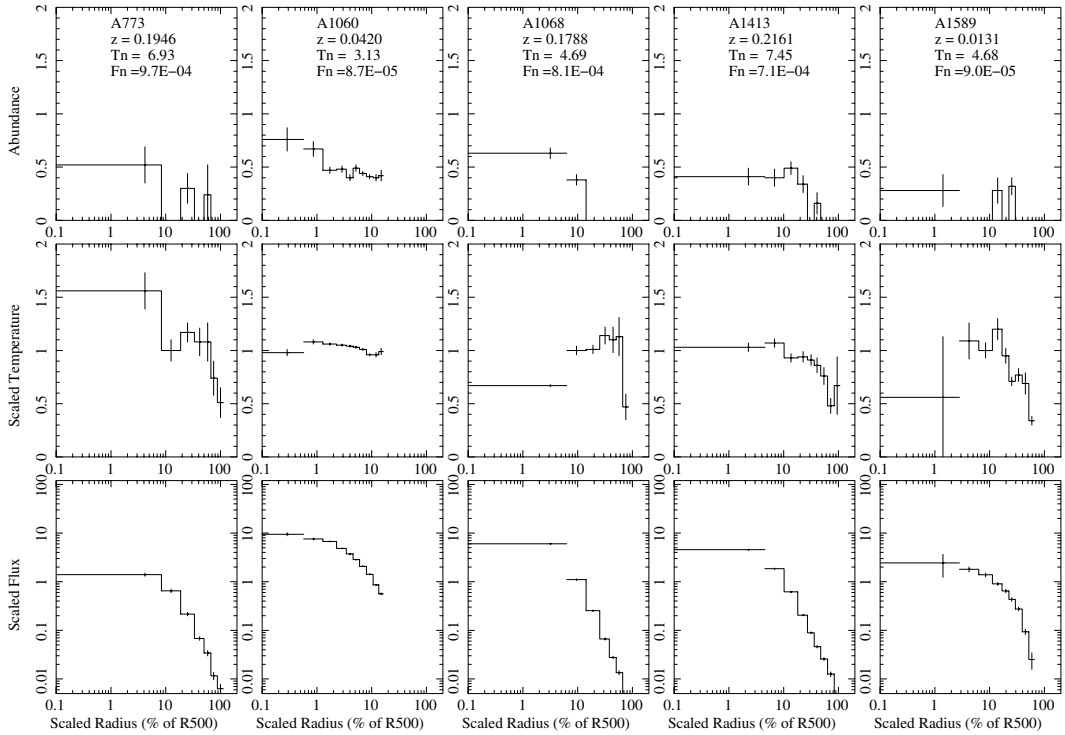

Fig. 24. Cluster temperature, abundance, and flux radial profiles. The name of the cluster, fitted redshift, and values for the temperature (T_N) and flux (T_N) used for the normalization of the data are provided in the abundance panel.

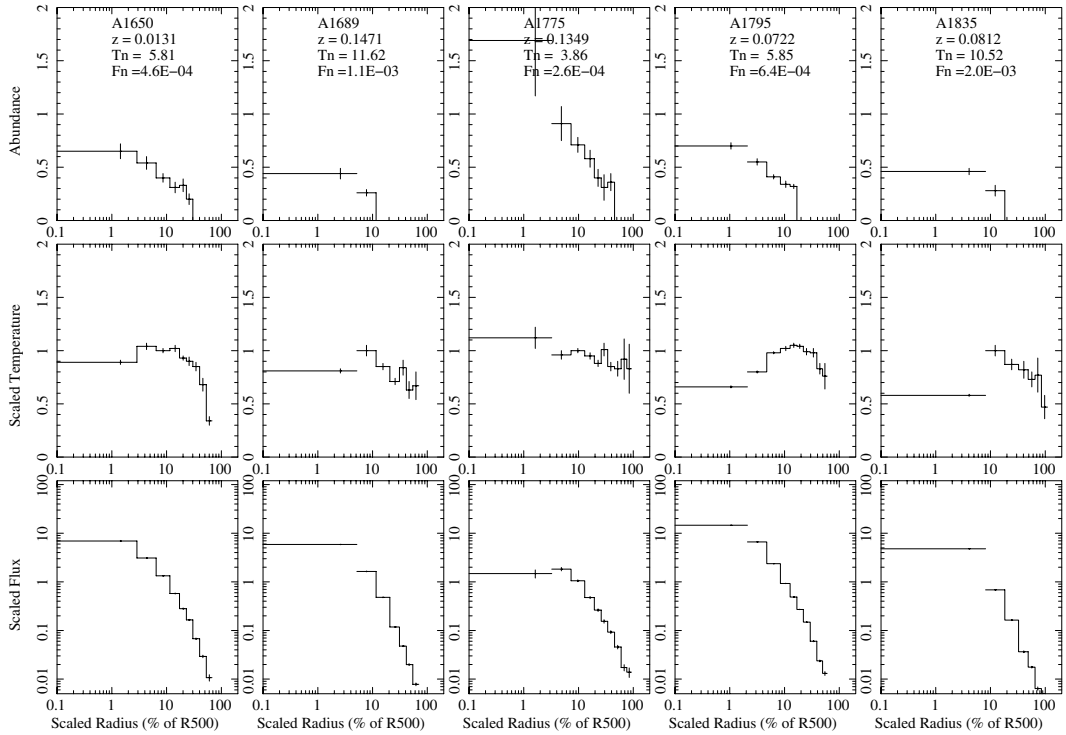

Fig. 25. Cluster temperature, abundance, and flux radial profiles. The name of the cluster, fitted redshift, and values for the temperature (T_N) and flux (T_N) used for the normalization of the data are provided in the abundance panel.

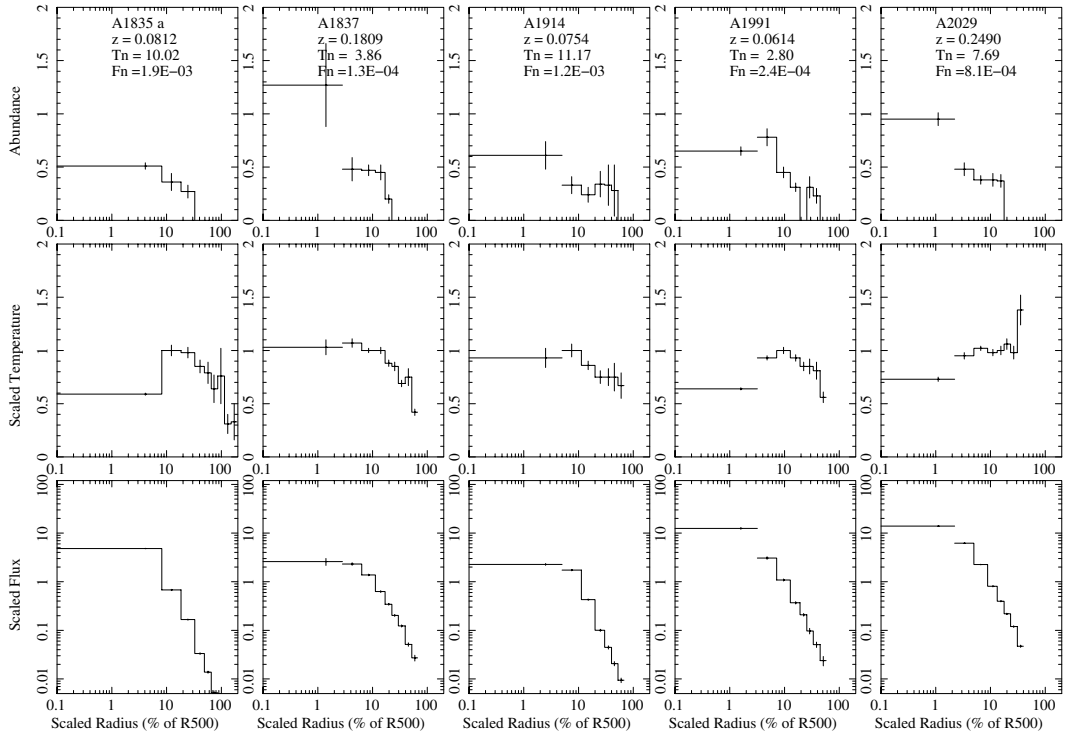

Fig. 26. Cluster temperature, abundance, and flux radial profiles. The name of the cluster, fitted redshift, and values for the temperature (T_N) and flux (T_N) used for the normalization of the data are provided in the abundance panel.

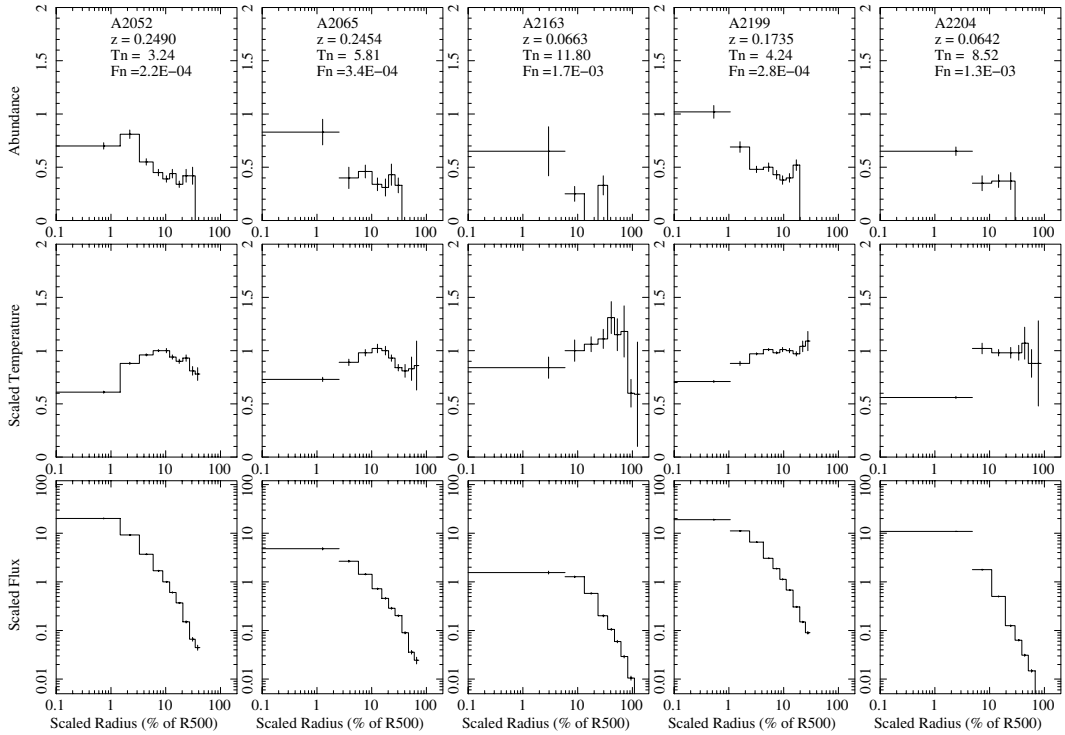

Fig. 27. Cluster temperature, abundance, and flux radial profiles. The name of the cluster, fitted redshift, and values for the temperature (T_N) and flux (T_N) used for the normalization of the data are provided in the abundance panel.

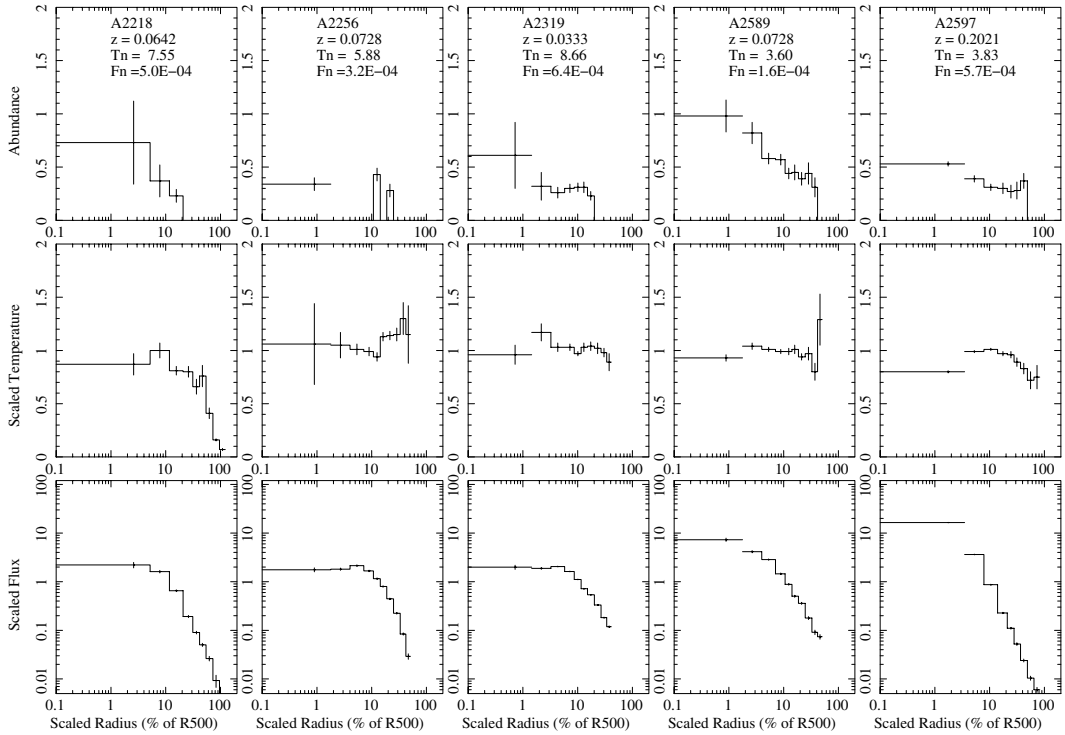

Fig. 28. Cluster temperature, abundance, and flux radial profiles. The name of the cluster, fitted redshift, and values for the temperature (T_N) and flux (T_N) used for the normalization of the data are provided in the abundance panel.

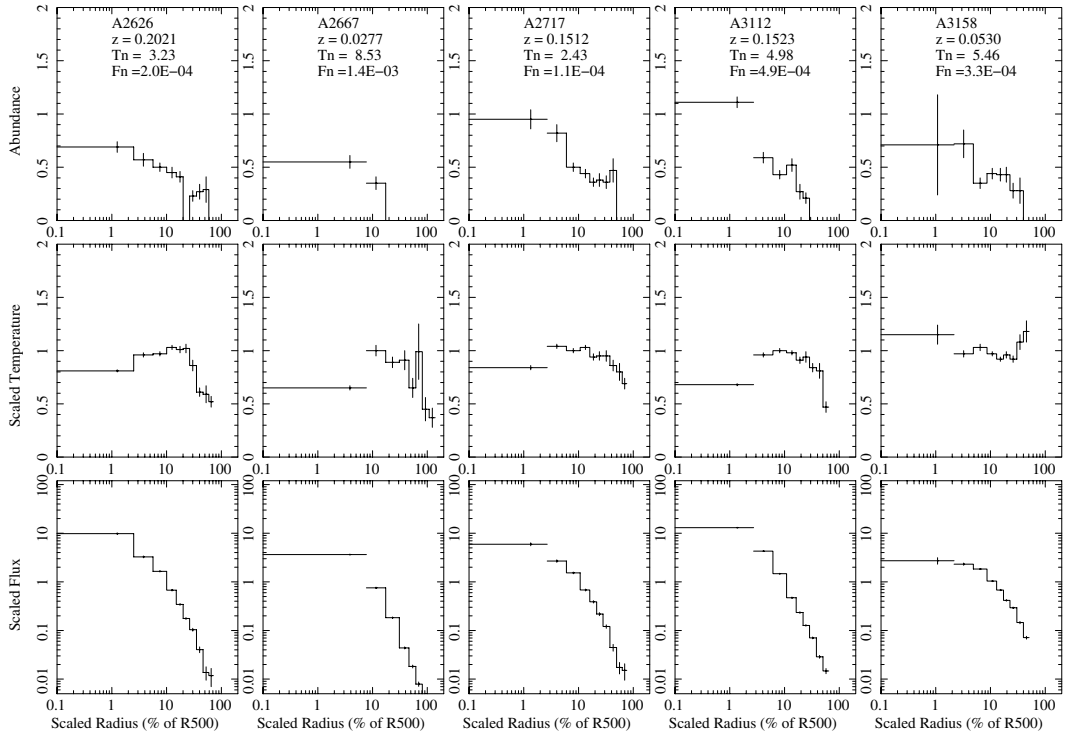

Fig. 29. Cluster temperature, abundance, and flux radial profiles. The name of the cluster, fitted redshift, and values for the temperature (T_N) and flux (T_N) used for the normalization of the data are provided in the abundance panel.

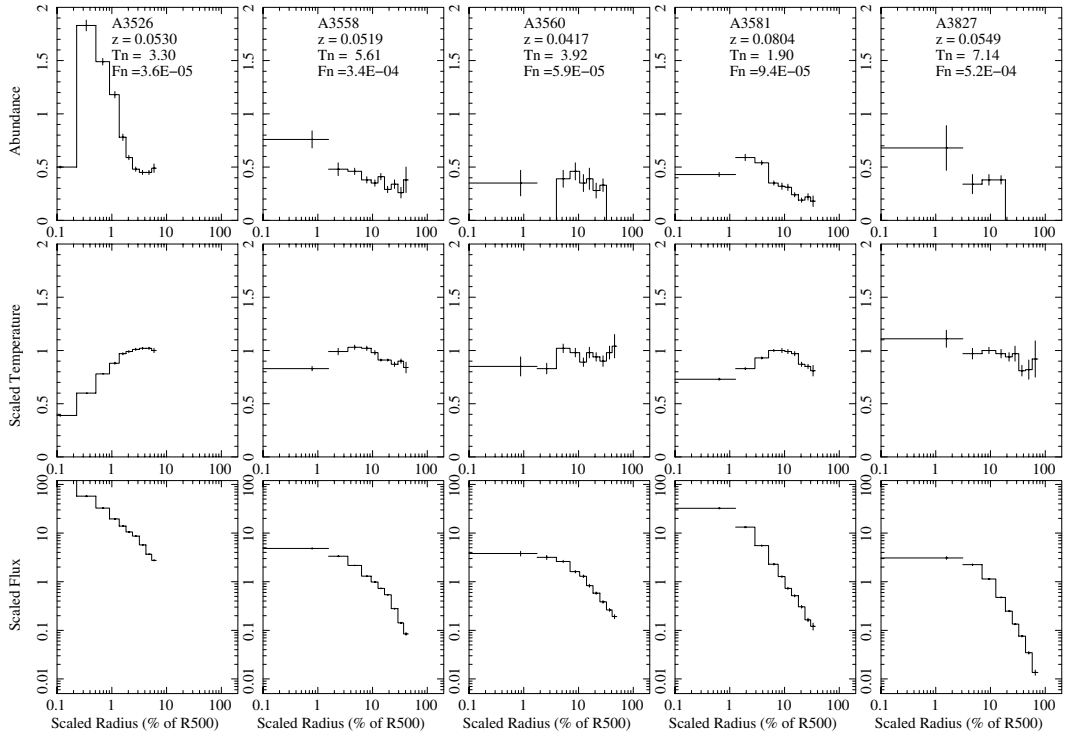

Fig. 30. Cluster temperature, abundance, and flux radial profiles. The name of the cluster, fitted redshift, and values for the temperature (T_N) and flux (T_N) used for the normalization of the data are provided in the abundance panel.

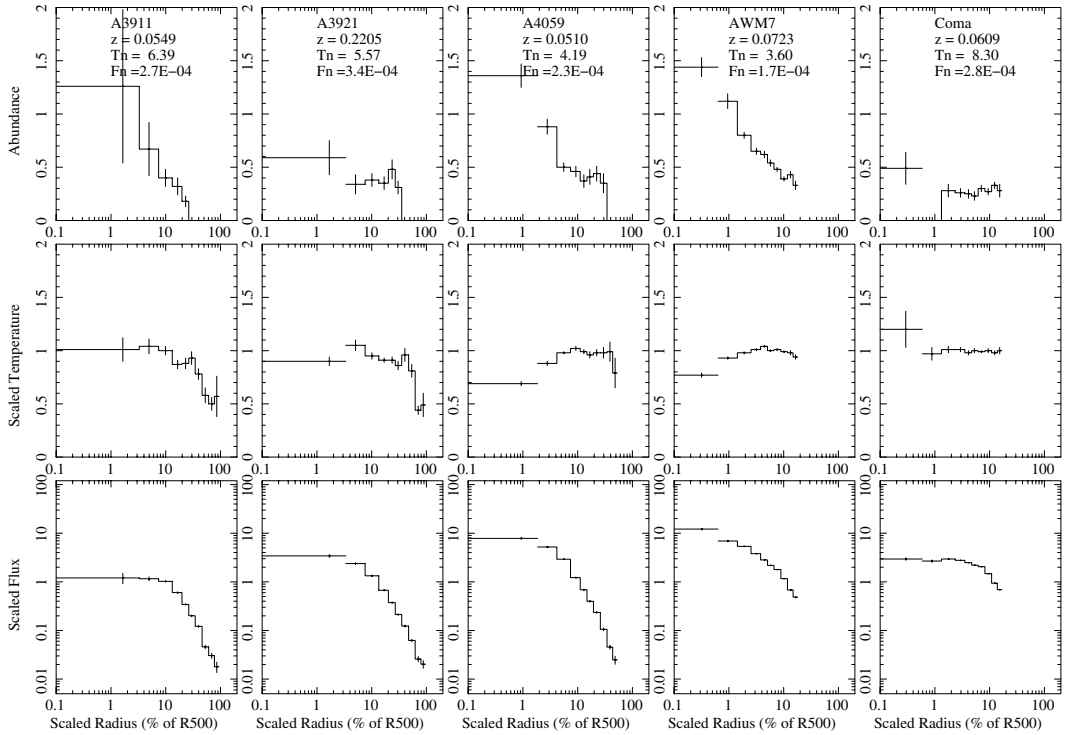

Fig. 31. Cluster temperature, abundance, and flux radial profiles. The name of the cluster, fitted redshift, and values for the temperature (T_N) and flux (T_N) used for the normalization of the data are provided in the abundance panel.

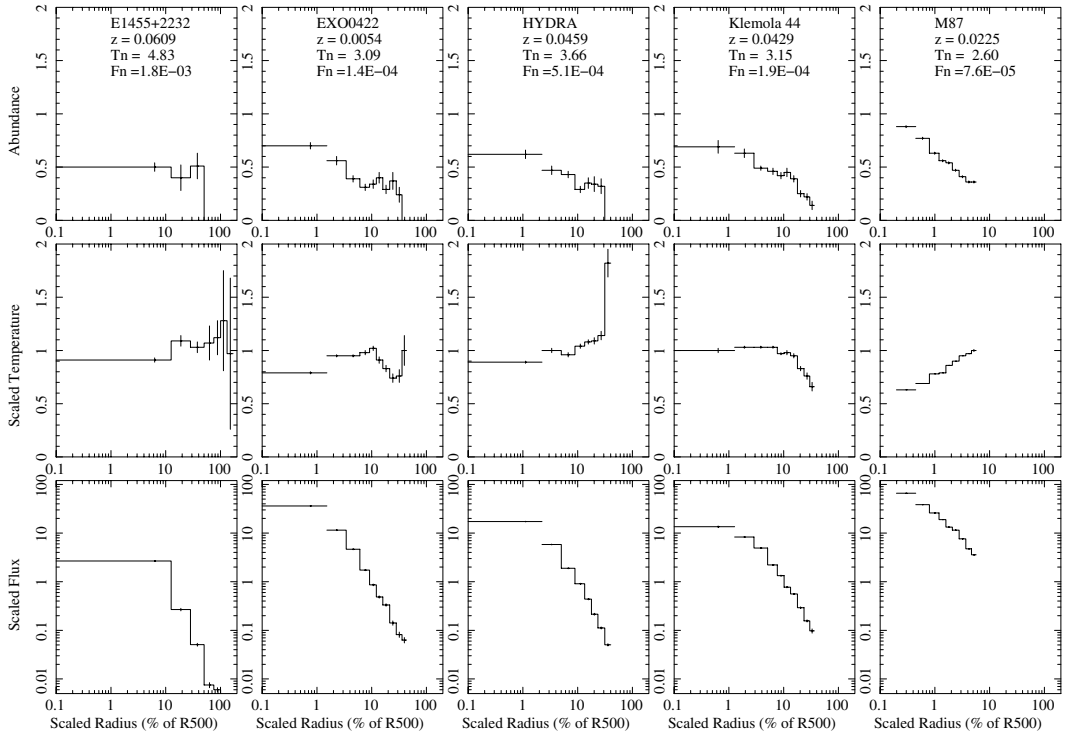

Fig. 32. Cluster temperature, abundance, and flux radial profiles. The name of the cluster, fitted redshift, and values for the temperature (T_N) and flux (T_N) used for the normalization of the data are provided in the abundance panel.

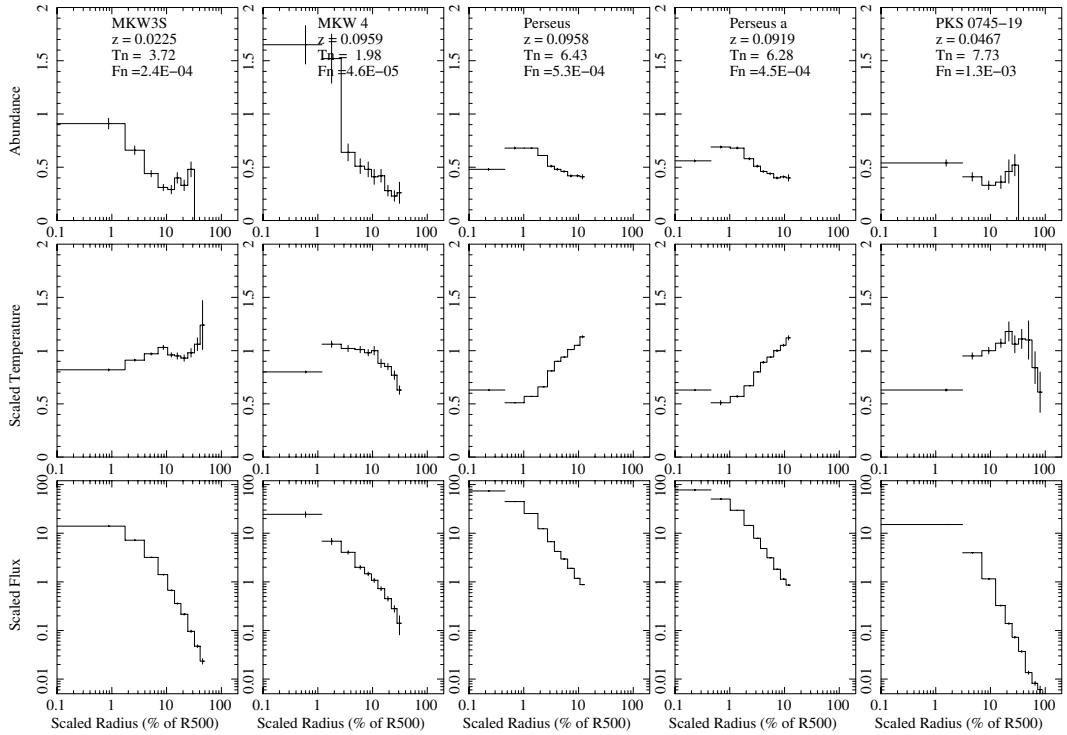

Fig. 33. Cluster temperature, abundance, and flux radial profiles. The name of the cluster, fitted redshift, and values for the temperature (T_N) and flux (T_N) used for the normalization of the data are provided in the abundance panel.

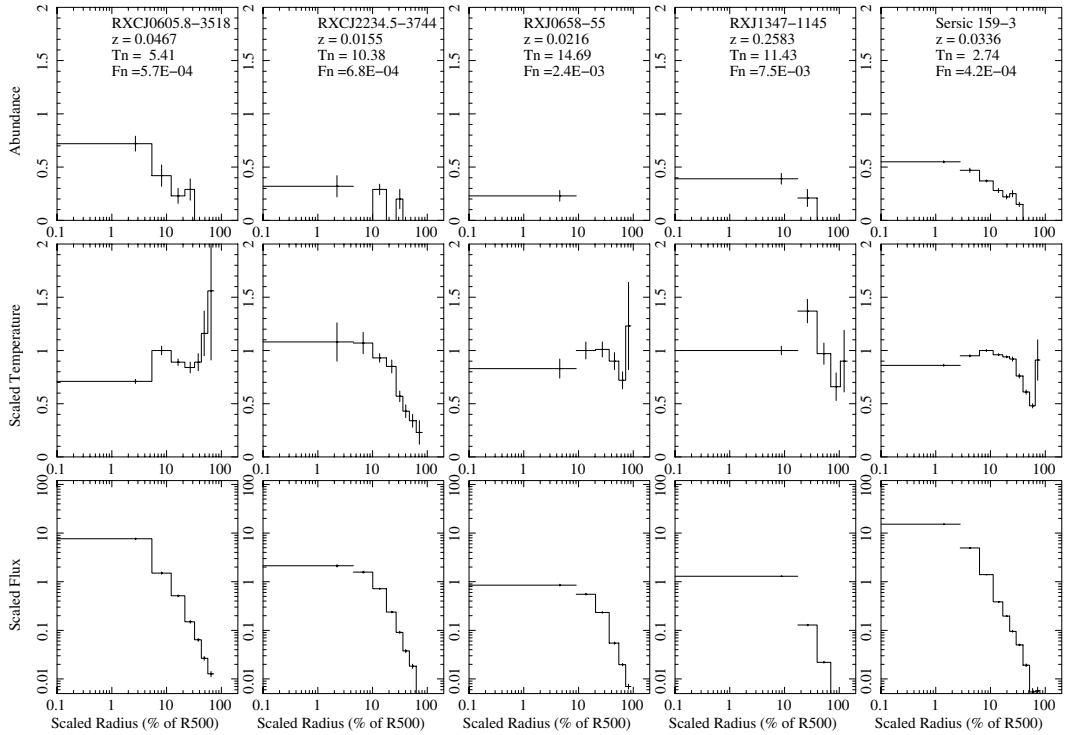

Fig. 34. Cluster temperature, abundance, and flux radial profiles. The name of the cluster, fitted redshift, and values for the temperature (T_N) and flux (T_N) used for the normalization of the data are provided in the abundance panel.

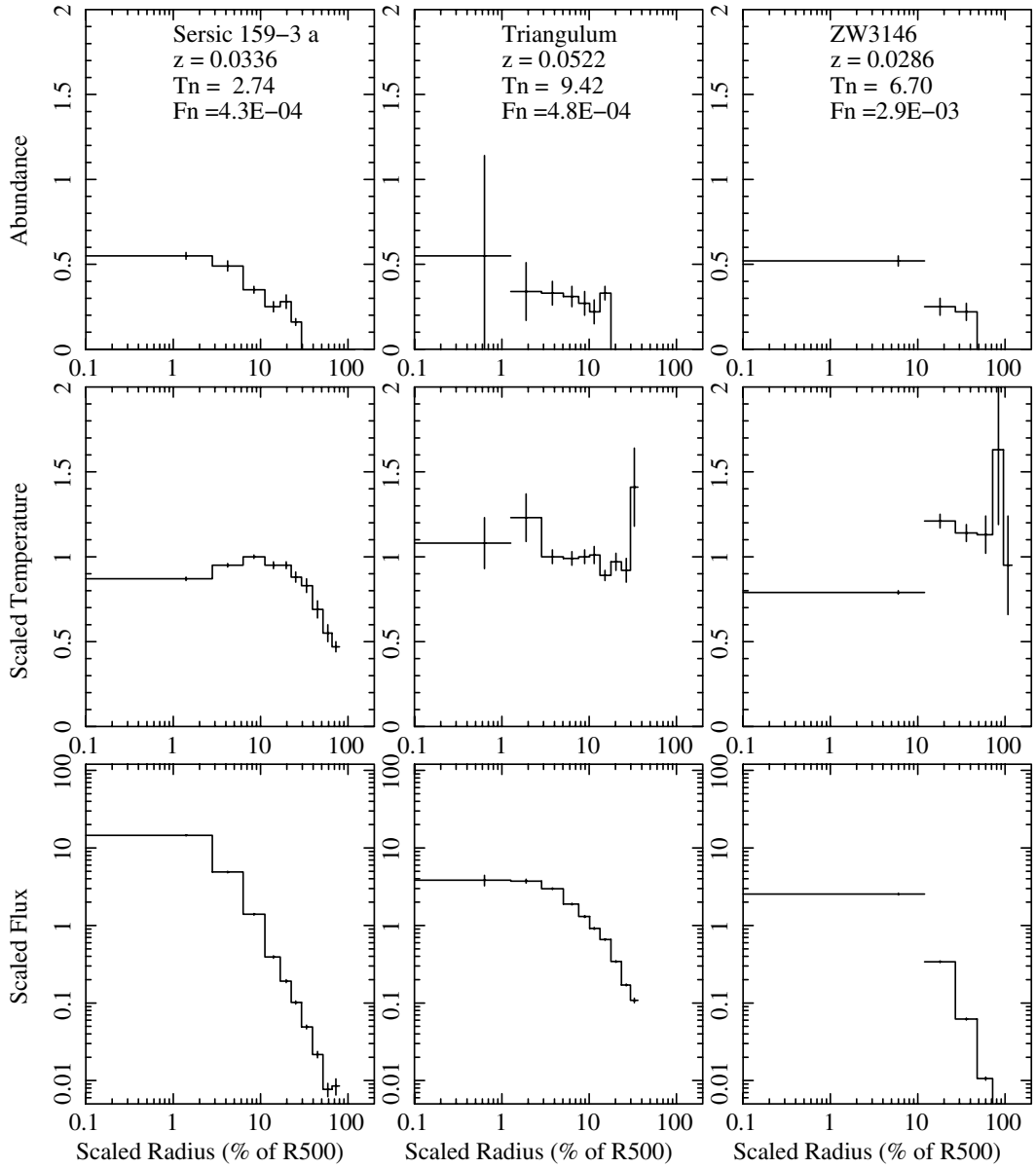

Fig. 35. Cluster temperature, abundance, and flux radial profiles. The name of the cluster, fitted redshift, and values for the temperature (T_N) and flux (T_N) used for the normalization of the data are provided in the abundance panel.

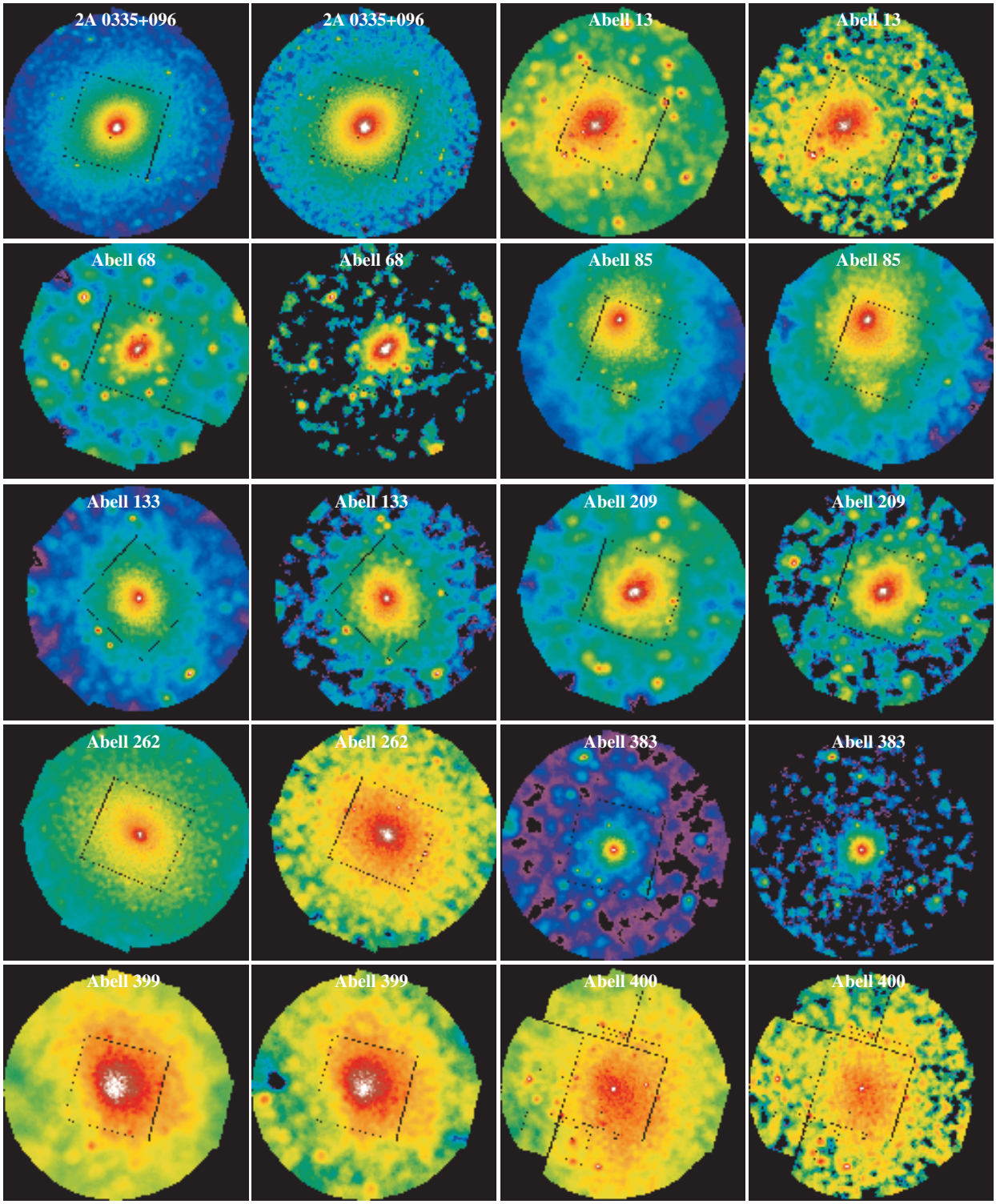

Fig. 36. Soft (*left*) and hard (*right*) band images of the clusters.

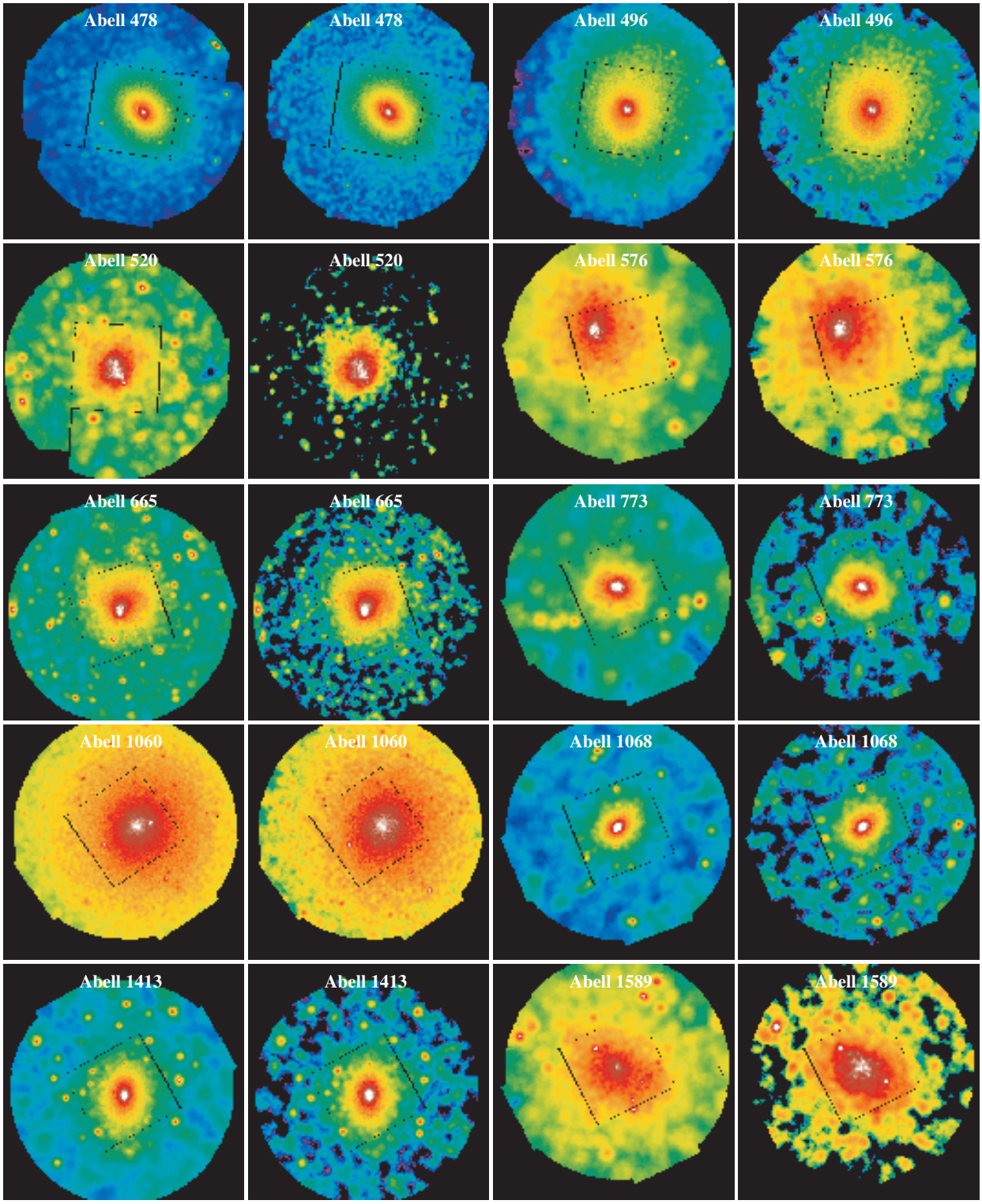

Fig. 37. Soft (*left*) and hard (*right*) band images of the clusters.

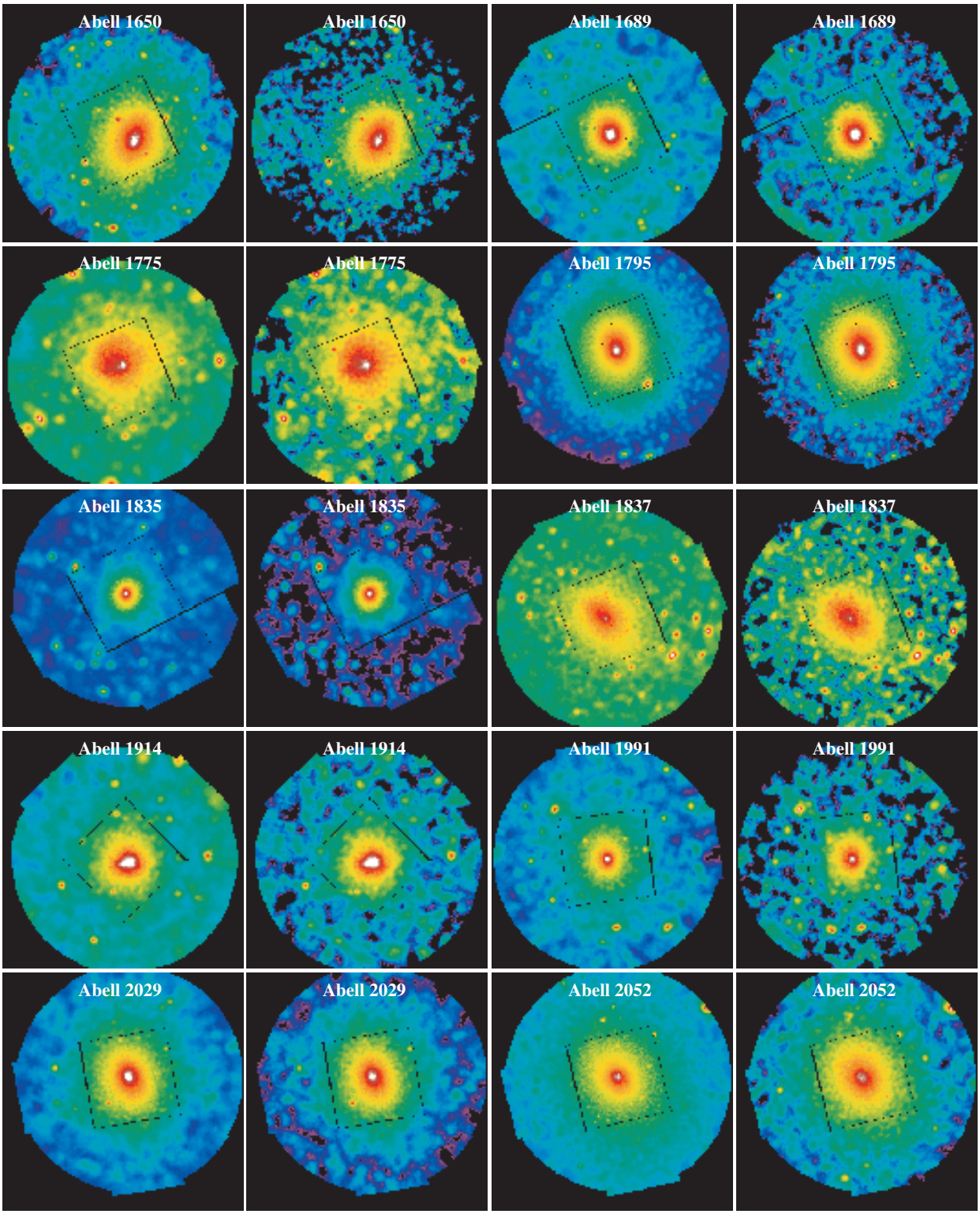

Fig. 38. Soft (*left*) and hard (*right*) band images of the clusters.

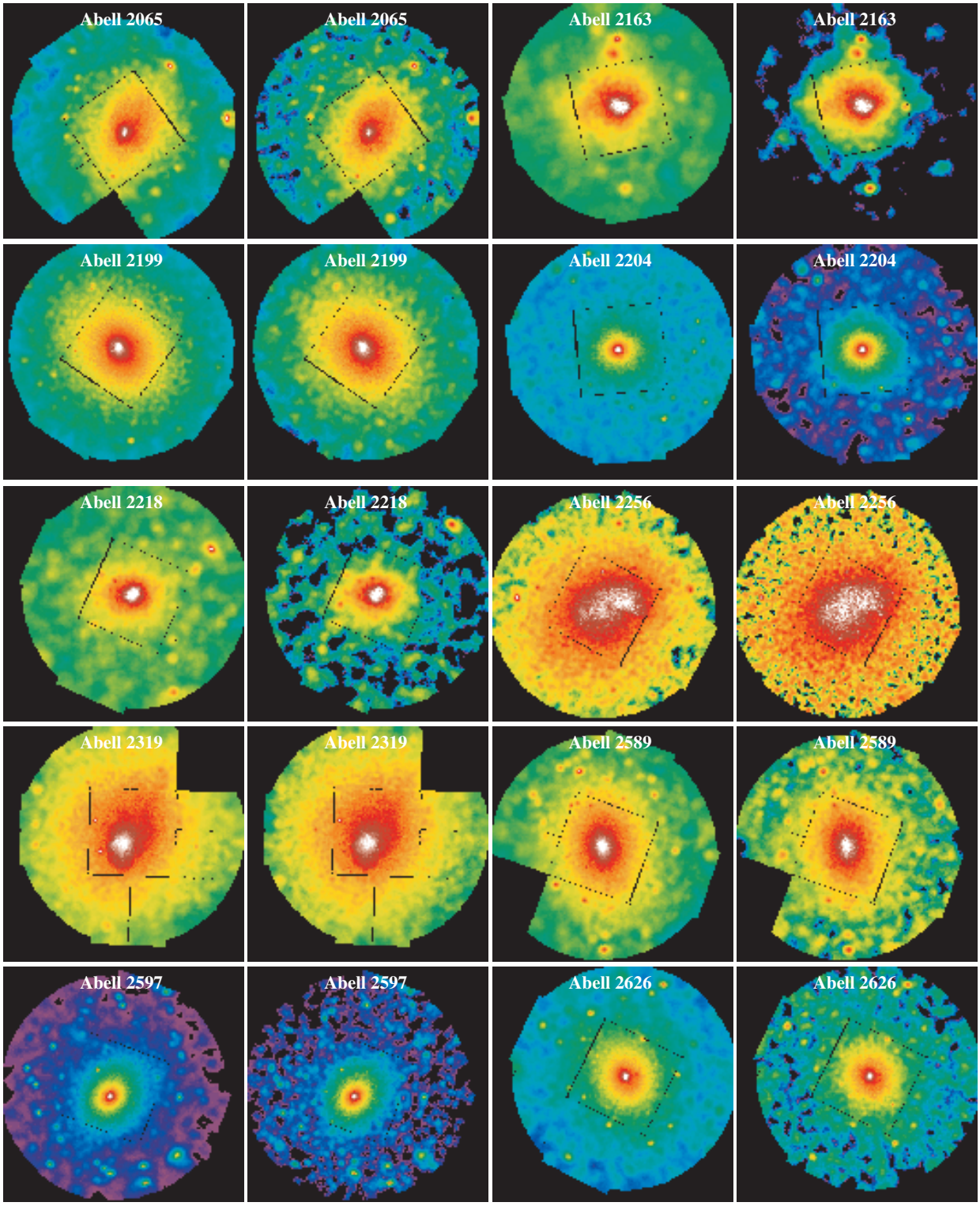

Fig. 39. Soft (*left*) and hard (*right*) band images of the clusters.

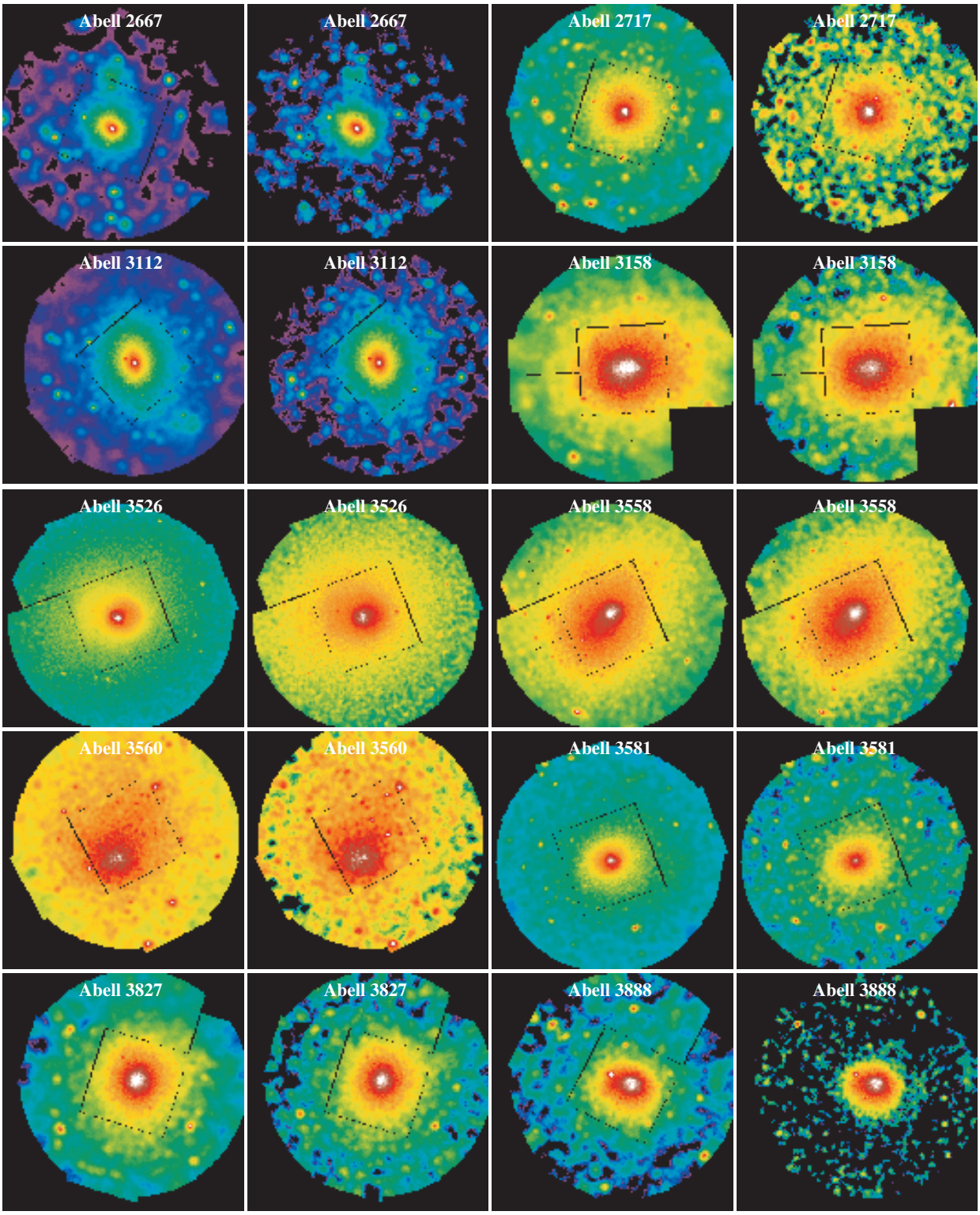

Fig. 40. Soft (*left*) and hard (*right*) band images of the clusters.

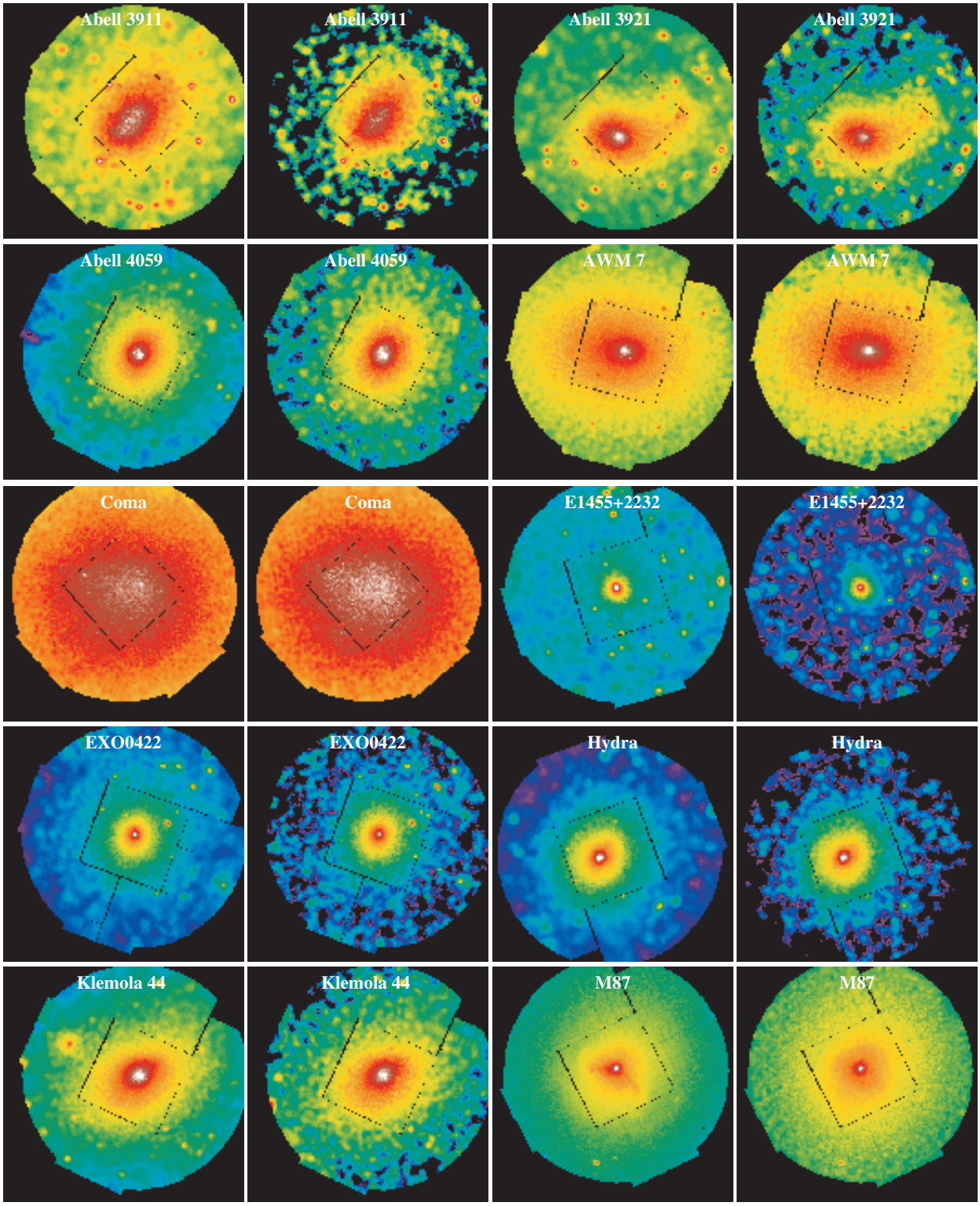

Fig. 41. Soft (*left*) and hard (*right*) band images of the clusters.

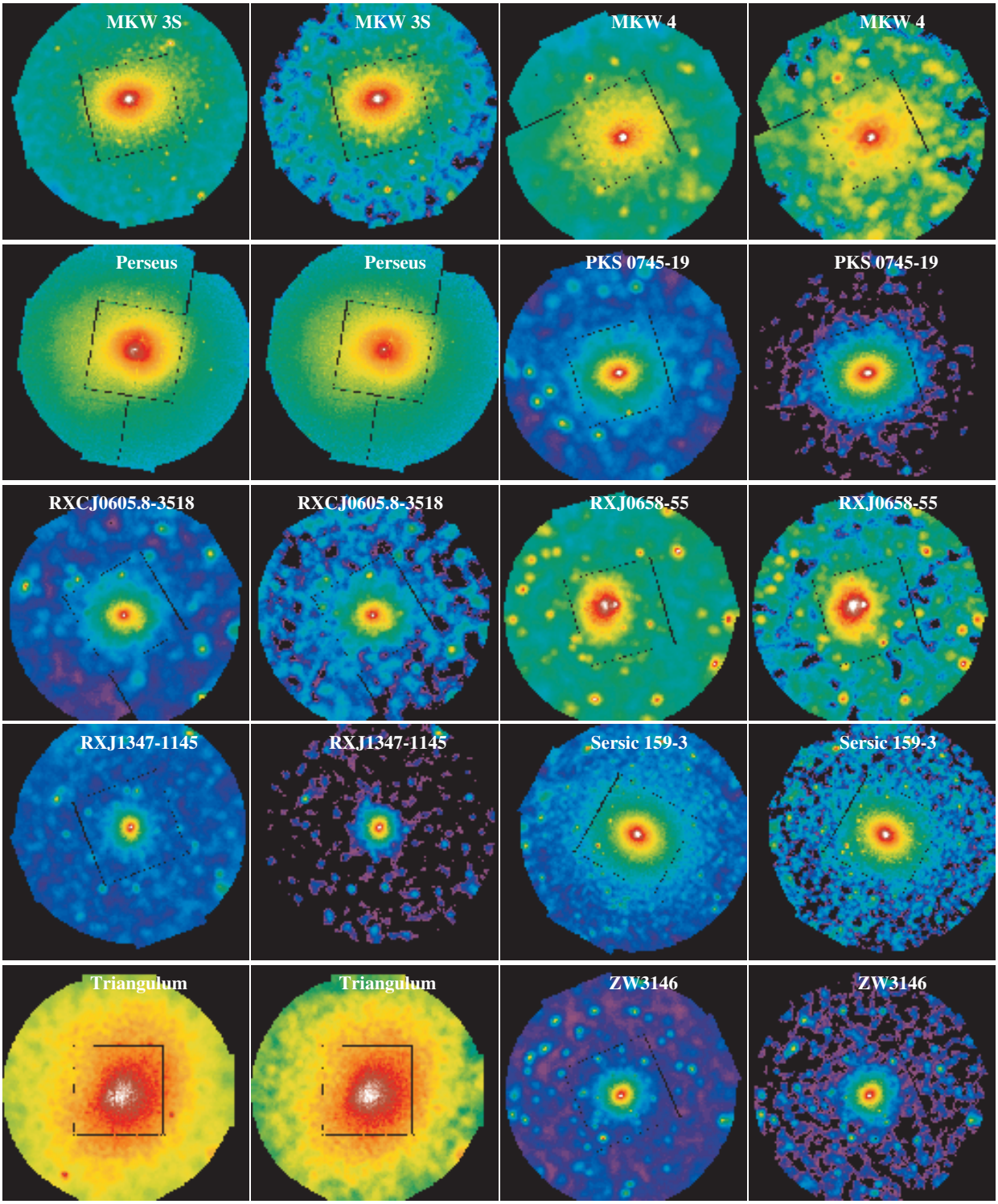

Fig. 42. Soft (*left*) and hard (*right*) band images of the clusters.

Table 5. Cluster details.

Cluster	Annulus	T (keV)	σ_T (keV)	A	σ_A	F (0.3–10.0 keV) erg cm^{-2} s^{-1} arcmin^{-2}	σ_F (0.3–10.0 keV) erg cm^{-2} s^{-1} arcmin^{-2}
2A 0335+096	1	1.542	0.008	0.371	0.011	1.876E-11	0.034E-11
–	2	2.383	0.011	0.708	0.015	8.398E-12	0.079E-12
–	3	3.011	0.014	0.612	0.013	2.607E-12	0.024E-12
–	4	3.225	0.020	0.502	0.016	9.532E-13	0.121E-13
–	5	3.233	0.025	0.449	0.018	4.965E-13	0.076E-13
–	6	3.257	0.033	0.447	0.024	2.619E-13	0.053E-13
–	7	3.072	0.041	0.321	0.021	1.557E-13	0.033E-13
–	8	3.019	0.053	0.381	0.031	6.525E-14	0.199E-14
–	9	2.826	0.078	0.346	0.037	3.062E-14	0.127E-14
–	10	2.721	0.133	0.221	0.063	1.871E-14	0.153E-14
Abell 13	1	5.184	0.348	0.807	0.336	5.463e-13	0.764e-13
–	2	5.541	0.391	0.747	0.201	3.992e-13	0.348e-13
–	3	4.682	0.182	0.326	0.078	1.980e-13	0.092e-13
–	4	4.985	0.219	0.266	0.063	1.043e-13	0.044e-13
–	5	4.152	0.225	–[8]	–	4.627e-14	0.248e-14
–	6	4.174	0.273	–	–	3.081e-14	0.177e-14
–	7	4.150	0.300	0.466	0.141	1.595e-14	0.142e-14
–	8	3.758	0.493	–	–	8.115e-15	0.899e-15
–	9	4.191	1.012	–	–	3.035e-15	0.517e-15
Abell 68	1	7.487	0.726	0.254	0.162	1.351E-12	0.087E-12
–	2	7.803	0.635	0.274	0.081	6.687E-13	0.319E-13
–	3	6.966	0.541	–	–	2.102E-13	0.103E-13
–	4	5.897	0.711	–	–	4.401E-14	0.315E-14
–	5	5.621	1.241	–	–	1.627E-14	0.170E-14
–	6	3.606	0.893	–	–	7.168E-15	1.210E-15
Abell 85	1	3.618	0.084	1.161	0.089	1.043E-11	0.030E-11
–	2	5.089	0.145	0.567	0.077	3.921E-12	0.120E-12
–	3	5.321	0.103	0.521	0.053	1.946E-12	0.046E-12
–	4	5.972	0.185	0.379	0.062	1.043E-12	0.029E-12
–	5	6.269	0.195	0.428	0.069	6.139E-13	0.185E-13
–	6	6.246	0.273	0.356	0.095	3.046E-13	0.126E-13
–	7	6.305	0.157	0.319	0.047	2.548E-13	0.058E-13
–	8	6.047	0.292	0.322	0.080	1.005E-13	0.039E-13
–	9	5.679	0.404	–	–	5.382E-14	0.252E-14
–	10	7.177	1.115	–	–	3.768E-14	2.496E-15
Abell 133	1	2.376	0.044	1.056	0.070	4.090E-12	0.169E-12
–	2	3.848	0.100	0.872	0.098	1.338E-12	0.066E-12
–	3	4.300	0.087	0.555	0.061	5.686E-13	0.196E-13
–	4	4.222	0.107	0.472	0.072	2.436E-13	0.102E-13
–	5	4.159	0.137	0.338	0.081	1.322E-13	0.066E-13
–	6	3.997	0.176	0.397	0.105	7.203E-14	0.471E-14
–	7	3.738	0.180	0.457	0.095	4.473E-14	0.286E-14
–	8	3.940	0.337	0.423	0.171	1.829E-14	0.209E-14
–	9	2.658	0.296	0.381	0.172	6.742E-15	1.381E-15
–	10	2.314	0.640	–	–	3.300E-15	1.160E-15
Abell 209	1	6.946	0.855	0.778	0.486	1.608E-12	0.260E-12
–	2	6.766	0.422	0.336	0.072	7.642E-13	0.384E-13
–	3	7.303	0.470	–	–	3.035E-13	0.147E-13
–	4	7.993	0.668	–	–	1.053E-13	0.056E-13
–	5	6.892	0.915	0.233	0.164	5.042E-14	0.421E-14
–	6	5.603	0.821	–	–	2.559E-14	0.253E-14
–	7	4.867	0.776	–	–	1.127E-14	0.135E-14
Abell 262	1	1.270	0.010	0.495	0.030	2.636E-12	0.143E-12
–	2	1.889	0.032	1.108	0.083	1.182E-12	0.080E-12
–	3	2.121	0.022	0.656	0.037	5.865E-13	0.220E-13
–	4	2.140	0.025	0.408	0.028	3.609E-13	0.126E-13
–	5	2.141	0.027	0.381	0.027	2.596E-13	0.092E-13
–	6	2.161	0.034	0.380	0.030	1.783E-13	0.070E-13
–	7	2.198	0.040	0.359	0.024	1.380E-13	0.046E-13
–	8	2.102	0.034	0.322	0.027	7.796E-14	0.311E-14
–	9	1.982	0.041	0.306	0.027	4.649E-14	0.220E-14
–	10	1.983	0.072	0.299	0.046	3.336E-14	0.270E-14
Abell 383	1	3.643	0.078	0.746	0.062	3.913E-12	0.132E-12
–	2	5.573	0.374	0.363	0.116	6.474E-13	0.352E-13
–	3	4.812	0.251	0.325	0.095	1.463E-13	0.084E-13
–	4	4.449	0.543	–	–	2.879E-14	0.236E-14

Table 5. continued.

Cluster	Annulus	T (keV)	σ_T (keV)	A	σ_A	F (0.3–10.0 keV) erg cm^{-2} s^{-1} arcmin^{-2}	σ_F (0.3–10.0 keV) erg cm^{-2} s^{-1} arcmin^{-2}
–	5	3.615	0.628	–	–	1.149E-14	0.135E-14
–	6	3.717	0.976	–	–	6.276E-15	0.983E-15
–	7	3.678	1.145	–	–	2.919E-15	0.645E-15
–	8	0.000	0.000	–	–	2.322E-15	0.578E-15
Abell 399	1	9.840	1.980	0.465	0.097	1.277E-12	0.088E-12
–	2	6.665	0.525	–	–	9.888E-13	0.527E-13
–	3	6.704	0.279	–	–	7.264E-13	0.333E-13
–	4	7.509	0.451	0.287	0.103	4.289E-13	0.199E-13
–	5	6.425	0.332	0.343	0.123	2.669E-13	0.145E-13
–	6	6.445	0.375	0.330	0.093	1.680E-13	0.082E-13
–	7	6.258	0.333	–	–	1.174E-13	0.055E-13
–	8	6.520	0.464	0.154	0.135	6.528E-14	0.413E-14
–	9	7.380	0.854	–	–	3.345E-14	0.230E-14
Abell 400	1	2.303	0.259	0.551	0.137	2.112e-13	0.353e-13
–	2	2.326	0.153	–	–	1.851e-13	0.267e-13
–	3	2.340	0.071	0.677	0.076	1.792e-13	0.134e-13
–	4	2.126	0.044	0.452	0.051	1.273e-13	0.082e-13
–	5	2.122	0.046	0.414	0.047	1.012e-13	0.063e-13
–	6	2.142	0.050	0.398	0.050	7.716e-14	0.600e-14
–	7	1.906	0.051	0.277	0.030	5.831e-14	0.338e-14
–	8	2.067	0.060	0.384	0.052	3.667e-14	0.274e-14
–	9	1.989	0.073	0.373	0.053	2.116e-14	0.193e-14
–	10	2.027	0.110	–	–	1.575e-14	1.770e-15
Abell 478	1	4.499	0.049	0.551	0.019	2.252E-11	0.016E-11
–	2	6.086	0.085	0.403	0.020	6.245E-12	0.055E-12
–	3	6.290	0.069	0.383	0.016	2.400E-12	0.022E-12
–	4	6.610	0.108	0.335	0.023	7.404E-13	0.108E-13
–	5	6.497	0.138	0.307	0.028	3.604E-13	0.067E-13
–	6	6.508	0.201	0.276	0.040	1.766E-13	0.047E-13
–	7	6.124	0.217	0.415	0.045	8.236E-14	0.238E-14
–	8	8.367	0.533	–	–	3.657E-14	0.125E-14
Abell 496	1	2.479	0.032	1.038	0.055	9.749E-12	0.240E-12
–	2	3.176	0.048	0.715	0.046	3.833E-12	0.100E-12
–	3	3.682	0.050	0.572	0.032	1.821E-12	0.036E-12
–	4	4.135	0.063	0.449	0.038	8.506E-13	0.195E-13
–	5	4.233	0.070	0.428	0.042	5.433E-13	0.138E-13
–	6	4.536	0.122	0.290	0.047	3.372E-13	0.094E-13
–	7	4.185	0.080	0.333	0.042	2.164E-13	0.058E-13
–	8	4.130	0.111	0.300	0.041	1.146E-13	0.036E-13
–	9	4.020	0.144	–	–	5.824E-14	0.231E-14
–	10	4.289	0.305	–	–	3.519E-14	0.225E-14
Abell 520	1	9.176	1.306	0.210	0.121	7.735E-13	0.470E-13
–	2	7.264	0.593	–	–	6.521E-13	0.352E-13
–	3	8.960	0.509	0.285	0.054	4.198E-13	0.150E-13
–	4	8.576	0.744	–	–	1.357E-13	0.056E-13
–	5	6.629	0.516	–	–	5.353E-14	0.272E-14
–	6	10.682	1.638	–	–	3.200E-14	0.199E-15
–	7	4.873	0.709	–	–	1.326E-14	0.108E-14
–	8	6.524	2.797	–	–	4.687E-15	0.856E-15
Abell 576	1	3.270	0.411	0.838	0.536	9.522E-13	2.921E-13
–	2	3.782	0.364	0.712	0.320	6.781E-13	1.163E-13
–	3	3.804	0.165	0.714	0.143	4.255E-13	0.363E-13
–	4	4.068	0.192	0.323	0.122	2.755E-13	0.218E-13
–	5	4.262	0.188	0.529	0.155	2.270E-13	0.198E-13
–	6	3.962	0.212	0.430	0.139	1.335E-13	0.120E-13
–	7	3.322	0.137	0.432	0.091	7.780E-14	0.577E-14
–	8	3.054	0.216	0.261	0.081	3.749E-14	0.352E-14
–	9	3.212	0.304	–	–	2.039E-14	0.241E-14
–	10	2.759	0.681	–	–	9.953E-15	2.048E-15
Abell 665	1	7.240	0.561	0.112	0.128	1.017E-12	0.051E-12
–	2	7.810	0.291	0.298	0.062	9.722E-13	0.265E-13
–	3	7.998	0.191	0.282	0.036	5.992E-13	0.111E-13
–	4	8.114	0.277	0.388	0.061	2.001E-13	0.055E-13
–	5	7.881	0.367	0.241	0.075	9.623E-14	0.320E-14
–	6	6.475	0.327	0.350	0.104	5.830E-14	0.275E-14

Table 5. continued.

Cluster	Annulus	T (keV)	σ_T (keV)	A	σ_A	F (0.3–10.0 keV) erg cm^{-2} s^{-1} arcmin^{-2}	σ_F (0.3–10.0 keV) erg cm^{-2} s^{-1} arcmin^{-2}
–	7	4.689	0.331	0.187	0.066	1.847E-14	0.103E-14
–	8	2.222	0.281	–	–	4.497E-15	0.702E-15
–	9	1.540	0.198	–	–	1.300E-15	0.439E-15
–	10	1.160	0.135	–	–	1.309E-15	0.593E-15
Abell 773	1	10.816	1.210	0.525	0.173	1.888E-12	0.139E-12
–	2	6.933	0.725	–	–	8.006E-13	0.067E-13
–	3	8.095	0.651	0.299	0.144	2.624E-13	0.202E-13
–	4	7.505	0.907	–	–	8.074E-14	0.687E-14
–	5	7.463	1.243	0.238	0.277	3.993E-14	0.487E-14
–	6	5.162	1.127	–	–	1.194E-14	0.209E-14
–	7	3.538	0.959	–	–	5.400E-15	1.328E-15
Abell 1060	1	3.081	0.108	0.759	0.110	1.194E-12	0.084E-12
–	2	3.374	0.071	0.671	0.071	9.606E-13	0.429E-13
–	3	3.330	0.040	0.469	0.030	7.914E-13	0.177E-13
–	4	3.291	0.037	0.483	0.027	5.704E-13	0.121E-13
–	5	3.250	0.039	0.401	0.025	4.243E-13	0.090E-14
–	6	3.220	0.042	0.491	0.030	3.336E-13	0.080E-14
–	7	3.158	0.035	0.437	0.022	2.361E-13	0.045E-14
–	8	3.012	0.043	0.415	0.024	1.573E-13	0.035E-14
–	9	3.011	0.051	0.404	0.026	9.503E-14	0.234E-14
–	10	3.087	0.101	0.419	0.054	6.314E-14	0.300E-14
Abell 1068	1	3.123	0.055	0.631	0.048	5.377E-12	0.148E-12
–	2	4.691	0.197	0.384	0.053	1.078E-12	0.038E-12
–	3	4.743	0.201	–	–	2.483E-13	0.094E-13
–	4	5.366	0.352	–	–	6.827E-14	0.335E-14
–	5	5.163	0.543	–	–	2.801E-14	0.183E-14
–	6	5.287	0.867	–	–	1.384E-14	0.129E-14
–	7	2.220	0.562	–	–	2.919E-15	0.557E-15
Abell 1413	1	7.682	0.332	0.409	0.079	4.639E-12	0.012E-12
–	2	7.995	0.327	0.396	0.076	1.899E-12	0.056E-12
–	3	6.898	0.269	0.492	0.061	6.280E-13	0.176E-13
–	4	7.013	0.403	0.338	0.075	2.006E-13	0.071E-13
–	5	6.806	0.366	–	–	8.671E-14	0.345E-14
–	6	6.423	0.530	0.163	0.104	4.190E-14	0.244E-14
–	7	5.650	0.615	–	–	2.249E-14	0.146E-14
–	8	3.559	0.528	–	–	8.913E-15	1.024E-15
–	9	5.015	2.030	–	–	2.495E-15	0.755E-15
Abell 1589	1	2.634	2.668	0.276	0.146	2.234E-13	1.104E-13
–	2	5.080	0.780	–	–	2.203E-13	0.259E-13
–	3	4.676	0.308	–	–	1.645E-13	0.147E-13
–	4	5.614	0.463	0.281	0.115	1.150E-13	0.080E-13
–	5	4.443	0.339	–	–	7.515E-14	0.602E-14
–	6	3.326	0.203	0.317	0.079	4.498E-14	0.391E-14
–	7	3.583	0.291	–	–	2.948E-14	0.245E-14
–	8	3.232	0.445	–	–	9.579E-15	1.204E-15
–	9	1.588	0.204	–	–	1.953E-15	0.719E-15
Abell 1650	1	5.145	0.114	0.654	0.069	4.832E-12	0.122E-12
–	2	6.064	0.158	0.543	0.059	2.196E-12	0.053E-12
–	3	5.812	0.126	0.396	0.040	9.004E-13	0.173E-13
–	4	5.951	0.163	0.306	0.049	3.821E-13	0.090E-13
–	5	5.401	0.141	0.332	0.061	1.828E-13	0.056E-13
–	6	5.235	0.206	0.199	0.051	1.017E-13	0.033E-13
–	7	4.967	0.244	–	–	4.088E-14	0.149E-14
–	8	3.938	0.337	–	–	1.606E-14	0.100E-14
–	9	1.991	0.219	–	–	4.182E-15	0.642E-15
Abell 1689	1	9.435	0.280	0.437	0.048	9.087E-12	0.117E-12
–	2	11.619	0.593	0.258	0.031	2.505E-12	0.047E-12
–	3	9.927	0.309	–	–	7.202E-13	0.122E-13
–	4	8.234	0.360	–	–	1.702E-13	0.039E-13
–	5	9.743	0.780	–	–	7.142E-14	0.216E-14
–	6	7.357	0.913	–	–	2.785E-14	0.127E-14
–	7	7.804	1.481	–	–	1.113E-14	0.078E-14
Abell 1775	1	4.341	0.382	1.687	0.517	7.223E-13	1.356E-13
–	2	3.716	0.155	0.913	0.157	7.036E-13	0.563E-13
–	3	3.862	0.089	0.711	0.070	3.867E-13	0.165E-13
–	4	3.660	0.116	0.582	0.077	1.647E-13	0.085E-13

Table 5. continued.

Cluster	Annulus	T (keV)	σ_T (keV)	A	σ_A	F (0.3–10.0 keV) erg cm^{-2} s^{-1} arcmin^{-2}	σ_F (0.3–10.0 keV) erg cm^{-2} s^{-1} arcmin^{-2}
–	5	3.413	0.116	0.404	0.083	8.308E-14	0.522E-14
–	6	3.896	0.221	0.315	0.120	5.016E-14	0.403E-14
–	7	3.276	0.166	0.363	0.078	2.834E-14	0.196E-14
–	8	3.201	0.268	–	–	1.386E-14	0.119E-14
–	9	3.546	0.744	–	–	5.478E-15	0.793E-15
–	10	3.217	0.880	–	–	4.229E-15	0.947E-15
Abell 1795	1	3.881	0.037	0.702	0.027	1.328E-11	0.011E-11
–	2	4.707	0.054	0.553	0.027	6.189E-12	0.064E-12
–	3	5.742	0.070	0.407	0.022	2.267E-12	0.022E-12
–	4	5.958	0.092	0.338	0.028	8.825E-13	0.115E-13
–	5	6.124	0.112	0.316	0.021	4.640E-13	0.056E-13
–	6	6.060	0.141	–	–	2.574E-13	0.036E-13
–	7	5.805	0.150	–	–	1.394E-13	0.020E-13
–	8	5.744	0.248	–	–	5.622E-14	0.121E-14
–	9	4.880	0.292	–	–	2.091E-14	0.086E-14
–	10	4.426	0.693	–	–	1.115E-14	0.099E-14
Abell 1835	1	6.062	0.121	0.457	0.034	1.099E-11	0.012E-11
–	2	10.524	0.495	0.284	0.046	1.743E-12	0.383E-12
–	3	9.123	0.497	–	–	4.054E-13	0.101E-13
–	4	8.632	0.793	–	–	8.954E-14	0.390E-14
–	5	7.667	0.741	–	–	4.165E-14	0.177E-14
–	6	8.092	1.650	–	–	1.544E-14	0.126E-14
–	7	4.969	1.125	–	–	6.206E-15	0.763E-15
Abell 1835 a[9]	1	5.896	0.114	0.513	0.034	1.078E-11	0.011E-11
–	2	10.024	0.466	0.364	0.082	1.682E-12	0.049E-12
–	3	9.790	0.456	0.266	0.062	4.036E-13	0.110E-13
–	4	8.517	0.630	–	–	7.844E-14	0.313E-14
–	5	7.891	0.958	–	–	3.176E-14	0.170E-14
–	6	6.411	1.301	–	–	1.120E-14	0.110E-14
–	7	7.612	2.568	–	–	6.764E-15	0.828E-15
–	8	3.138	0.926	–	–	2.740E-15	0.613E-15
–	9	3.325	1.748	–	–	1.290E-15	0.554E-15
Abell 1837	1	3.959	0.256	1.268	0.386	5.620E-13	0.921E-13
–	2	4.110	0.143	0.484	0.106	4.097E-13	0.253E-13
–	3	3.855	0.088	0.469	0.053	2.367E-13	0.089E-13
–	4	3.860	0.112	0.453	0.068	1.071E-13	0.050E-13
–	5	3.393	0.122	0.196	0.035	5.081E-14	0.218E-14
–	6	3.286	0.160	–	–	2.941E-14	0.129E-14
–	7	2.678	0.122	–	–	1.616E-14	0.079E-14
–	8	2.893	0.320	–	–	6.978E-15	0.554E-15
–	9	1.621	0.099	–	–	2.805E-15	0.382E-15
Abell 1914	1	11.219	1.021	0.614	0.126	4.565E-12	0.188E-12
–	2	12.007	0.728	0.329	0.083	3.317E-12	0.114E-12
–	3	10.327	0.422	0.242	0.070	7.948E-13	0.248E-13
–	4	8.967	0.712	0.336	0.117	1.845E-13	0.090E-13
–	5	9.057	1.015	0.326	0.194	8.221E-14	0.627E-14
–	6	8.996	1.556	0.280	0.238	3.770E-14	0.364E-14
–	7	8.053	1.404	–	–	1.673E-14	0.175E-14
Abell 1991	1	1.785	0.033	0.654	0.043	3.296E-12	0.143E-12
–	2	2.611	0.057	0.778	0.082	9.264E-13	0.568E-13
–	3	2.795	0.075	0.451	0.050	2.954E-13	0.139E-13
–	4	2.603	0.087	0.310	0.044	9.172E-14	0.505E-14
–	5	2.388	0.106	–	–	5.005E-14	0.321E-14
–	6	2.377	0.183	0.308	0.100	2.319E-14	0.301E-14
–	7	2.262	0.235	0.230	0.072	1.140E-14	0.146E-14
–	8	1.573	0.126	–	–	4.611E-15	1.003E-15
Abell 2029	1	5.585	0.134	0.951	0.065	1.900E-11	0.027E-11
–	2	7.273	0.224	0.483	0.058	8.060E-12	0.134E-12
–	3	7.827	0.189	0.377	0.044	2.905E-12	0.047E-12
–	4	7.558	0.250	0.382	0.061	1.029E-12	0.025E-12
–	5	7.695	0.322	0.367	0.064	5.066E-13	0.149E-13
–	6	8.187	0.403	–	–	2.837E-13	0.084E-13
–	7	7.531	0.429	–	–	1.515E-13	0.064E-13
–	8	10.599	1.042	–	–	6.345E-14	0.342E-14

Table 5. continued.

Cluster	Annulus	T (keV)	σ_T (keV)	A	σ_A	F (0.3–10.0 keV) erg cm^{-2} s^{-1} arcmin^{-2}	σ_F (0.3–10.0 keV) erg cm^{-2} s^{-1} arcmin^{-2}
Abell 2052	1	1.968	0.021	0.701	0.031	5.517E-12	0.127E-12
–	2	2.839	0.038	0.805	0.037	2.871E-12	0.067E-12
–	3	3.105	0.033	0.552	0.026	1.085E-12	0.021E-12
–	4	3.254	0.041	0.454	0.029	4.902E-13	0.113E-13
–	5	3.230	0.049	0.393	0.032	2.827E-13	0.075E-13
–	6	3.053	0.058	0.442	0.038	1.698E-13	0.055E-13
–	7	2.913	0.061	0.341	0.031	9.754E-14	0.300E-14
–	8	3.027	0.103	0.420	0.057	4.174E-14	0.217E-14
–	9	2.633	0.119	0.421	0.076	1.733E-14	0.151E-14
–	10	2.517	0.197	–	–	1.146E-14	0.136E-14
Abell 2065	1	4.236	0.123	0.829	0.124	2.491E-12	1.383E-13
–	2	5.182	0.190	0.402	0.096	1.306E-12	0.058E-12
–	3	5.704	0.176	0.461	0.059	7.381E-13	0.214E-13
–	4	5.906	0.210	0.343	0.065	3.649E-13	0.118E-13
–	5	5.823	0.242	0.309	0.080	2.276E-13	0.086E-13
–	6	5.374	0.188	0.430	0.103	1.441E-13	0.070E-13
–	7	4.880	0.192	0.331	0.066	9.532E-14	0.377E-14
–	8	4.719	0.339	–	–	4.190E-14	0.215E-14
–	9	4.824	0.655	–	–	1.682E-14	0.145E-14
–	10	4.967	1.320	–	–	1.160E-14	0.179E-14
Abell 2163	1	9.871	1.153	0.648	0.227	3.807E-12	0.255E-12
–	2	11.801	1.177	0.250	0.068	2.939E-12	0.112E-12
–	3	12.472	0.835	–	–	1.337E-12	0.049E-12
–	4	13.101	1.117	0.331	0.095	4.721E-13	0.230E-13
–	5	15.446	1.803	–	–	2.505E-13	0.122E-13
–	6	13.591	1.745	–	–	1.397E-13	0.083E-13
–	7	13.884	2.783	–	–	6.871E-14	0.420E-14
–	8	7.125	1.593	–	–	2.234E-14	0.205E-14
–	9	6.906	5.839	–	–	3.493E-15	1.253E-15
Abell 2199	1	3.011	0.052	1.023	0.063	8.126E-12	0.211E-12
–	2	3.721	0.066	0.695	0.050	4.617E-12	0.107E-12
–	3	4.129	0.046	0.483	0.029	2.649E-12	0.041E-12
–	4	4.278	0.053	0.498	0.035	1.256E-12	0.024E-12
–	5	4.161	0.061	0.430	0.037	7.471E-13	0.161E-13
–	6	4.272	0.074	0.383	0.044	4.469E-13	0.114E-13
–	7	4.251	0.071	0.396	0.042	2.695E-13	0.066E-13
–	8	4.117	0.099	0.519	0.050	1.245E-13	0.039E-13
–	9	4.422	0.192	–	–	6.276E-14	0.229E-14
–	10	4.611	0.390	–	–	3.822E-14	0.230E-14
Abell 2204	1	4.807	0.071	0.655	0.035	1.879E-11	0.020E-11
–	2	8.706	0.433	0.348	0.068	3.387E-12	0.080E-12
–	3	8.335	0.269	0.370	0.061	9.448E-13	0.238E-13
–	4	8.384	0.463	0.372	0.078	2.374E-13	0.085E-13
–	5	8.323	0.575	–	–	1.190E-13	0.048E-13
–	6	9.085	1.276	–	–	5.940E-14	0.298E-14
–	7	7.499	1.109	–	–	2.721E-14	0.166E-14
–	8	7.486	3.432	–	–	6.861E-15	1.134E-15
Abell 2218	1	7.295	0.806	0.730	0.386	1.393E-12	0.180E-12
–	2	8.342	0.599	0.368	0.148	9.645E-13	0.579E-13
–	3	6.759	0.304	0.230	0.059	3.572E-13	0.157E-13
–	4	6.675	0.451	–	–	1.048E-13	0.054E-13
–	5	5.484	0.610	–	–	4.587E-14	0.287E-14
–	6	6.357	0.857	–	–	2.687E-14	0.199E-14
–	7	3.387	0.392	–	–	1.077E-14	0.113E-14
–	8	1.323	0.095	–	–	2.543E-15	0.720E-15
–	9	0.609	0.098	–	–	7.458E-16	4.554E-16
Abell 2256	1	6.241	2.232	0.342	0.063	8.576E-13	0.800E-13
–	2	6.173	0.722	–	–	8.819E-13	0.474E-13
–	3	5.937	0.302	–	–	1.031E-12	0.039E-12
–	4	5.813	0.246	–	–	7.972E-13	0.289E-13
–	5	5.497	0.236	0.434	0.061	5.563E-13	0.231E-13
–	6	6.633	0.263	–	–	4.054E-13	0.148E-13
–	7	6.704	0.240	0.278	0.063	2.179E-13	0.079E-13
–	8	6.767	0.345	–	–	1.103E-13	0.044E-13
–	9	7.647	0.889	–	–	4.244E-14	0.223E-14
–	10	6.727	1.572	–	–	1.428E-14	0.181E-14

Table 5. continued.

Cluster	Annulus	T (keV)	σ_T (keV)	A	σ_A	F (0.3–10.0 keV) erg cm^{-2} s^{-1} arcmin^{-2}	σ_F (0.3–10.0 keV) erg cm^{-2} s^{-1} arcmin^{-2}
Abell 2319	1	8.310	0.811	0.611	0.315	2.251E-12	0.221E-12
–	2	10.162	0.716	0.316	0.132	2.052E-12	0.089E-12
–	3	8.944	0.308	0.265	0.048	2.182E-12	0.039E-12
–	4	8.894	0.272	0.303	0.041	1.738E-12	0.028E-12
–	5	8.427	0.195	0.312	0.044	1.181E-12	0.021E-12
–	6	8.919	0.333	0.313	0.053	7.701E-13	0.163E-13
–	7	9.006	0.313	0.233	0.037	5.671E-13	0.099E-13
–	8	8.871	0.443	–	–	3.489E-13	0.072E-13
–	9	8.448	0.362	–	–	1.907E-13	0.045E-13
–	10	7.671	0.703	–	–	1.211E-13	0.047E-13
Abell 2589	1	3.349	0.107	0.975	0.150	1.749E-12	0.134E-12
–	2	3.730	0.110	0.816	0.096	9.821E-13	0.515E-13
–	3	3.622	0.071	0.582	0.045	6.220E-13	0.189E-13
–	4	3.575	0.081	0.567	0.050	3.139E-13	0.108E-13
–	5	3.579	0.099	0.437	0.055	1.826E-13	0.072E-13
–	6	3.625	0.129	0.449	0.070	1.050E-13	0.051E-13
–	7	3.378	0.098	0.392	0.061	7.137E-14	0.337E-14
–	8	3.473	0.217	0.442	0.097	3.668E-14	0.260E-14
–	9	2.863	0.276	0.307	0.095	1.631E-14	0.174E-14
–	10	4.660	0.880	–	–	1.628E-14	0.174E-14
Abell 2597	1	3.054	0.027	0.530	0.020	1.113E-11	0.011E-11
–	2	3.800	0.055	0.394	0.030	2.562E-12	0.045E-12
–	3	3.869	0.056	0.310	0.028	6.003E-13	0.117E-13
–	4	3.722	0.092	0.299	0.045	1.543E-13	0.050E-13
–	5	3.665	0.120	0.268	0.057	7.358E-14	0.307E-14
–	6	3.399	0.142	0.278	0.079	3.380E-14	0.215E-14
–	7	3.170	0.178	0.372	0.073	1.552E-14	0.104E-14
–	8	2.751	0.311	–	–	6.340E-15	0.593E-15
–	9	2.877	0.438	–	–	3.688E-15	0.427E-15
Abell 2626	1	2.610	0.042	0.693	0.054	2.492E-12	0.097E-12
–	2	3.084	0.066	0.571	0.056	8.441E-13	0.354E-13
–	3	3.134	0.049	0.501	0.036	4.176E-13	0.126E-13
–	4	3.323	0.064	0.448	0.047	1.722E-13	0.064E-13
–	5	3.251	0.086	0.413	0.047	8.561E-14	0.352E-14
–	6	3.288	0.119	–	–	4.422E-14	0.198E-14
–	7	2.762	0.149	0.229	0.055	2.233E-14	0.148E-14
–	8	1.973	0.133	0.271	0.073	7.593E-15	1.039E-15
–	9	1.901	0.261	0.289	0.124	2.561E-15	0.784E-15
–	10	1.685	0.158	–	–	2.120E-15	0.859E-15
Abell 2667	1	5.530	0.196	0.554	0.061	5.890E-12	0.142E-12
–	2	8.529	0.455	0.352	0.061	1.321E-12	0.041E-12
–	3	7.616	0.442	–	–	3.116E-13	0.108E-13
–	4	7.788	0.810	–	–	7.479E-14	0.366E-14
–	5	5.558	0.810	–	–	2.791E-14	0.190E-14
–	6	8.407	2.186	–	–	1.370E-14	0.143E-14
–	7	3.807	0.973	–	–	5.288E-15	0.786E-15
–	8	3.145	0.777	–	–	3.624E-15	0.628E-15
Abell 2717	1	2.040	0.039	0.953	0.085	8.896E-13	0.607E-13
–	2	2.538	0.057	0.819	0.079	3.955E-13	0.240E-13
–	3	2.430	0.044	0.495	0.037	1.952E-13	0.079E-13
–	4	2.497	0.059	0.437	0.044	8.545E-14	0.407E-14
–	5	2.291	0.078	0.359	0.043	4.538E-14	0.250E-14
–	6	2.303	0.107	0.384	0.058	2.579E-14	0.184E-14
–	7	2.310	0.128	0.364	0.063	1.419E-14	0.114E-14
–	8	2.085	0.119	0.473	0.112	5.339E-15	0.850E-15
–	9	1.954	0.199	–	–	2.055E-15	0.542E-15
–	10	1.682	0.118	–	–	1.729E-15	0.642E-15
Abell 3112	1	3.379	0.036	1.113	0.053	9.632E-12	0.184E-12
–	2	4.797	0.100	0.590	0.053	3.081E-12	0.071E-13
–	3	4.979	0.091	0.427	0.040	1.020E-12	0.021E-13
–	4	4.876	0.123	0.518	0.063	3.337E-13	0.108E-13
–	5	4.552	0.165	0.270	0.071	1.499E-13	0.060E-13
–	6	4.697	0.226	0.212	0.050	8.087E-14	0.300E-14
–	7	4.184	0.180	–	–	4.278E-14	0.184E-14
–	8	4.048	0.328	–	–	1.723E-14	0.115E-14
–	9	2.354	0.246	–	–	6.746E-15	0.834E-15

Table 5. continued.

Cluster	Annulus	T (keV)	σ_T (keV)	A	σ_A	F (0.3–10.0 keV) erg cm^{-2} s^{-1} arcmin^{-2}	σ_F (0.3–10.0 keV) erg cm^{-2} s^{-1} arcmin^{-2}
Abell 3158	1	6.253	0.470	0.710	0.472	1.515E-12	0.230E-12
–	2	5.305	0.183	0.724	0.130	1.239E-12	0.066E-12
–	3	5.627	0.160	0.350	0.050	9.060E-13	0.221E-13
–	4	5.293	0.114	0.444	0.054	5.160E-13	0.140E-13
–	5	5.018	0.125	0.433	0.060	3.296E-13	0.104E-13
–	6	5.230	0.151	0.432	0.071	2.049E-13	0.073E-13
–	7	5.014	0.163	0.285	0.066	1.362E-13	0.049E-13
–	8	5.875	0.404	0.279	0.118	7.133E-14	0.406E-14
–	9	6.460	0.525	–	–	3.595E-14	0.244E-14
Abell 3526	1	1.299	0.037	0.503	0.012	1.013E-11	0.014E-11
–	2	1.983	0.010	1.831	0.054	4.244E-12	0.120E-12
–	3	2.558	0.012	1.492	0.032	2.147E-12	0.037E-12
–	4	2.907	0.020	1.176	0.028	1.194E-12	0.020E-12
–	5	3.207	0.023	0.782	0.025	7.746E-13	0.126E-13
–	6	3.268	0.027	0.591	0.023	5.541E-13	0.093E-13
–	7	3.324	0.024	0.482	0.018	4.419E-13	0.061E-13
–	8	3.369	0.030	0.447	0.021	2.902E-13	0.047E-13
–	9	3.372	0.033	0.447	0.023	1.864E-13	0.033E-13
–	10	3.300	0.056	0.487	0.039	1.404E-13	0.043E-13
Abell 3558	1	4.677	0.136	0.761	0.082	2.637E-12	0.094E-12
–	2	5.552	0.168	0.476	0.056	1.790E-12	0.045E-12
–	3	5.757	0.099	0.455	0.032	1.161E-12	0.018E-12
–	4	5.724	0.106	0.378	0.032	6.826E-13	0.108E-13
–	5	5.492	0.105	0.353	0.031	5.075E-13	0.081E-13
–	6	5.114	0.078	0.412	0.034	3.728E-13	0.068E-13
–	7	5.122	0.071	0.294	0.028	2.667E-13	0.042E-13
–	8	4.878	0.097	0.337	0.040	1.373E-13	0.031E-13
–	9	5.043	0.133	0.264	0.053	6.947E-14	0.210E-14
–	10	4.710	0.264	0.376	0.119	4.147E-14	0.278E-14
Abell 3560	1	3.331	0.359	0.346	0.115	2.771E-13	0.306E-13
–	2	3.253	0.190	–	–	2.286E-13	0.224E-13
–	3	3.997	0.139	0.393	0.083	2.083E-13	0.118E-13
–	4	3.841	0.141	0.458	0.083	1.293E-13	0.075E-13
–	5	3.479	0.164	0.351	0.080	9.652E-14	0.617E-14
–	6	3.827	0.182	0.392	0.100	6.497E-14	0.454E-14
–	7	3.693	0.163	0.285	0.069	4.344E-14	0.244E-14
–	8	3.528	0.207	0.329	0.065	2.858E-14	0.176E-14
–	9	3.856	0.246	–	–	2.028E-14	0.138E-14
–	10	4.093	0.442	–	–	1.519E-14	0.141E-14
Abell 3581	1	1.396	0.017	0.432	0.022	3.243E-12	0.113E-12
–	2	1.585	0.013	0.593	0.028	1.484E-12	0.056E-12
–	3	1.764	0.020	0.536	0.022	5.915E-13	0.185E-13
–	4	1.895	0.028	0.346	0.022	2.212E-13	0.080E-13
–	5	1.909	0.035	0.320	0.025	1.221E-13	0.052E-13
–	6	1.886	0.046	0.307	0.030	6.876E-14	0.366E-14
–	7	1.843	0.046	0.238	0.023	4.600E-14	0.222E-14
–	8	1.648	0.034	0.195	0.023	2.526E-14	0.154E-14
–	9	1.623	0.042	0.225	0.031	1.388E-14	0.121E-14
–	10	1.535	0.092	0.176	0.048	9.583E-15	1.583E-15
Abell 3827	1	7.938	0.565	0.682	0.206	2.633E-12	0.169E-12
–	2	6.944	0.373	0.345	0.091	1.718E-12	0.063E-12
–	3	7.144	0.247	0.378	0.054	8.827E-13	0.218E-13
–	4	6.920	0.304	0.385	0.044	3.679E-13	0.092E-13
–	5	6.683	0.257	–	–	1.902E-13	0.053E-13
–	6	6.926	0.498	–	–	1.038E-13	0.033E-13
–	7	5.804	0.382	–	–	5.573E-14	0.203E-14
–	8	5.867	0.650	–	–	2.549E-14	0.146E-14
–	9	6.561	1.230	–	–	1.033E-14	0.129E-14
Abell 3911	1	6.454	0.707	1.265	0.716	5.754E-13	1.407E-13
–	2	6.636	0.467	0.666	0.245	4.875E-13	0.452E-13
–	3	6.389	0.233	0.401	0.080	3.971E-13	0.150E-13
–	4	5.538	0.246	0.316	0.077	2.185E-13	0.087E-13

Table 5. continued.

Cluster	Annulus	T (keV)	σ_T (keV)	A	σ_A	F (0.3–10.0 keV) erg cm^{-2} s^{-1} arcmin^{-2}	σ_F (0.3–10.0 keV) erg cm^{-2} s^{-1} arcmin^{-2}
–	5	5.591	0.301	0.176	0.049	1.203E-13	0.042E-13
–	6	5.953	0.405	–	–	7.168E-14	0.284E-14
–	7	4.981	0.290	–	–	4.071E-14	0.185E-14
–	8	3.697	0.420	–	–	1.351E-14	0.120E-14
–	9	3.215	0.379	–	–	8.326E-15	1.054E-15
–	10	3.611	1.182	–	–	5.228E-15	1.288E-15
Abell 3921	1	5.234	0.245	0.588	0.160	1.322E-12	0.091E-12
–	2	6.095	0.287	0.341	0.095	9.003E-13	0.382E-13
–	3	5.570	0.183	0.377	0.057	4.962E-13	0.145E-13
–	4	5.302	0.144	0.354	0.059	2.444E-13	0.078E-13
–	5	5.312	0.170	0.479	0.090	1.409E-13	0.062E-13
–	6	5.036	0.232	0.313	0.059	7.505E-14	0.303E-14
–	7	5.577	0.337	–	–	4.503E-14	0.178E-14
–	8	4.711	0.371	–	–	2.138E-14	0.122E-14
–	9	2.551	0.231	–	–	6.745E-15	0.851E-15
–	10	2.854	0.638	–	–	5.575E-15	0.989E-15
Abell 4059	1	2.868	0.071	1.356	0.108	2.976E-12	0.155E-12
–	2	3.688	0.077	0.880	0.069	1.852E-12	0.066E-12
–	3	4.087	0.060	0.503	0.038	9.636E-13	0.220E-13
–	4	4.285	0.078	0.456	0.049	4.045E-13	0.115E-13
–	5	4.154	0.096	0.371	0.056	2.194E-13	0.075E-13
–	6	4.038	0.118	0.411	0.071	1.268E-13	0.055E-13
–	7	4.093	0.121	0.443	0.071	7.628E-14	0.330E-14
–	8	4.118	0.211	0.355	0.093	3.329E-14	0.219E-14
–	9	4.143	0.363	–	–	1.443E-14	0.138E-14
–	10	3.326	0.576	–	–	7.179E-15	1.351E-15
AWM7	1	2.780	0.056	1.440	0.094	3.722E-12	0.169E-12
–	2	3.351	0.046	1.120	0.070	2.023E-12	0.072E-12
–	3	3.526	0.040	0.798	0.032	1.451E-12	0.027E-12
–	4	3.616	0.040	0.647	0.027	9.924E-13	0.175E-13
–	5	3.728	0.041	0.623	0.028	7.379E-13	0.134E-13
–	6	3.609	0.044	0.538	0.027	5.481E-13	0.102E-13
–	7	3.631	0.039	0.476	0.021	4.421E-13	0.068E-13
–	8	3.547	0.049	0.391	0.024	2.772E-13	0.050E-13
–	9	3.528	0.057	0.434	0.027	1.639E-13	0.034E-13
–	10	3.391	0.079	0.334	0.044	1.108E-13	0.041E-13
Coma	1	9.933	1.389	0.490	0.154	1.500E-12	0.091E-12
–	2	8.079	0.528	–	–	1.326E-12	0.071E-12
–	3	8.396	0.222	0.275	0.056	1.400E-12	0.029E-12
–	4	8.395	0.184	0.257	0.044	1.310E-12	0.022E-12
–	5	8.156	0.168	0.251	0.038	1.165E-12	0.018E-12
–	6	8.324	0.166	0.233	0.039	1.032E-12	0.016E-12
–	7	8.231	0.121	0.297	0.028	9.749E-13	0.111E-13
–	8	8.339	0.132	0.270	0.032	6.986E-13	0.088E-13
–	9	8.140	0.132	0.333	0.033	4.489E-13	0.065E-13
–	10	8.320	0.222	0.278	0.063	3.279E-13	0.078E-13
E1455+2232	1	4.409	0.095	0.503	0.040	4.869E-12	0.098E-12
–	2	5.247	0.244	0.401	0.117	5.104E-13	0.297E-13
–	3	4.954	0.263	0.509	0.125	9.724E-14	0.664E-14
–	4	5.165	0.796	–	–	1.468E-14	0.168E-14
–	5	5.408	0.772	–	–	1.197E-14	0.129E-14
–	6	6.167	2.284	–	–	5.321E-15	0.939E-15
–	7	4.679	3.423	–	–	1.590E-15	0.604E-15
EXO0422	1	2.429	0.027	0.705	0.033	6.726E-12	0.144E-12
–	2	2.938	0.045	0.557	0.037	2.158E-12	0.060E-12
–	3	2.953	0.039	0.389	0.025	8.194E-13	0.192E-13
–	4	3.047	0.055	0.310	0.032	3.005E-13	0.094E-13
–	5	3.140	0.072	0.342	0.044	1.531E-13	0.062E-13
–	6	2.825	0.097	0.402	0.055	8.436E-14	0.457E-14
–	7	2.564	0.078	0.290	0.044	5.283E-14	0.295E-14
–	8	2.296	0.134	0.367	0.075	2.223E-14	0.225E-14
–	9	2.366	0.189	0.244	0.074	1.221E-14	0.152E-14
–	10	3.089	0.434	–	–	1.069E-14	0.135E-14

Table 5. continued.

Cluster	Annulus	T (keV)	σ_T (keV)	A	σ_A	F (0.3–10.0 keV) erg cm^{-2} s^{-1} arcmin^{-2}	σ_F (0.3–10.0 keV) erg cm^{-2} s^{-1} arcmin^{-2}
Hydra	1	3.251	0.040	0.620	0.035	1.179E-11	0.017E-11
–	2	3.653	0.064	0.468	0.037	3.962E-12	0.081E-12
–	3	3.503	0.057	0.426	0.030	1.247E-12	0.027E-12
–	4	3.810	0.070	0.293	0.034	5.933E-13	0.143E-13
–	5	3.943	0.088	0.346	0.046	2.957E-13	0.091E-13
–	6	3.970	0.127	0.340	0.070	1.451E-13	0.066E-13
–	7	4.170	0.142	0.322	0.071	7.686E-14	0.355E-14
–	8	6.665	0.484	–	–	4.059E-14	0.214E-14
Klemola 44	1	3.141	0.067	0.687	0.063	3.555E-12	0.125E-12
–	2	3.238	0.047	0.628	0.040	2.171E-12	0.055E-12
–	3	3.240	0.033	0.490	0.024	1.225E-12	0.022E-12
–	4	3.241	0.039	0.457	0.027	5.435E-13	0.116E-13
–	5	3.060	0.045	0.417	0.028	3.156E-13	0.076E-13
–	6	3.082	0.056	0.451	0.036	1.857E-13	0.055E-13
–	7	3.002	0.055	0.393	0.030	1.301E-13	0.035E-13
–	8	2.610	0.062	0.251	0.031	6.013E-14	0.224E-14
–	9	2.402	0.086	0.215	0.031	3.037E-14	0.150E-14
–	10	2.093	0.128	0.140	0.044	1.693E-14	0.166E-14
M87	1	1.517	0.006	0.379	0.007	2.240E-11	0.015E-11
–	2	1.650	0.004	0.879	0.015	7.215E-12	0.080E-12
–	3	1.802	0.006	0.772	0.010	3.905E-12	0.033E-12
–	4	2.033	0.006	0.635	0.009	2.494E-12	0.020E-12
–	5	2.065	0.007	0.556	0.008	1.756E-12	0.015E-12
–	6	2.231	0.011	0.538	0.009	1.242E-12	0.011E-12
–	7	2.347	0.009	0.465	0.007	1.060E-12	0.008E-12
–	8	2.470	0.011	0.406	0.008	6.960E-13	0.058E-13
–	9	2.526	0.013	0.362	0.008	4.294E-13	0.039E-13
–	10	2.604	0.021	0.362	0.014	3.265E-13	0.050E-13
MKW 3S	1	3.043	0.044	0.910	0.048	4.954E-12	0.120E-12
–	2	3.397	0.043	0.656	0.040	2.432E-12	0.057E-12
–	3	3.619	0.047	0.443	0.026	1.032E-12	0.019E-12
–	4	3.812	0.060	0.312	0.030	4.453E-13	0.095E-13
–	5	3.549	0.076	0.287	0.036	2.038E-13	0.056E-13
–	6	3.530	0.099	0.401	0.052	1.131E-13	0.042E-13
–	7	3.473	0.101	0.327	0.046	6.595E-14	0.239E-14
–	8	3.625	0.157	0.482	0.070	3.148E-14	0.168E-14
–	9	3.955	0.225	–	–	1.610E-14	0.105E-14
–	10	4.597	0.866	–	–	8.398E-15	1.077E-15
MKW 4	1	1.573	0.023	1.651	0.184	2.340E-12	0.302E-12
–	2	2.096	0.056	1.521	0.235	5.578E-13	0.820E-13
–	3	2.008	0.052	0.643	0.076	2.307E-13	0.192E-13
–	4	2.001	0.064	0.506	0.074	1.056E-13	0.096E-13
–	5	1.944	0.067	0.483	0.070	7.648E-14	0.703E-14
–	6	1.984	0.078	0.412	0.070	5.420E-14	0.525E-14
–	7	1.741	0.078	0.419	0.056	3.543E-14	0.327E-14
–	8	1.679	0.053	0.278	0.052	1.979E-14	0.219E-14
–	9	1.523	0.079	0.235	0.052	1.160E-14	0.177E-14
–	10	1.244	0.078	0.259	0.103	5.885E-15	2.469E-15
Perseus	1	4.043	0.014	0.477	0.008	5.565E-11	0.149E-11
–	2	3.292	0.007	0.681	0.007	3.332E-11	0.008E-11
–	3	3.686	0.006	0.676	0.005	1.964E-11	0.003E-11
–	4	4.276	0.007	0.610	0.005	9.889E-12	0.020E-12
–	5	5.215	0.014	0.508	0.006	5.551E-12	0.014E-12
–	6	5.766	0.023	0.482	0.008	3.584E-12	0.011E-12
–	7	6.071	0.022	0.456	0.007	2.514E-12	0.008E-12
–	8	6.484	0.028	0.416	0.009	1.631E-12	0.006E-12
–	9	6.741	0.029	0.424	0.010	1.030E-12	0.004E-12
–	10	7.258	0.072	0.405	0.018	7.729E-13	0.056E-13
Perseus a[10]	1	3.973	0.021	0.560	0.014	4.996E-11	0.022E-11
–	2	3.195	0.099	0.689	0.009	3.128E-11	0.011E-11
–	3	3.598	0.088	0.675	0.006	1.912E-11	0.004E-11
–	4	4.199	0.011	0.584	0.007	9.600E-12	0.027E-12

Table 5. continued.

Cluster	Annulus	T (keV)	σ_T (keV)	A	σ_A	F (0.3–10.0 keV) erg cm^{-2} s^{-1} arcmin^{-2}	σ_F (0.3–10.0 keV) erg cm^{-2} s^{-1} arcmin^{-2}
–	5	5.044	0.019	0.506	0.009	5.425E-12	0.020E-12
–	6	5.612	0.033	0.460	0.011	3.417E-12	0.015E-12
–	7	5.926	0.030	0.441	0.010	2.217E-12	0.009E-12
–	8	6.309	0.038	0.401	0.012	1.298E-12	0.007E-12
–	9	6.612	0.040	0.410	0.014	8.264E-13	0.050E-13
–	10	7.006	0.099	0.397	0.025	6.279E-13	0.065E-13
PKS 0745-19	1	4.875	0.080	0.538	0.033	2.748E-11	0.030E-11
–	2	7.354	0.226	0.413	0.044	7.893E-12	0.121E-12
–	3	7.733	0.210	0.332	0.039	2.275E-12	0.041E-12
–	4	8.278	0.326	0.362	0.065	6.574E-13	0.194E-13
–	5	9.087	0.659	0.463	0.111	2.923E-13	0.128E-13
–	6	8.200	0.616	0.524	0.101	1.514E-13	0.070E-13
–	7	8.579	0.687	–	–	7.834E-14	0.380E-14
–	8	8.506	1.375	–	–	2.868E-14	0.219E-14
–	9	6.472	1.167	–	–	1.626E-14	0.165E-14
–	10	4.732	1.481	–	–	1.090E-14	0.202E-14
RXCJ0605.8-3518	1	3.866	0.089	0.717	0.069	5.409E-12	0.171E-12
–	2	5.408	0.220	0.416	0.103	1.104E-12	0.054E-12
–	3	4.811	0.189	0.227	0.074	3.412E-13	0.153E-13
–	4	4.537	0.286	0.295	0.103	9.945E-14	0.645E-14
–	5	4.834	0.437	–	–	4.333E-14	0.313E-14
–	6	6.248	1.149	–	–	1.980E-14	0.180E-14
–	7	8.425	3.500	–	–	1.031E-14	0.132E-14
RXCJ2234.5-3744	1	11.165	1.896	0.323	0.102	2.133E-12	0.124E-12
–	2	11.087	1.011	–	–	1.577E-12	0.069E-12
–	3	9.664	0.415	0.290	0.055	6.989E-13	0.192E-13
–	4	8.816	0.651	–	–	2.285E-13	0.076E-13
–	5	5.890	0.477	0.198	0.094	7.595E-14	0.405E-14
–	6	4.478	0.584	–	–	2.822E-14	0.216E-14
–	7	3.566	0.594	–	–	1.229E-14	0.128E-14
–	8	2.412	1.099	–	–	2.150E-15	0.697E-15
RXJ0658-55	1	12.257	1.286	0.229	0.050	2.409E-12	0.109E-12
–	2	14.686	1.205	–	–	1.592E-12	0.064E-12
–	3	14.799	0.975	–	–	6.728E-13	0.276E-13
–	4	13.160	1.248	–	–	1.555E-13	0.082E-13
–	5	10.503	1.156	–	–	5.489E-14	0.314E-14
–	6	18.091	6.064	–	–	2.052E-14	0.243E-14
RXJ1347-1145	1	11.426	0.446	0.390	0.045	9.748E-12	0.123E-12
–	2	15.643	1.239	0.214	0.081	9.690E-13	0.329E-13
–	3	11.086	1.179	–	–	1.594E-13	0.072E-13
–	4	7.533	1.484	–	–	1.935E-14	0.180E-14
–	5	10.277	3.281	–	–	9.269E-15	1.140E-15
Sérsic 159-3	1	2.365	0.016	0.554	0.015	7.273E-12	0.074E-12
–	2	2.614	0.018	0.466	0.016	2.359E-12	0.033E-12
–	3	2.741	0.024	0.366	0.014	6.529E-13	0.092E-13
–	4	2.642	0.031	0.278	0.019	1.670E-13	0.037E-13
–	5	2.572	0.041	0.224	0.021	8.322E-14	0.222E-14
–	6	2.523	0.061	0.255	0.030	4.061E-14	0.153E-14
–	7	2.093	0.056	0.152	0.018	1.848E-14	0.076E-14
–	8	1.681	0.053	–	–	6.327E-15	0.443E-15
–	9	1.322	0.059	–	–	1.637E-15	0.291E-15
–	10	2.491	0.528	–	–	2.306E-15	0.436E-15
Sérsic 159-3 a[11]	1	2.374	0.026	0.554	0.024	7.165E-12	0.112E-12
–	2	2.600	0.030	0.486	0.027	2.424E-12	0.054E-12
–	3	2.744	0.039	0.351	0.022	6.678E-13	0.148E-13
–	4	2.606	0.051	0.246	0.030	1.739E-13	0.061E-13
–	5	2.620	0.065	0.278	0.039	8.679E-14	0.376E-14
–	6	2.424	0.094	0.155	0.024	4.177E-14	0.187E-14
–	7	2.276	0.121	–	–	1.952E-14	0.107E-14
–	8	1.898	0.136	–	–	7.853E-15	0.706E-15
–	9	1.519	0.140	–	–	2.530E-15	0.478E-15
–	10	1.287	0.085	–	–	2.632E-15	0.615E-15

Table 5. continued.

Cluster	Annulus	T (keV)	σ_T (keV)	A	σ_A	F (0.3–10.0 keV) erg cm^{-2} s^{-1} arcmin^{-2}	σ_F (0.3–10.0 keV) erg cm^{-2} s^{-1} arcmin^{-2}
Triangulum	1	10.192	1.381	0.554	0.588	3.323E-12	0.510E-12
–	2	11.615	1.334	0.344	0.172	3.126E-12	0.183E-12
–	3	9.432	0.388	0.330	0.066	2.436E-12	0.059E-12
–	4	9.337	0.388	0.308	0.065	1.538E-12	0.039E-12
–	5	9.405	0.410	0.272	0.067	1.053E-12	0.028E-12
–	6	9.528	0.450	0.222	0.074	7.344E-13	0.213E-13
–	7	8.379	0.252	0.331	0.043	5.297E-13	0.111E-13
–	8	9.156	0.495	–	–	2.796E-13	0.065E-13
–	9	8.701	0.633	–	–	1.385E-13	0.038E-13
–	10	13.256	2.205	–	–	9.028E-14	0.600E-14
ZW3146	1	5.289	0.068	0.517	0.028	7.745E-12	0.083E-12
—	2	8.106	0.259	0.255	0.054	1.116E-12	0.027E-12
–	3	7.668	0.312	0.221	0.053	1.985E-13	0.056E-13
–	4	7.542	0.746	–	–	3.378E-14	0.162E-14
–	5	10.906	2.961	–	–	1.589E-14	0.140E-14
–	6	6.385	1.955	–	–	4.422E-15	0.642E-15

[8] Dashes in the abundance column signifies that the abundance for the given annulus has been linked to the abundance above.
[9] Second observation.
[10] Second observation, under the name Abell 426 in the archive.
[11] Second observation, under the name AS 1101 in the archive.